2015

Biomechanics of aligned cell sheets for arterial tissue engineering

https://hdl.handle.net/2144/16092

Boston University

BOSTON UNIVERSITY

COLLEGE OF ENGINEERING

Dissertation

BIOMECHANICS OF ALIGNED CELL SHEETS FOR ARTERIAL TISSUE ENGINEERING

by

DANIEL EDWIN BACKMAN

B.S., Tufts University, 2005

Submitted in partial fulfillment of the
requirements for the degree of
Doctor of Philosophy
2015

Approved by

First Reader Joyce Wong

Joyce Y. Wong, Ph.D.
Professor of Biomedical Engineering

Second Reader

Michael L. Smith, Ph.D.
Associate Professor of Biomedical Engineering

Third Reader

Jerome Mertz, Ph.D.
Professor of Biomedical Engineering

Fourth Reader Béla Suki

Bela Suki, Ph.D.
Professor of Biomedical Engineering

Fifth Reader

Matthew Layne, Ph.D.
Assistant Professor of Biochemistry

Dedication

I dedicate my dissertation to all the people who have supported me throughout my time at BU and throughout my life. First, I would like to thank my wife, Jenny, who has supported me throughout of my dissertation with unwavering encouragement, helpful scientific discussions, and patience. I would also like to thank her for finally learning to not ask when I'm going to be done with my PhD! I would also like to thank my parents for their support and guidance throughout my life. Also, I would like to thank them for encouraging me to pursue my PhD.

I would also like to thank Tuan Pham and Shamit Shrivastava for their friendship throughout my time at BU. I'd like to thank them for being there when experiments failed and their continued encouragement. And thanks for all the coffee breaks where we talked about research, life, and everything in between.

Acknowledgments

I would first like to thank my advisor Professor Joyce Wong for all her guidance and support throughout my dissertation. I would also like to thank all of the Wong lab members for all their technical support. I would also like to thank the undergraduate students whom have helped me during my thesis, Bauer LeSavage, Shivem Shah, William Wang and Kevin Shen. Additionally, I would like to thank my committee members Professor Michael Smith, Professor Bela Suki, Professor Matt Layne and Professor Jerome Mertz for their helpful guidance.

I would also like to thank the Quantitative Biology and Physiology Training grant for providing me with funding at BU. I would like to thank Professor Katya Ravid and the Cardiovascular Biology Training grant for broadening my understanding of cardiovascular biology as well as funding me during graduate school.

BIOMECHANICS OF ALIGNED CELL SHEETS FOR ARTERIAL TISSUE ENGINEERING

DANIEL EDWIN BACKMAN

Boston University College of Engineering, 2015

Major Professors: Joyce Y. Wong, Ph.D., Professor of Biomedical Engineering

ABSTRACT

Cardiovascular disease remains the leading cause of death in the United States and oftentimes damaged or occluded arteries need to be replaced. Current surgical materials are unsuitable for small diameter, high pressure vessels such as the carotid and coronary artery because they cannot match the mechanical properties of native tissue. Compliance mismatch between the two materials leads to complications such as anastomotic intimal hyperplasia, thrombosis, and aneurysm. Therefore there is significant clinical need for a tissue engineered arterial graft suitable for small diameter, high pressure vessels.

An artery is composed of three layers, but the middle layer, the tunica media, is responsible for bearing normal physiological loads. The medial layer features alternating layers of smooth muscle cells and extracellular matrix where each layer has smooth muscle cells and collagen aligned helically along the length of the artery. This structural feature coupled with the composition of the extracellular matrix cause arterial tissue to have a non-linear mechanical response. A tissue engineered vascular graft that recapitulates the native arterial structure may overcome the limitations of current tissue engineered strategies.

We hypothesize that a tissue engineered arterial graft can be built by stacking aligned, single layer cell sheets to better mimic native mechanical properties. Cell sheets are confluent layer of cells and extracellular matrix. In the first aim of this work we developed an inexpensive, novel force sensor design capable of measuring small forces (< 1 mN) that we incorporated into a custom-built uniaxial tensile tester. For the second aim we developed a technique for culturing single layer, aligned, bovine vascular smooth cell sheets. We accomplished this by developing a technique for grafting N-isopropylacrylamide, a thermo-responsive polymer, onto the surface of flat and micropatterned poly-dimethylsiloxane (PDMS) substrates. These substrates allow cell sheets to be cultured and then be detached by decreasing the temperature. In the third aim we experimentally characterized the mechanical and structural properties of aligned vascular smooth muscle cell sheets to show that cell orientation can be controlled by the micropattern and that cellular alignment leads mechanical anisotropy. We also successfully modeled the cell sheet mechanical behavior using existing phenomenological models. The results from this work suggest that aligned cell sheets are capable of recapturing the non-linear stress-strain response of native arterial tissue, making them suitable for arterial tissue engineering. The results from this work provide an experimental and computational foundation for future efforts towards building a multi-layered cell sheet based arterial tissue.

Table of Contents

List of Tables

List of Figures

List of Abbreviations

AFM	Atomic Force Microscopy
APTES	(3-aminopropyltriethoxysilane)
COTS	Commercial off-the-shelf
DAQ	Data acquisition
EMI	Electromagnetic interference
FFT	Fast Fourier Transform
FT-IR	Fourier Transformed Infrared Spectroscopy
NIPAAm	N-isopropylacrylamide
p-p	Peak-to-peak
PDMS	(poly) dimethylsiloxane
PK	Piola-Kirchoff
pNIPAAm	Polymerized NIPAAm
RMS	Root Mean Squared
SIP	Systems in a package

Chapter 1: Specific Aims and Introduction

Specific Aims 1: Develop a uniaxial tensile tester and force sensor capable of measuring the mechanics of cell sheet based tissues.

Measuring forces in cell sheets requires precise measurement of small forces (<10 mN), a range lower than the capabilities of most commercial force sensors. Furthermore, these sensors are expensive, fragile, and limited to a single force range. For this aim, we developed a cantilevered beam force sensor design that combines a Hall-Effect sensor with a pair of magnets to measure tip deflection. The sensor design is accurate, inexpensive, easy to manufacture, and customizable for multiple force ranges. For this aim, we built and characterized four force sensors built for different force ranges and the most sensitive force sensor can measure forces in the 0–5 mN range with approximately 2.5 μN resolution.

Specific Aim 2: To develop a thermo-responsive substrate system for the culture of vascular smooth muscle cell sheets for arterial tissue engineering.

In this aim, we developed a method for the long-term culture of aligned, contractile, vascular smooth muscle cell sheets on thermo-responsive PDMS substrates and then demonstrated that these cell sheets are both mechanically and structurally anisotropic. Building upon previous work in our lab, we used benzophenone to initiate the free radical polymerization of N-isopropylacrylamide (NIPAAm) onto the surface of PDMS substrates. We then were able to correlate cell attachment with NIPAAm surface density measurements. To allow the long-term culture of contractile, vascular smooth muscle cell sheets on these substrates, we coated the substrate surface with 3-aminopropyltriethoxysilane to improve cell attachment and sheet formation. Using this substrate platform, we were able to grow non-patterned cell sheet and patterned cell sheets that are structurally anisotropic.

Specific Aim 3: To characterize the mechanical and structural properties of vascular smooth muscle cell sheets and model their mechanical behavior.

This third aim builds upon the work of the first two aims to understand the mechanical properties of single layer cell sheets. We showed that cells grown on flat and patterned substrates do not alter the amount of extracellular matrix secretion by the smooth muscle cells, but does cause cellular alignment and collagen alignment in the cell sheets. We then characterized the mechanics of the aligned cell sheets to show that cell sheets are significantly stiffer (800%) in the alignment direction, but fail at lower engineering strains (80%) in the alignment direction compared to the transverse direction. Using a generalized version of a phenomenological model developed by Lanir, we then modeled the stress-strain behavior of the cell sheet-based tissues to better extract the incremental tensile modulus.

Clinical Significance

Cardiovascular disease, in particular atherosclerosis, remains one of the leading causes of mortality in the western world[1]. Atherosclerosis is a disease characterized by accumulation of lipids and fibrous elements on walls of larger arteries and it is estimated to be the cause of 50% of the deaths in the Western world[2,3]. Eventually, accumulation of lipids and fibrous material will form atherosclerotic plaques that occlude the vessel wall and impair blood flow through the vessel[3]. Atherosclerotic plaques can also rupture, leading to thrombus formation and subsequent myocardial infarction[3].

Surgery, such as a bypass operation or balloon angioplasty, is often required to restore normal flow to occluded blood vessels [4,5]. In the United States, coronary and peripheral vascular bypass procedures are performed in approximately 600,000 patients a year using autologous venous sources such as the saphenous vein or the internal mammary artery[6,7]. While autologous replacement has had success in part because it avoids the immune response from allogenic or xenogenic sources, harvesting autologous tissues is expensive, time consuming and leads to an increased incidence of surgical complications[8]. Moreover, approximately one-third of patients do not have usable veins for by-pass grafting because of pre-existing vascular disease[8]. As a result of these limitations, there is a significant clinical need for a tissue engineered vascular graft that can be constructed from autologous sources [4,9,10].

Arterial Wall Structure & Mechanics

Arteries are particularly amenable to tissue engineering because they are essentially composed of concentric rings of circularized cell sheets. The arterial wall has three distinct layers: the tunica intima, the tunica media and tunica adventitia (Figure 1). The innermost layer, the tunica intima, is composed of a single layer of endothelial cells that contacts the blood and is supported by a proximal subendothelial layer composed of collagen and other matrix proteins, and beyond that an inner elastic lamina composed of elastin, collagen, and proteoglycans[11,12]. The endothelial cells in the tunica intima actively protect against thrombus formation[13], and are responsible for signal transduction to vascular smooth muscle cells in the tunica media immediately adjacent to the opposite side of the inner elastic lamina.

The tunica media is composed of alternating layers of vascular smooth muscle cells and extracellular matrix composed of collagen, elastin, and proteoglycans. Many studies of the anatomy of the artery have shown that the medial layer of the artery has a complex, but well-defined hierarchical structure[11,14]. Vascular smooth muscle cells are aligned within individual layers, and have a contractile, non-proliferative contractile phenotype with an elongated morphology[15,16]. Wavy collagen fiber bundles are aligned helically along the length of the artery with successive layers aligned in different directions[11,17]. The individual layers of vascular smooth muscle cells, collagen and elastin form individual lamellae that are approximately 10 μm thick[11].

The tunica adventitia is the outermost layer of the artery and is composed of extracellular matrix, vascular smooth muscle cells, fibroblasts and densely woven collagen. The structure is not nearly as well-defined as the media and provides mechanical support when loaded with super-physiological loads[11]. The tunica adventitia also hosts the vaso vasorum, which is composed of arterioles, venules and capillaries required for proving nutrients for smooth muscle cells within tunica media[11].

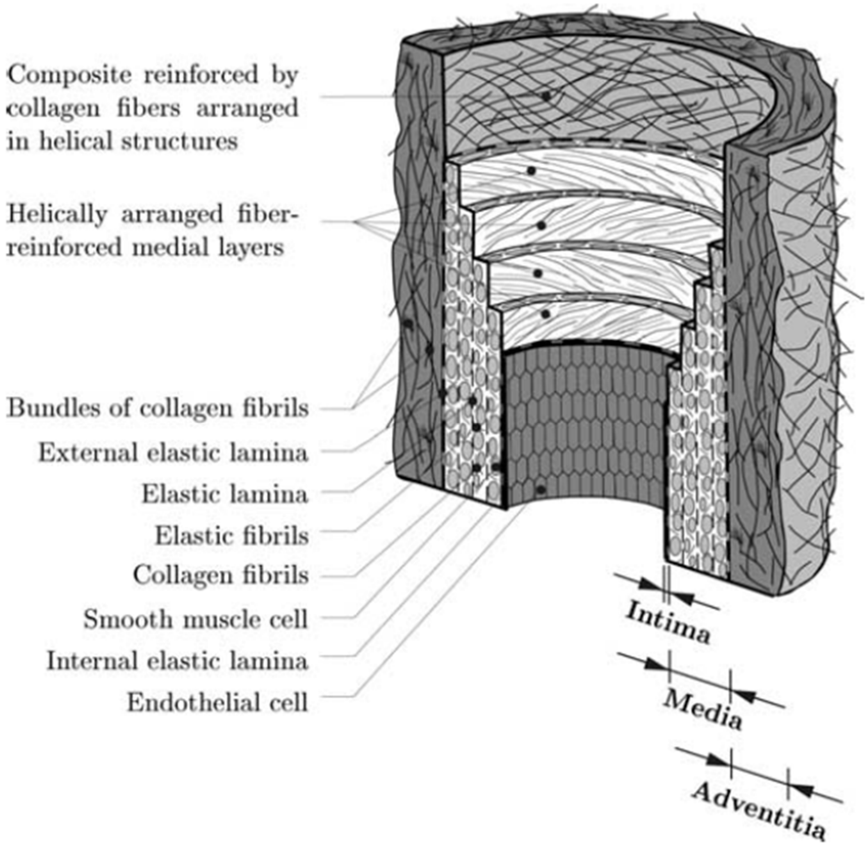

Figure 1: The artery wall has a well-defined structure with three layers: intima, media and adventitia. This figure was originally published in Holzapfel, 2000.[18]

Elastin is the most common extracellular matrix protein in the arterial wall, comprising nearly 50% of the dry weight[19]. Elastin is an amorphous protein and forms an elastic fiber during development when tropoelastin, an elastin precursor, is deposited onto fibrillin-rich microfibrils[20,21]. This results in a composite material featuring an elastin core, cross-linked by lysyl oxidase, and micro-fibrils surrounding the elastin core[20]. These elastic fibers are arranged in fenestrated, concentric rings within the media of elastic arteries such as the aorta and common carotid artery (CCA)[22]. As pressure builds in the artery, the waviness (or fenestration) of the elastin is lost and the artery begins to bear load[14]. Beyond a structural role, elastin is also a potent regulator of vascular smooth muscle cells[22]. For example, elastin knockout mice develop obstructive arterial disease caused by wall thickening due to vascular smooth muscle cell proliferation, suggesting that elastin fibers help keep vascular smooth muscle cells in a quiescent contractile phenotype[23].

Collagen is another important extracellular matrix protein found within the tunica media and tunica adventitia. Collagen is synthesized first as soluble procollagen, which is then converted into collagen by enzymatic cleavage of the terminal pro-peptides by metalloproteinases[24]. The collagen then self-assembles into fibrils composed of three polypeptide chains in a triple alpha helix conformation, which are subsequently stabilized by lysl oxidase (LOX)-dependent cross-linking of exposed lysine residues[24]. Collagen is extremely stiff with measurements on single collagen fibers ranging from 5–11.5 GPa[24,25].

The geometry of major arteries varies spatially along the length of the artery, and there are significant anatomical differences between individuals. For example, a recent study of 11 human carotid arteries showed that the wall thicknesses of the common carotid artery (CCA) and internal carotid artery (ICA) were 1.17 ± 0.16 (SD) mm and 0.86 ± 0.06 (SD) mm, respectively[26]. The average media thickness of the ICA and the CCA was measured to be 0.7 ± 0.13 (SD) mm and 0.53 mm ± 0.10 (SD), respectively[26]. Another study measured the geometry of 15 human left anterior descending (LAD) artery walls[27]. The wall thickness measured to be 0.87 ± 0.23 (SD) mm and the medial layer thickness was measured to be 0.32 ± 0.11 (SD) mm[27]. It is important to note that these arterial wall thickness measurements were made in the unloaded configuration because it has been shown that the arterial wall thickness decreases with increased applied load[28].

The arterial wall structure governs its mechanical properties – specifically a non-linear stress-strain response. The matrix components, primarily collagen and elastin, have been shown to dominate the passive mechanical response[29]. Due to its high extensibility, elastin, bears the hemodynamic loads at low strains[30,31]. At low strains, collagen fibers are crimped and cannot bear load because the collagen fibers only support load in tension (and not in compression)[15]. As the strain increases, the collagen fibers are gradually recruited, leading to a significant stiffening of the arterial tissue. It is thought that this gradual recruitment of stiff collagen fibers gives the arterial tissue its non-linear stress-strain response[32]. Collagen is also essential for maintaining arterial stability and preventing rupture of the arterial wall under high pressures[33]. While the mechanical properties of the artery are dominated by elastin and collagen, vascular smooth muscle cells contribute to the active mechanical response by contracting the vessel wall in response to vasoactive agonists[16].

It is vitally important that the mechanical properties of arteries be considered in order to maintain patency of a tissue engineered arterial patch. As blood pulses through an artery, it exerts a cyclic load on the arterial wall that the tissue engineered artery or patch must also be able to withstand because failure of a graft could lead to arterial dissection, aneurysm, and potentially death[4,9,32]. The tissue engineered artery must also have a compliance that is similar to native tissue at sites of anastamoses, because compliance mismatch between graft and host will lead to intimal hyperplasia[34–36]. In practical terms, these requirements dictate that the tissue engineered artery be designed to have a stiffness and stress-strain response similar native tissue, and a high enough failure stress to avoid rupture.

In order to meet these requirements, it is first necessary to obtain precise knowledge of the mechanical properties of human arterial tissue[37]. However, the difficulty in obtaining human cadaver tissue has made data derived from experimental determination of the actual stress-strain behavior of human arterial tissue sparse. In one study, arterial tissue taken from 205 patients ranging in age from 1 day old to 80 years old had stiffnesses ranging from 0.9–4.2 MPa when subject to inflation and axial loading as shown in Figure 2, with significant variability between the mechanical properties and tissue stiffness with age.

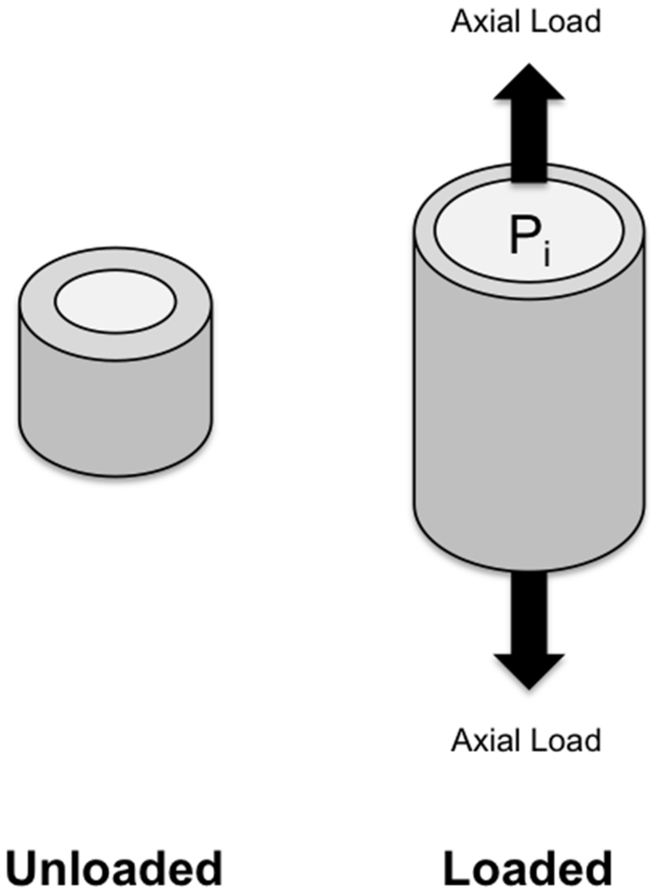

Figure 2: Arteries are loaded in two dimensions. Pressure within the artery (Pi) cause the diameter of the artery to increase and increase in circumferential stresses. Along the axis of symmetry, the artery is subject to a load, creating an axial stress and lengthening the artery.

Recent work by Holzapfel measured failure mechanics properties of individual layers (intima, media, adventitia) of coronary tissue for 15 human subjects [27]. The medial layer of arterial tissue typically failed at 0.49 ± 0.19 MPa. Interestingly, the report does not give a tangent modulus of the tissue but rather the data was analyzed by fitting it to a constitutive model for non-linear mechanical behavior. Individual samples were compared via the fitting parameters[27]. Another recent study measured the mechanics of coronary artery tissue using uniaxial tensile tests to measure failure properties of native tissue. In this study of 5 coronary arteries, the tissue failed at approximately 0.39 ± 0.09 MPa, which is similar to the result reported by Holzapfel. While these studies have begun to describe the mechanics of arterial tissue, failure mechanics alone do not fully capture the stress-strain response of the arterial tissue. As described above, arteries have a non-linear stress strain curve, and it is possible that other tissues could have significantly different material response curves, but fail at the same stress.

The determination of the stress levels in arterial tissue is complex for several reasons. First, the *in vivo* loading environment of arterial tissue is 2-dimensional as highlighted in Figure 2, being subject to both axial load as well as circumferential load caused by internal pressure.[38] Thus, uniaxial tensile tests are unable to completely recapture physiological loading environments of native tissue. However, biaxial tensile tests measure the stress-strain response of tissue by stretching the tissue in 2 directions simultaneously, providing a more physiologically relevant loading environment[39–41].

While still providing some insight into the mechanics of arterial tissue, clinical studies in living patients typically report the compliance of arterial tissue, which refers to the change in vessel area (or diameter) with respect to pressure in the artery. Recent efforts have been devoted towards bridging the gap between the stress-state of the arterial tissue and clinical data by the use of computational modeling frameworks[42]. To accomplish this, assumptions had to be made about the axial stretch of the artery as well as that the axial force remains constant, thus the computational frameworks remain imperfect[42].

Arterial Tissue Engineering

Due to the frequent absence of usable autologous blood vessels in patients with vascular disease, significant effort has been devoted to developing a tissue engineered vascular graft. Early efforts towards developing a replacement blood vessel involved using PTFE and Dacron, but the resulting compliance mismatch caused anastomotic hyperplasia and an increased incidence of thrombus formation[43]. Thus, although these artificial grafts are still widely used, they provide a less than ideal solution. The idea for a blood vessel made of biological material and grown *in vitro* was first proposed by Weinberg and Bell in 1986 where they used collagen gels as the basis for a vascular graft[44]. While there a myriad of techniques for building a tissue engineered vascular graft, they can be divided into two basic categories: top-down and bottom-up approaches. Top-down approaches involve seeding cells onto degradable scaffolds or decellularized extracellular matrix to give the artery its structural and mechanical properties. On the other hand, bottom up approaches rely on the self-assembly and directed-assembly of nanoscale and microscale structures to recapture macroscopic structure and properties of native tissues[45,46].

Over the past several decades, top-down tissue engineering approaches have been the more common strategy for building a tissue engineered vascular graft. Most of the early studies involved seeding cells onto a synthetic, polymeric scaffold. In 1998, Shinoka *et al*. developed a pulmonary graft by seeding autologous cells onto a biodegradable (polyglactin/polyglycolic) acid scaffold[47]. This was the first reported use of an autologous cell source combined with a polymeric scaffold. Niklason *et al.,* developed a tissue engineered blood vessel using cells seeded onto poly-glycolic acid (PGA) tubular scaffolds and exposing the blood vessels to 1–2% cyclic mechanical strain for 7–8 weeks using a bioreactor and then adding an endothelial lining to prevent thrombosis formation[48]. Progress has been made towards developing "readily available" tissue engineered vascular grafts that show no thrombus formation and minimal calicification[49] For example, in one study tubular degradable poly-glycolic acid (PGA) scaffolds were seeded with SMCS, cultured in a bioreactor and then decellularized leaving cell-derived matrix[49]. The tubular ECM constructs were seeded with smooth muscle cells and endothelial cells, implanted, and functioned for 1 month post-implantation[49]. Scaffold based tissue engineering technologies have typically been limited by their inability to grow and remodel after implantation. However, recent advances have shown degradable scaffolds some potential to grow and remodel[50–52]. Still, scaffold based tissue engineering techniques continue to advance, but still provide minimal control of the microscale tissue structure[4,46].

Decellularized extracellular matrix scaffolds remain another popular method for growing vascular tissue. Tissue decellularization can be accomplished by using harsh chemical treatments (acid/base, detergents), mechanical agitation (freezing, pressure) and enzymatic digestion, detailed in a review by Gilbert *et al.*[53]. In a pioneering study, researchers decellularized human saphenous veins and tested their mechanical properties *in vitro,* demonstrating suitable burst and suture holding strength[54]. In the same study, canine jugular veins that had been decellularized and implanted as carotid interposition grafts showed *in vivo* patency for 2 weeks without rupture[54]. Another early study used decellularized arteries as the basis of a vascular graft and seeded the decellularized artery with marrow-derived cells and then implanted the construct[55]. This study showed bone marrow-derived cells (BMCs) differentiated using the canine interposition graft model resulted in regeneration of the artery as well as improved patency in decellularized arteries seeded with BMCs compared with acellular controls over 8 weeks[55]. In another report, human umbilical arteries were decellularized and then implanted, but developed thrombosis before developing an intact endothelium[56]. This study highlighted how important the endothelial layer is in creating a functional arterial replacement. These studies highlight some of the advances and difficulties of using decellularized extracellular matrix as a tissue engineered vascular graft. Since these initial studies, the field has grown rapidly. Reviews by Badylak, Crapo, and Fu are referenced for more detailed exposition into the state of the art[57–60]. Taken together, these studies demonstrate that decellularized arterial tissue retains some of the structural features of native arteries, but still does not match their mechanical properties. These differences include a decrease in residual stresses, increased stiffness, and decreased extensibility[61], and may be related to the inability of decellularized vessels to recapture the native microstructural organization upon recellularization[46]. Thus, the top-down approaches (scaffold & decellularization methods) for tissue engineering still have yet to succeed because loss of microstructural organization changes the mechanical properties of an artery in potentially significant ways. Clearly a better approach would be to use tissue engineering strategies that enable the control of tissue microstructure, which can better recapture the functional properties of native tissue.

Bottom-up approaches have become increasingly popular for growing tissue engineered vascular grafts because they promise such microstructural control. Bottom-up approaches use self-assembly (cell sheets) or directed assembly (bioprinting) of microscale features to engineering a tissue with controlled structural features[45]. Cell sheets, self-assembly methods, and most recently tissue bioprinting are all examples of bottom-up strategies for tissue engineering.

Bioprinting has become an attractive strategy because one can precisely print cells embedded in gels, carbohydrate glass[62], and into 3-dimensional geometrical patterns. While still a burgeoning technology that is rapidly advancing, bioprinting has yet to be widely adopted due to high cost, complexity and limited availability of commercial bioprinters[63]. Bioprinters have limited resolution (> 5 μm) and have slow print speed with the printer head capable of traveling from 10 μm/s to 1,600 mm/s[63]. Furthermore, bioprinters have limited compatibility with physiologically relevant materials and cells. Bioprinter materials have limited mechanical integrity, making them unsuitable for applications where mechanical strength and integrity is important, such as arterial tissue engineering.

Self-assembly is the oldest of these bottom-up strategies. A completely biologically derived tissue engineered vascular graft based upon self-assembly was first demonstrated in 1998 by L'Heureux *et al.*[64]. By culturing fibroblasts and smooth muscle cells for 3–4 weeks, ECM-rich sheets were formed and then wrapped around a mandrel to form a tubular structure[64]. However, despite producing thick tissues, this method still did not capture the native tissue structure. The premise underlying the work in this thesis is that cell sheets can be used in a similar manner to create tubular structures, but in a way that leads to better microstructural control.

Thermo-responsive Substrate Strategies for Cell Sheet Engineering

Cell sheet engineering strategies can be used to build tissue engineered vascular grafts without polymeric scaffolding. Cell sheets are confluent layers of cells and extracellular matrix and can be harvested using thermo-responsive substrates, hydrogels or enzymatically degradable substrates[65–67]. Okano *et al.* pioneered the idea of using a thermo-responsive substrates for non-enzymatic harvest of cells by grafting N-isopropylacrylamide onto polystyrene dish surfaces[68]. The thermo-responsive substrate platform is driven by the thermodynamic properties because N-isopropylacrylamide polymer undergoes a lower critical solution phase transition at 32˚C [69]. In water, NIPAAm polymer aggregates and form hydrophobic globular domains at temperatures above 32 °C, while below that temperature it transitions into a hydrophilic coil formation[70]. When grafted onto a substrate, this thermodynamically driven process leads to substrates being hydrophobic at 37 °C and more hydrophilic below 32˚C[68]. Okano *et al.*, further demonstrated that cell sheets (i.e. confluent layers of cells) could also be grown on these thermo-responsive NIPAAm-based substrates[71]. Since this work, many different labs have developed different methods to produce cell sheets on NIPAAm substrates; a detailed summary of the different techniques can be found in several reviews[72–74].

Thermo-responsive, poly(dimethysiloxane) (PDMS) substrates are advantageous for growing cell sheets for several reasons. PDMS is an inexpensive, non-cytotoxic, optically clear, silicone elastomer commonly used in biomedical application. PDMS can be cast easily onto micro-textured silicon wafers using soft lithography techniques. By changing the ratio of base and curing agent, the Young's modulus of the PDMS can be controlled[75]. As it is a soft material with a modulus in the range of 100 kPa to 1.6 MPa, it can be dynamically stretched[76]. Several different methods have been proposed and developed to graft NIPAAm onto the surface of PDMS. For example, Ebara *et al.* developed a method using the UV initiator benzophenone to graft NIPAAm onto the PDMS surface[77]. Their data demonstrates that grafting NIPAAm onto PDMS makes the surface more hydrophilic and that the water contact angle is less than 40 degrees at 20°C and greater than 80 degrees at 40°C. Thus, their results clearly demonstrate that a NIPAAm-PDMS system can produce similar thermo-responsive properties to other NIPAAm grafted surfaces[77]. Ma *et al.* subsequently extended this method to show that NIPAAm surfaces can be used both for growing osteoblast-based cell sheets and for controlled drug delivery[78]. Similarly, our laboratory also extended this method to grow aligned smooth muscle cell sheets on micro-textured PDMS substrates. In another recently developed method, NIPAAm was grafted onto the surface of PDMS by using argon plasma to creating reactive peroxide sites on the PDMS, and then baking the peroxidated PDMS with NIPAAm monomer[79]. This group was able use this substrate to grow aligned smooth muscle cell sheets. In yet another study, Akiyama *et al*. developed a method to graft NIPAAm by modifying the PDMS surface with various silanes and then irradiating the substrates with an electron beam[80]. However, although aortic endothelial cells would attach to this substrate, they would not grow into not cell sheets[80].

The variability in the success of the foregoing studies is likely due to the fact that structure and conformation of NIPAAm-coated surfaces impacts the thermo-physical properties of the surface, which in turn impacts the ease with which cells may become attached to it. This is clearly demonstrated in an early study by Okano *et al*., who showed that the surface graft density of NIPAAm correlated to cell attachment[71]. Surfaces with graft densities of 1.4 □g/mL showed acceptable cell attachment, while surfaces with a NIPAAm graft density of 2.9 □g/mL showed cells unable to attach and spread[71]. This study then determined that cell attachment correlated with fibronectin adsorption onto the surface, highlighting the fact that NIPAAm-coated surface are *incapable* of supporting cell attachment without adsorbed proteins[71]. The results of this paper thus highlight some of the fundamental properties of NIPAAm surfaces. First, surface density of NIPAAm has a significant impact on cell attachment. Second, protein adsorption is essential for cell attachment.

A more recent study detailed an atom transfer radical polymerization scheme (ATRP) for grafting NIPAAm with spatial graft densities gradients[81]. This study investigated effects of different surface densities on NIPAAm surface swelling, protein adsorption, cell attachment and detachment[81]. Results demonstrated that surface swelling alone did not induce cell attachment, but showed a stronger correlation between protein adsorption (primary & tertiary) and cell attachment and detachment[81]. These results challenge the dogmatic belief that cell detachment on NIPAAm is caused by surface swelling[68,82,83]. Taken together, the foregoing studies illustrate a few of the complexities about working with NIPAAm-based surfaces and demonstrate that while these systems have been extensively implemented, there is still uncertainty about cell attachment/detachment mechanisms on these surfaces.

Methods for controlling cell alignment

The effectiveness of bottom-up approaches to build a tissue structure depends upon the ability to mimic the cellular and extracellular micro-structure of native tissue. While cells can orient and align over short length scales, forming a tissue sheet *in vitro* with universal alignment of its component cells requires external stimuli such as mechanical stretch, micropatterning, micro-contact printing, and external directional flow to drive structural organization [84].

Micropatterned substrates use topographical patterns to induce cells to align via contact guidance based on physical cues provided by the pattern. The idea of contact guidance to control cellular organization is actually very old, first being proposed by Weiss and Hiscoe in 1948 while experimenting with nerve growth[85]. Since this initial discovery, many studies have demonstrated that micropatterned surfaces guide orientation of many different cell types including epithelial cells[86], fibroblasts[87] , osteoblasts[88], and vascular smooth muscle cells[89,90]. More recently, these techniques have been applied to tissue engineering in order to induce cellular alignment over longer length scales[90–92].

Experiments growing tissues using micropatterning techniques have demonstrated their limitations when growing cell sheets for long durations. Sarkar, *et al*. showed alignment in vascular smooth muscle cells, but only grew cells for 4 days, while Zahor *et al*. only grew mesenchymal stem cells for 2 days alignment[90,91]. However, in more recent studies we have shown that as cell sheets grow thicker the aligning effect of the micropattern was eventually lost[93]. These results thus demonstrate that micropatterning can be used to induce cellular alignment, but only if the cells are grown for short time intervals, and only if the resultant sheet is comprised of a single layer of cells.

Micro-contact printing of extra-cellular matrix proteins onto flat substrates also induces cells to align in the direction of the printed shape. In an experiment within our laboratory, fibronectin was micro-contact printed onto the surface of an UpCell (commercially available NIPAAm dishes) dish forming an array of fibronectin lanes separated by regions with no adsorbed protein[94]. Because NIPAAm-coated surfaces are incapable of supporting cell attachment without adsorbed proteins, cells seeded in serum-free media adhere only to the fibronectin lanes and align in the direction of the lane[71,81,94]. However, unlike micropatterning, cellular alignment reorients as the cells remodel their local micro-environment[95]. Because cells realign on the matrix-printed substrates, it is preferable to seed cells on a micro-textured substrates whenever feasible.

Mechanical stretching offers a potent alternative for aligning cells by subjecting the cells on a substrate or embedded in a gel to cyclic loading[76,96]. Cyclic stretch typically applies a uniaxial load at 0.5–2 Hz from 2–20% strain to cells such as fibroblasts, endothelial, and smooth muscle cells that normally experience physiological stretch *in vivo* [97]. Typically, cells align perpendicular to the direction of cyclic stretch in order to minimize the strain experienced over the whole cell, and much effort has been devoted to understanding the underlying mechano-biology, including the development of mathematical models[98–100],[101]. In general, alignment depends upon the cycling frequency, stretching duration, and stretching magnitude. For example, vascular smooth muscle cell alignment has been induced within 24 hours, but after stopping stretching cells lose their alignment within 48 hours[102]. In another study, Kakasis *et al*. showed that vascular smooth muscle cell alignment depends upon stretch magnitude, yielding cells of variable alignment[103]. While these experiments show cellular alignment can be induced by cyclic strain, there are a number of disadvantages to this technique. Mechanical stretching requires complex, expensive equipment, is sensitive to stretching parameters (frequency, time duration, and stretching magnitude), and cellular alignment is lost after stretching stops, all of which make it that make it less attractive than simple micropatterning based methods.

Arterial Wall Mechanical Modeling

Designing a tissue engineered vascular graft purely by experimental characterization is time consuming and laborious. Therefore, we hypothesize that the design process can be aided by using computational techniques to model the mechanical response of cell sheets, allowing us to mathematically test modifications of cell sheet processing conditions and explore different stacking strategies. This integrated approach represents a step forward from traditional design methodologies used by the tissue engineering community that typically rely on empirical methods, and should provide a shorter path towards the successful development of a tissue engineered vascular graft.

Biomechanical models have traditionally been used to model native tissue to better understand pathological phenomena such as aneurysm development and atherogenesis[104]. For tissue engineering applications, though, their usefulness lies in ensuring that the materials used produce a functional tissue engineered blood vessel that replicates the performance of arteries *in vivo*, namely that the vessel wall should have a nonlinear stress-strain response curve and capable of withstanding significant loads[105,106]. Initial efforts at modeling tissue engineered vessels were purely phenomenological. The earliest such model, as described by Fung, was able to predict the nonlinear stress-strain response of soft tissue.[107] Fung noticed that the relationship between the stress and the derivative of stress with respect to stretch was linear. Although ground-breaking in its ability to capture the mechanical response of tissue, the Fung model offered limited predictive capability, likely because it and models that followed were based only on experimental data and do not capture the detailed physics of the system[107] This type of modeling still has value, though, because it can facilitate the higher order analysis of the stress-strain curves by smoothing the data, (e.g., allowing the extraction of more accurate incremental modulus).

Since then, many different phenomenological models have been developed and applied to modeling arterial tissue[108,109]. Most recently, researchers have developed models that incorporate the tissue microstructure into model formulations. These microstructural models are capable of predicting behavior, but are more complex, make significant assumptions, and require extensive microstructural characterization. One such example is a model developed by Holzapfel *et al.* where the direction of fiber alignment was incorporated into model formulation[18]. Phenomenological modeling also provided a tool to help identify the relative contribution of cells and the different extracellular matrix components such as collagen, elastin, and proteoglycans to the mechanical behavior of the tissue. For example, the impact of decreased elastin in knockout mice (Eln+/-) on aortic mechanics and fiber alignment was better predicted using constitutive models than from purely empirical mechanical measurements.

Mechanical modeling of native tissue mechanics also provides a framework for evaluating variability of experimental data. Holzapfel *et al.* experimentally measured the mechanical properties of 15 coronary arteries and then fit the experimental data using a phenomenological constitutive modeling framework.[27] Statistical analysis of the variability of the tissue mechanical behavior was done using the fitting parameters because the fitting parameters can be related to some feature of the underlying mechanical response.

The link between the microstructural and the macrostructural mechanical properties of a material is an active area of research within many engineering disciplines including tissue engineering. Empirical methodologies (e.g. building a structure and hoping that it has the right material properties) have driven most of the progress in the tissue engineering field, but are inefficient, laborious and expensive[110]. However, there has been recent progress towards modeling the link between the microstructural properties and macrostructural properties[104,111,112]. Dahl *et al.*, successfully applied a microstructurally motivated model developed by Lanir to describe the mechanical response of a tissue engineered vascular graft[109,113]. This most recent work provides the underlying premise for this dissertation.

Rationale for Specific Aims

This dissertation intends to develop and a bottom-up approach towards building a tissue engineered vascular graft to replace high-pressure small diameter vessels such as the carotid and coronary artery. To accomplish this goal, the work in this thesis is broken down into three specific aims. The first aim developed a novel force sensor design based upon a cantilevered thin beam design that uses a pair of coaxial magnets combined with a Hall-Effect sensor to measure beam tip displacement. This development overcame the limitations of the resolution of a strain gauge based force sensor used to collect prior data[93]. The second specific Aim uses a micropatterned, thermo-responsive PDMS-based substrate platform for the growth and culture of aligned vascular smooth muscle cell sheets. Recognizing that micropatterned substrates can induce cellular alignment with vascular smooth muscle cells for short time durations, but over time cell sheets will grow thicker and alignment will be lost[93], these sheets were grown to a minimal functional thickness. Aim 3 compares experimentally measured mechanics of aligned cell sheets to a constitutive model of the mechanics of arterial tissue.

The stacking arrangement and relative alignment of the cell sheets will have a significant impact upon the mechanical response of the cell sheets. Furthermore, as important as stacking is towards the response, the mechanical properties of individual cell sheets will also influence mechanics of the tissue structure. Therefore, computational studies can help drive the design process towards an optimal stacking methodology as well as an optimal processing technique that produces a cell sheet with the appropriate mechanical properties. A successful biomechanical model will inform the design process of the tissue engineered vascular patch.

Instead of using a synthetic scaffold to engineer a vascular graft, we propose a method that utilizes cell sheets – confluent layers of cells and extracellular matrix. One common method for growing and harvesting cell sheets involves using thermo-responsive substrates that allow cell attachment at incubator temperature and detach as the temperature is decreased. This method was pioneered by Okano *et al.*[71,114,115]. Based upon previous work within our lab, these cell sheets can be grown on micropatterned and microcontact printed substrates, and the cells align in a preferential direction[93,116]. We have also shown that cells grown on these surfaces can be detached and stacked to form multilayered cell sheet-based tissues[95]. Because the structure of the artery features layers of vascular smooth muscle cells and extracellular matrix with cells and extracellular matrix aligned in the same direction, cell sheets provide an excellent candidate material to replicate the native structure of the artery. As depicted in Figure 3 layering the cell sheets with the cellular and ECM alignment in different directions can produce a tissue that has a structure that mimics the native arterial structure. The layering patterns also have the potential to give the tissue the required mechanical behavior.

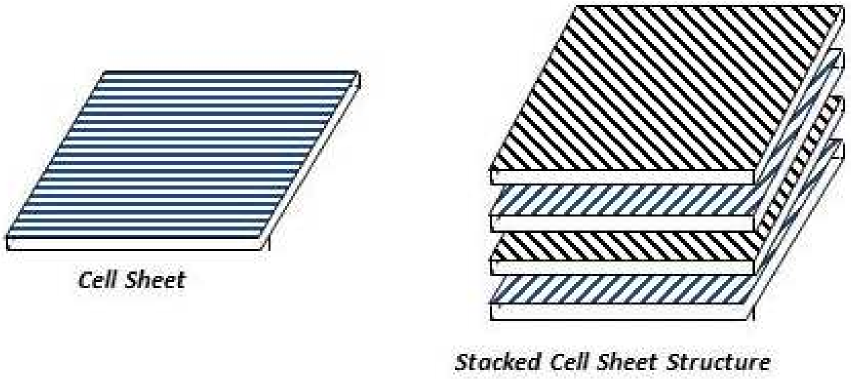

Figure 3: Cell sheets can be stacked to form multilayered constructs with controlled anisotropic mechanical properties. Cell sheet texture represents alignment direction of cells and extracellular matrix. Aligned cell sheets can be stacked with successive layers having different orientations to create a tissue with a hierarchal structure similar to native arterial tissue.

Chapter 2: A uniaxial tensile tester for measuring the mechanics of cell sheet based tissues

Introduction

Mechanical characterization of biological tissues and multi-layer tissue constructs can provide valuable information that helps guide, enhance, and accelerate tissue engineering development. Such characterization requires both mechanical testing devices and standard methods that measure the stress-strain behavior of *in vivo* biological materials, and testing must be capable of flexibly interrogating the complete stress-strain range for a spectrum of biological tissues, tissue constructs, and fibers. At very low forces, specialized equipment such as the Atomic Force Microscope (AFM) can provide valuable, highly localized, force data, whereas at the other extreme, conventional strain gauges and load cells can be applied to monitor macro stresses of greater magnitude[117]. However, there is a dearth of testing equipment and methods for mechanical testing in the force regime spanning 0.1 – 100 mN, yet it is this force range that is of greatest importance in the development of cell sheet-based technologies.

Measuring mechanical forces in biological materials is challenging. First, the stiffness of biological material varies widely, making it difficult to estimate the force testing ranges that these materials are able to withstand before testing. Second, the force ranges that these materials can withstand are often small, in a range where there are few commercial sensors. Commercial force sensors capable of measuring small forces are often limited to one force range, expensive, and not extensible. The wide force ranges needed when testing biological materials therefore make commercial force sensors unattractive options. Because of these limitations, we developed an inexpensive force sensor capable of measuring multiple force ranges and incorporated the sensor into a custom built uniaxial tensile tester. Using this sensor, we mechanically tested materials characterized by a wide range of mechanical properties: single layer cell sheets, silk fibers, and PDMS substrates.

To accomplish this, we set about designing a force sensor that specifically addresses the critical limitations of current force sensors. First, the force sensor design must be customizable, meaning that it can easily be modified to measure forces over a wider range of magnitudes, particularly in the sub-Newton regime. Second, sensor fabrication should be straightforward and avoid expensive materials and complex, costly manufacturing techniques. Third, the force sensor should integrate easily within a uniaxial tensile testing apparatus, having sufficient load-train stiffness to minimize strain rate errors associated with sensor compliance. The present research developed a mechanical testing apparatus and force sensor, the latter of which incorporates a thin cantilever beam in combination with a pair of magnets and a precision, ratiometric Hall-Effect integrated circuit (IC) magnetic field sensor.

Materials and Methods

Uniaxial Tensile Tester Design

Figure 4 depicts a simplified block diagram of the three major components of the uniaxial tensile tester: the test cell, the linear actuator and the force sensor. The test cell is comprised of an aqueous bath that hydrates tissue specimens during mechanical testing. The two ends of the tissue sample are attached to a pair of mounts in the testing bath using cyanoacrylate adhesive, thereby enabling connection of the tissue to the actuator and force sensor. The actuator is composed of a servomotor that drives a linear stage to stretch the tissue. The force sensor is composed of a thin, cantilevered brass beam mounted above the testing cell. An arm, connected to the mid-point of the beam, extends into the bath where it connects to the tissue mount. The beam extends beyond the tissue attachment point and a Hall-Effect IC sensor (Allegro Microsystems, model A1324) is permanently attached to the unloaded end of the beam and is positioned within the gap of the magnet yoke.

Each arm of the magnet yoke is fitted with a small (1/10" diameter and a 1/16" thick) axially magnetized, N42 Neodymium disc magnet (K&J Magnetics Inc.) with a residual magnetic induction of 1.32 Tesla. The linear actuator and testing cell use commercial-off-the-shelf (COTS) components that are commonly used in laboratory devices. Although the force sensor also uses COTS components, the manner in which the components are integrated and optimized is novel and a major focus of this thesis.

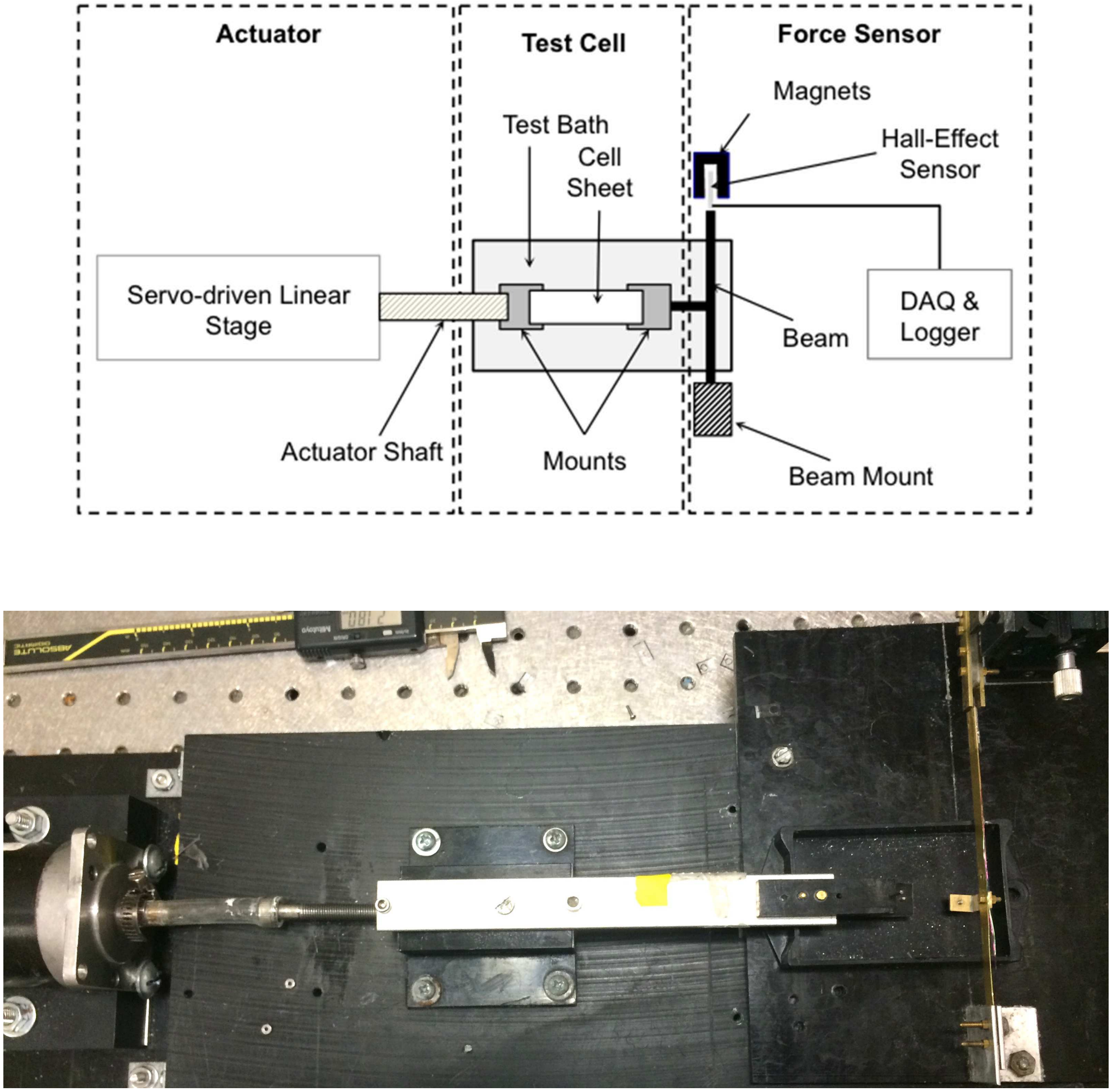

Figure 4: Uniaxial tensile tester schematic design consists of three device subsystems: actuator, test cell, and the force sensor. The actuator stretches the material, the test cell provides an aqueous bath for testing, and the force sensor measures forces.

Hall-Effect Integrated Circuit

The Hall effect, discovered in 1879 by Edwin Hall, relates to the observation that when current flows in an electrical conductor in the presence of a perpendicular magnetic field, a transverse electrical potential is produced in the conductor along a direction perpendicular to the magnetic field[118,119]. The Hall effect is schematically illustrated in Figure 5 for a semiconductor Hall element, which lies mutually perpendicular to both a magnetic field (**B**) and applied constant current (**i**). The resulting Lorenz force deflects the charge carriers (negative electrons and positive holes) in the semiconductor toward the opposing Hall electrodes, inducing an electrical potential between them. The magnitude of the induced potential, the Hall Voltage, is proportional to the vector cross product of the applied current and the magnetic field strength. The proportionality constant depends on the Hall element geometry and semiconductor material.

The Hall voltage is quite small, even for modern semiconducting materials, which produce an output on the order of 30 microvolts for a 1 gauss applied magnetic field. As a consequence, sensing of magnetic field strength using the Hall effect has only recently emerged as an economical, precision technology, via advances in semiconductor materials and the mass production of reliable low-cost integrated circuits (ICs). An IC Hall effect sensor includes an embedded Hall element(s), amplifier, and signal conditioner within a System-in-Package (SIP) module that measures approximately 3mm X 4mm X 1.5mm thick. Table 1 lists the specifications for the Allegro A1324 Hall effect sensor.

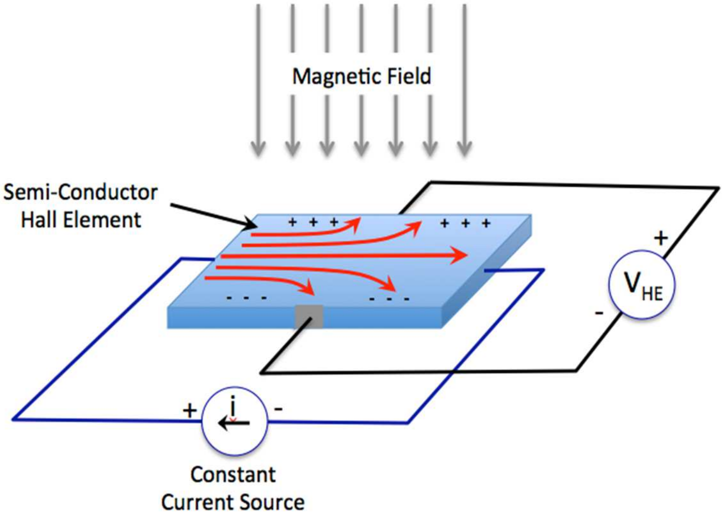

Figure 5: Hall-Effect Sensor Schematic.

Specification	Performance
Sensitivity	50 V/ Tesla
Voltage Output Range	0–5 Volts
Noise Level (p-p)	7 mV
Noise Level (RMS)	1.3 mV
Max Magnetic Field Strength	± 0.05 Tesla

Table 1: Hall-Effect Sensor specifications for A1324 Hall-Effect Integrated Circuit Sensor (Allegro Microsystems, Worcester, MA). Data taken from company supplied data-sheet.

Beam Design

The sensor design utilizes a cantilevered beam to measure forces. In order to effectively design the beam to have the desired mechanical properties, elementary beam bending mechanics was used to predict beam stiffness, beam tip displacement, angular bending and angular torsion. Equation 1 models beam deflection as a function of applied load, beam geometry and material[120].

$$w(x) = \frac{px^2\left(3L_p - x\right)}{6EI} \qquad \forall\, x < L_p \tag{1}$$

$$w(x) = \frac{pL_p^3}{3EI} + \frac{pL_p^2}{2EI}\left(x - L_p\right) \qquad \forall\, x > L_p$$

, where: p is the applied force, x is the position along the beam, L_p is the distance between the beam fixture to the loading point, and E is Young's modulus of the beam material. I is the moment of inertial of the beam and for a beam with a rectangular cross section $I = 1/12\, wt^3$ with a width of w and a thickness of t. The slope of the beam deflection can be described by taking the first derivative of the beam deflection equations i.e., $dw(x)/dx$. As the beam is not loaded along the neutral axis, the beam will twist with an angle of θ. The beam rotation caused by loading the beam off the neutral axis is modeled the strength of materials approximation shown in Equation 2[120].

$$\theta = \frac{2(1+\nu)T}{k_1 Ehb^3}x \tag{2}$$

, where:

$$k_1 = \frac{1}{3}\left[1 - \frac{192}{\pi^5}\frac{b}{h}\right]\sum_{n=1,3,5,\ldots}^{\infty}\frac{1}{n^5}\tanh\left(\frac{n\pi h}{2b}\right)$$

, and T is the torque applied to the beam, v is the Poisson ratio of the beam material, E is Young's modulus, h is the beam width, b is the beam thickness, and x is the position along the length of the beam. For this beam design, $T = p*d$, where p is the applied load and d is the distance between the beam's neutral axis and the location of the applied load.

Magnet & Hall-Effect Sensor Design

The magnetic flux density along the axis of symmetry of a single, axially magnetized, cylindrical disc magnet can be modeled by the following analytical approximation.

$$B(z) = \frac{\mu M}{2}\left[\frac{h-z}{\sqrt{r^2+(h-z)^2}} + \frac{z}{\sqrt{r^2+z^2}}\right] \tag{3}$$

M represents the magnetization vector of the magnet, h is the thickness of the magnet, r is the radius, μ is the magnetic susceptibility, and z represents the distance from the magnet surface. Because the magnetic field equations are linear, the magnetic field produced by multiple magnets separated by a gap, δ, can be modeled by superimposing the magnetic field generated by individual opposing magnets as expressed in Equation 4.

$$B_t(z,\delta) = B(z) - B(z+\delta) \tag{4}$$

Beam Calibration

The force sensors were calibrated experimentally to determine the relationship between sensor voltage output and applied load. The beams were mounted vertically, and masses were attached to the beam loading point with each calibration experiment being repeated six times. Sensor voltage output was recorded as a function of applied load and fit using linear regression in MATLAB (Mathworks, Natick, MA) to determine the beam stiffness (mN/V). The slope of the linear fit corresponds to the beam stiffness (mN/V), and the force range is calculated using the 5 Volt output range of the Hall-Effect sensor multiplied by the beam stiffness.

Cell Sheet Culture

Bovine vascular smooth muscle cells were cultured in low glucose Dulbecco's Modified Eagle Medium (Life Technologies) and supplemented with 10% fetal bovine serum (Hyclone) and 1% antibiotics (Life Technologies) and 1% L-Glutamine (Life Technologies). Cells were seeded at a density of 55,000 cells per cm^2 onto flat thermo-responsive PDMS substrates as previously published[93]. Growth medium was supplemented with 50 μg/mL of ascorbic acid daily after the cells formed a confluent monolayer. Cell sheets were cultured for 14 days before detachment and mechanical characterization. Silk fibers were prepared as previously described[121].

Mechanical Characterization

Bovine vascular smooth muscle cell sheets were detached from micropatterned substrates. Cell sheets were prepared for mechanical characterization by cutting multiple samples from individual cell sheets. Samples were then loaded into a custom-built uniaxial tensile tester fitted with the Hall-Effect force sensor. Each sample was pulled for three pre-stress cycles to 20% strain at a strain rate of 0.05/second. Cell sheets were then pulled to failure at a strain rate of 0.05/second. Engineering failure stress and strain were measured and the Young's modulus was determined over the linear regime of the stress-strain curve. The silk fibers were mechanically characterized by mounting the fibers in the uniaxial tensile tester and stretching the fibers to failure at a strain rate of 0.01/second.

Results

Optimal Hall-Effect Sensor and Magnet Configuration

The optimal magnet and Hall-Effect sensor configuration needed to satisfy three basic design criteria in order it to be a suitable force sensor. First, the magnetic field ideally should be linear ($dB(z)/dz = K$) when the magnetic flux density is within the range of -0.05 to 0.05 Tesla to avoid saturating the Hall-Effect sensor. Secondly, the magnetic flux density gradient should be maximized to minimize beam displacement. Lastly, the Hall-Effect sensor should never make contact with the magnets. The optimal magnet combination depends upon magnet size, magnet residual flux density (magnetization) and spatial configuration of the magnets. Because magnetic fields are difficult to visualize, a combination of analytical models and COMSOL models were employed to determine the optimal magnet combination.

Single-Magnet Hall-Effect Sensor Configuration

Preliminary optimization studies attempted to use the magnetic field generated by a single magnet as the basis for the sensor design. Before using the analytical model for optimization studies, the model was validated by comparing the model output to the manufacturer’s own experimentally verified finite-element model-based output. Figure 6 plots the comparison between the two magnetic field model results for an axially magnetized Neodymium N42 disc magnet with a 1/10” diameter and 1/16” thickness as a function of distance from the magnet surface. The results show excellent agreement, indicated that application of the analytical model is appropriate. Figure 7 shows the magnetic flux density along the axis of symmetry based upon Equation 3 for the three magnets detailed in Table 2. At distances less than 1 mm from the surface of the magnet, the magnetic flux density is nearly linear, but unfortunately the magnetic field is too strong, causing sensor saturation. At distances further from the magnet, the magnetic field strength is weak enough to avoid saturating the Hall-Effect sensor, but now the magnetic flux density spatial variation in non-linear. Figure 9 plots the modeled Hall-Effect sensor output for this configuration where the sensor output is not only non-linear, but also unable to exploit the full Hall-Effect sensor output for all three magnets.

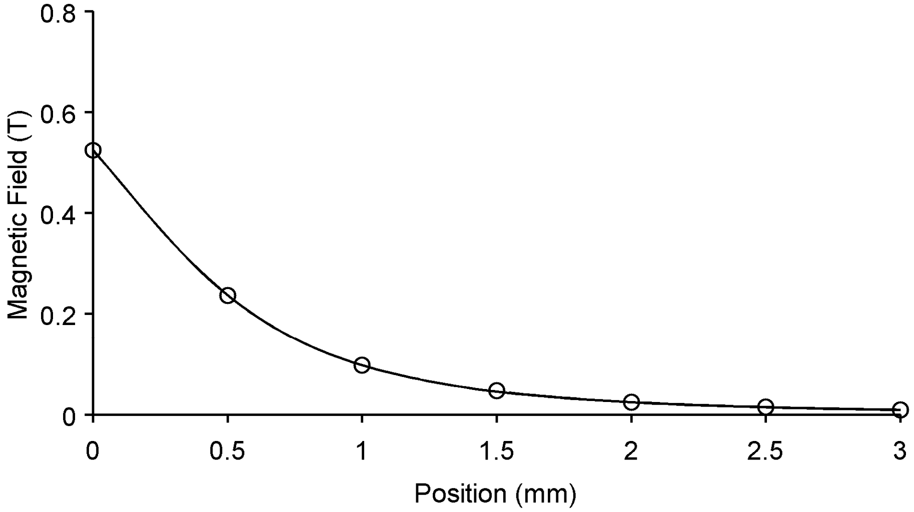

Figure 6: Comparison between analytical and finite element prediction of the magnetic field strength along the axis of a cylindrical Neodymium magnet (1/16" x 1/32", N52). The solid line represents the analytical solution as expressed in Equation 3 and the circles correspond to the finite-element prediction.

Line Type	**Residual Flux Density (T)**	**Diameter (inches)**	**Thickness (inches)**
Solid	1.48 T (N52)	1/16"	1/32"
Dashed	1.32 T (N42)	1/10"	1/32"
Gray	1.32 T (N42)	1/10"	1/16"

Table 2: Summary of physical and magnetic properties of rare earth Neodymium magnets used in the magnetic field calculations.

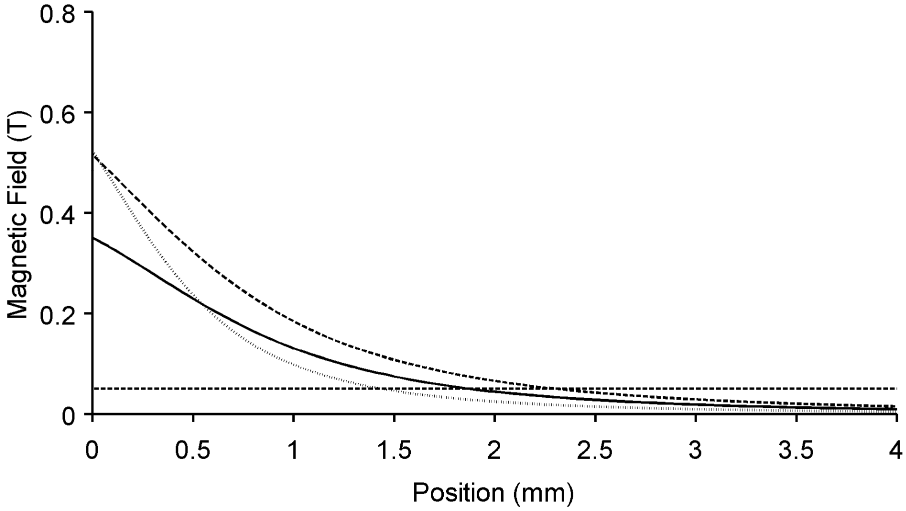

Figure 7: Axial magnetic field strength for single Neodymium magnets. Solid line: 1/10" x 1/32" - N52, dashed: 1/10" x 1/32" - N42, grey: 1/16" x 1/32" – N42 (diameter x thickness – Magnet Rating). Horizontal line depicts the saturation magnetic field strength for the Hall-Effect sensor.

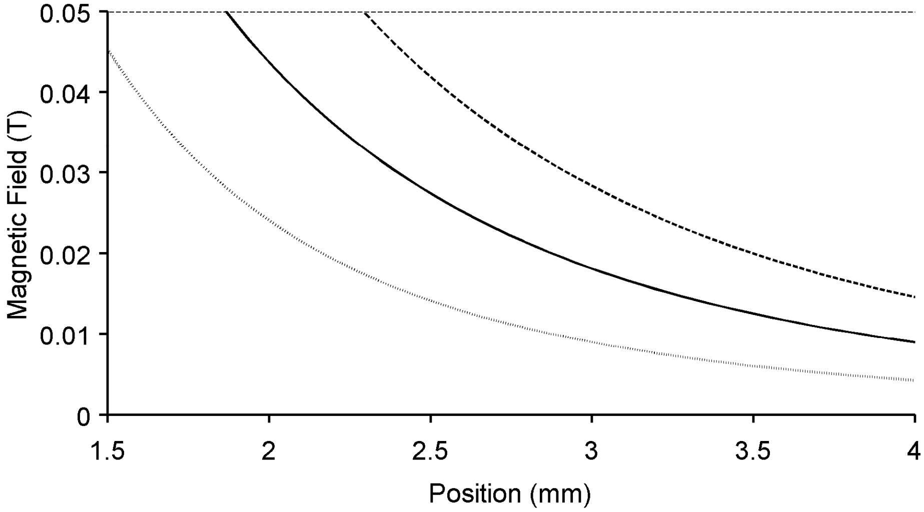

Figure 8: Axial magnetic field intensity along the axis of symmetry single Neodymium magnets. Solid line: 1/10" x 1/32" - N52, dashed: 1/10" x 1/32" - N42, dash-dot: 1/16" x 1/32" – N42 (diameter x thickness – Magnet Rating).

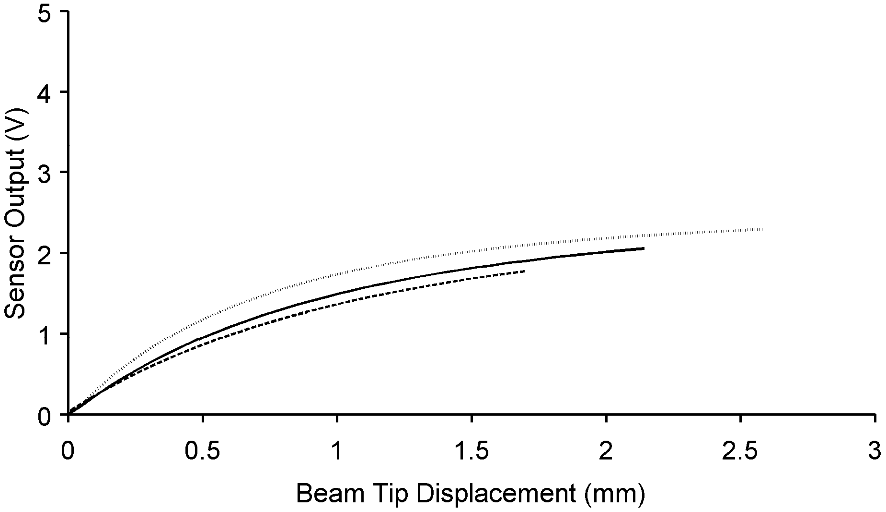

Figure 9: Hall-Effect voltage sensor output for 1 Neodymium magnet. Solid line: 1/10” x 1/32” - N52, dashed: 1/10” x 1/32” - N42, dash-dot: 1/16” x 1/32” – N42 (diameter x thickness – Magnet Rating).

Two-Magnet Hall-Effect Sensor Configuration

A linear magnetic flux density can be created by affixing two identical magnets separated coaxially with like poles facing each other. Furthermore, the magnetic flux density will have a magnitude of zero at the mid-point between the two magnets. Therefore, this magnet configuration meets the first set of criteria for the optimal design. Figure 10A describes the magnetic flux density as a function of position for a pair of N42 magnets with 1/10” diameter and 1/16” thickness magnets separated by 2.0, 2.25, 2.5, 2.75, 3.0 mm. As can be seen in this figure, the magnetic field gradient is largest when the magnets are closer together, and this result is universally true. Figure 10B plots the linear Hall-Effect sensor output voltage as a function of position. Because the magnetic field produced by a pair of cylindrical magnets depends upon the magnet size (diameter and thickness), residual flux density (magnetization), and magnet spacing, the optimal magnetic field gradient was determined by analytically modeling the magnetic flux density of pairs of commercially available disc magnets while varying gap thickness between the magnets.

Unfortunately, many of the steepest magnetic flux densities were unable to satisfy the final design criteria for the sensor design because the Hall-Effect sensor would physically contact one of the magnets, preventing utilization of the full sensor output. Figure 11 shows a schematic with dimensions of the magnetic yoke on the force sensor. Equation 5 was derived to predict the minimum physical gap between the magnet and Hall-Effect sensor that avoids saturation.

$$\Delta h = \frac{\delta}{2} - \left(1 + \frac{\Delta z_{sat}}{2}\right) \qquad (5)$$

, where: Δh is the predicted gap between the Hall-Effect sensor and magnet at full sensor output and δ is the distance between the two opposing magnets. $\boldsymbol{\Delta z_{sat}}$ is the displacement between the two positions where the Hall-Effect sensor saturates. Equation 6 provides a formal definition for $\boldsymbol{\Delta z_{sat}}$.

$$\begin{aligned} &\mathrm{z}_{\mathrm{sat}} = \mathrm{z}_{+} - \mathrm{z}_{-} \\ &B(\mathrm{z}_{+}) = \mathrm{B}_{sat+} = 0.05\,T \qquad (6) \\ &B(\mathrm{z}_{+}) = \mathrm{B}_{sat-} = -0.05\,T \end{aligned}$$

Any magnet configuration that has a negative gap spacing (Δh) indicates that the full sensor output is impossible due to magnet and sensor interference (collision), while a value greater than zero is physically possible. It was anticipated that differences would exist between the theoretical magnetic field predictions and actual magnetic fields. Therefore, the gap between the magnets was designed to be larger than the lowest theoretical prediction. Based upon this analysis, the magnet configuration that best satisfied the design criteria was determined to be a pair of 0.1" diameter, 0.1/16" thick, N42 Neodymium magnets with a separation between the magnets of 2.75 mm. With this configuration, the Hall-Effect sensor would produce full sensor output (5 Volts) over an approximate distance of 350μm.

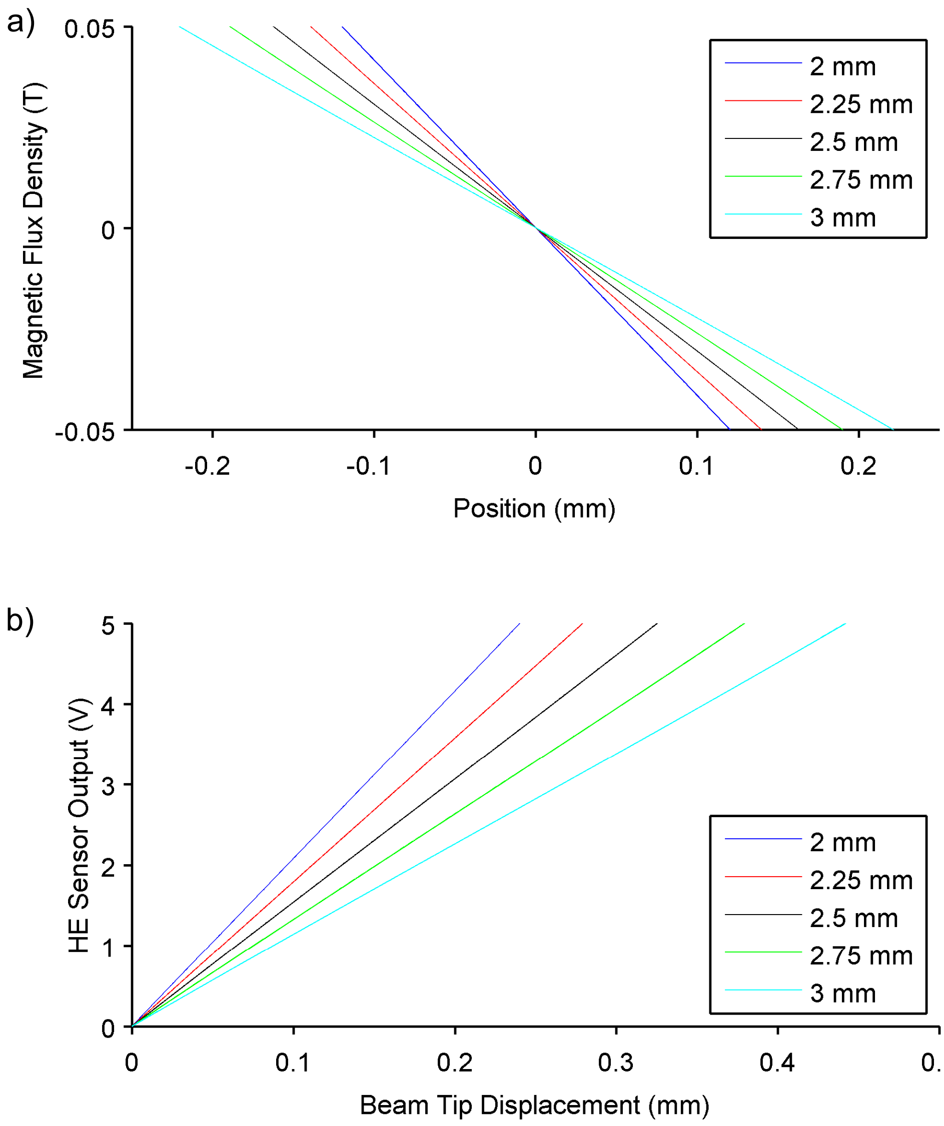

Figure 10 a) Axial magnetic field strength for a pair of Neodymium disc magnets (1/10" diameter, 1/16" thick, N42) separated by different gap spacing with poles facing. The legend represents the gap size between the magnets. Plot is centered at the mid-point between the magnets. b) Hall-Effect sensor output voltage as a function of beam tip displacement when mounted on a force sensor. The legend represents the gap size between the magnets.

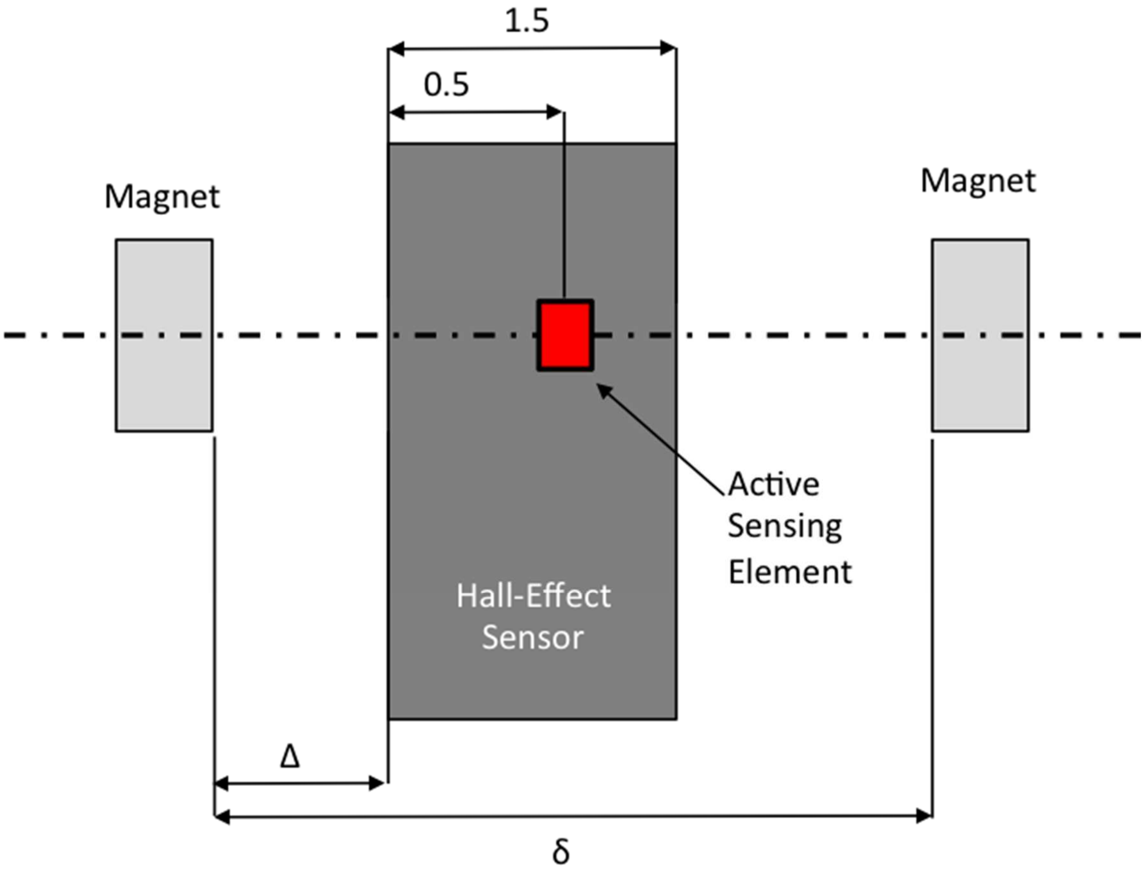

Figure 11: Paired Magnet Hall-Effect Sensor Configuration: A pair of magnets with like poles facing surround a Hall-Effect sensor. The Hall-Effect sensor's active sensing element (red) is embedded approximately 0.5 mm beneath the face of the sensor and approximately 1.0 mm from the back face of the sensor. The active sensing element is coaxially aligned with the two magnets.

Beam Design

The results from the previous magnetic field optimization studies provide design parameters with which to design beams required for the desired force measurement ranges. Figure 14 contains a plot of beam deflection for a 0.01” thick, ¼” wide, 4” long brass beam subject to a 5 mN load as predicted by Equation 1. The load is applied 1.5” from the base of the beam and 3/8” below the neutral axis of the beam. The brass has a nominal Young’s modulus of 110 GPa and a Poisson’s ratio of 0.35. Under the same loading conditions, Figure 15 plots the angular beam deformation caused by beam bending (solid line) as well as the angular beam deformation caused by torsional loading (dashed). A schematic description of the two bending modes is shown in Figure 13. The angular deformation caused by beam bending increases along the length of the beam until the loading point at which point the angular deformation becomes constant. This angular rotation cannot be avoided and is caused by merely loading the beam. Similar to the bending angular rotation, the torsional rotation increases linearly with position along the beam length as predicted by Equation 2. At the loading point, the torsional rotation becomes constant. This rotation occurs because the beam is loaded off the neutral axis, creating a torque on the beam, and is a result of the beam design. Interestingly, the torsional rotation caused by loading the beam below the beam’s neutral axis is predicted to be significantly smaller than the angular rotation due to beam bending. This result suggests that the deliberate design choice to load the beam below the neutral axis will not significantly impair measurement quality due to torsional beam rotation. Based on Equation 1 the beam shape due to normal beam bending will not change for different beams of different thickness. Unfortunately, the torsional beam rotation beam depends upon the geometry and material properties of the beam when modeled using Equation 2. Although there are differences, they are small for beams composed of the same material.

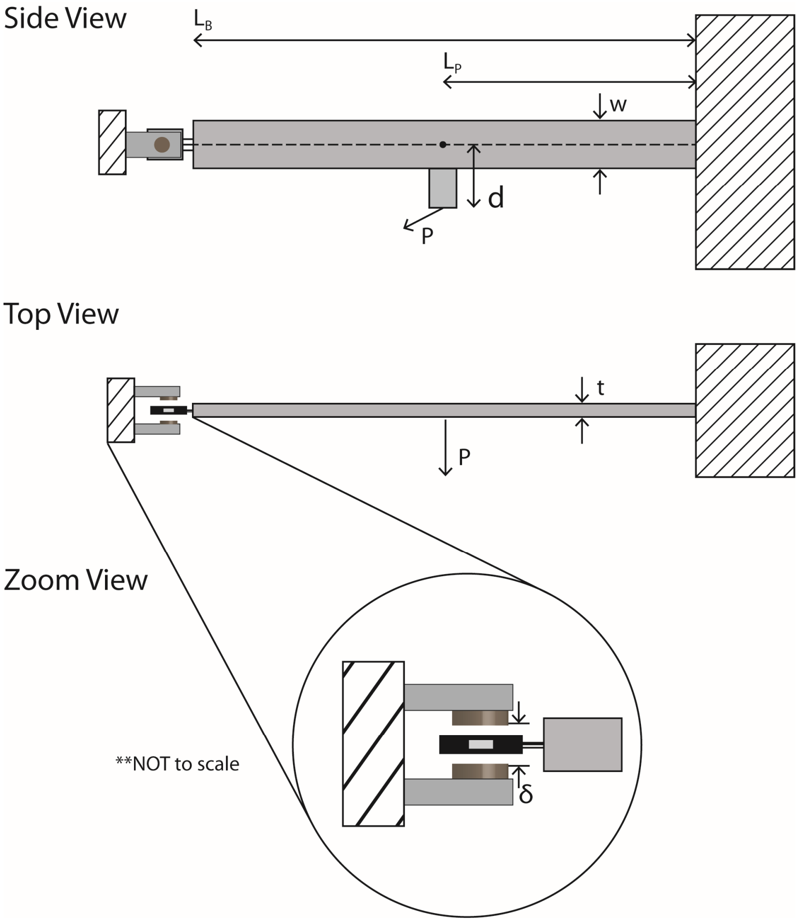

Figure 12: Design Schematic for the Hall-Effect force sensor design.

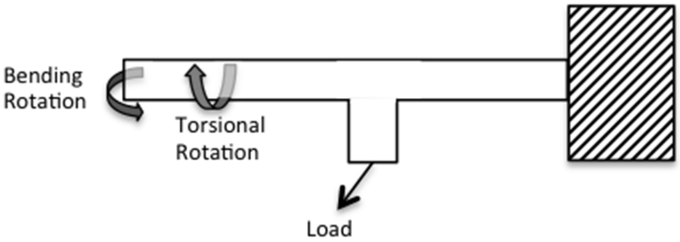

Figure 13: Angular beam rotation of a cantilevered beam when loaded off axis. Beam rotation can be decomposed into the bending rotation and the torsional rotation caused by off axis loading.

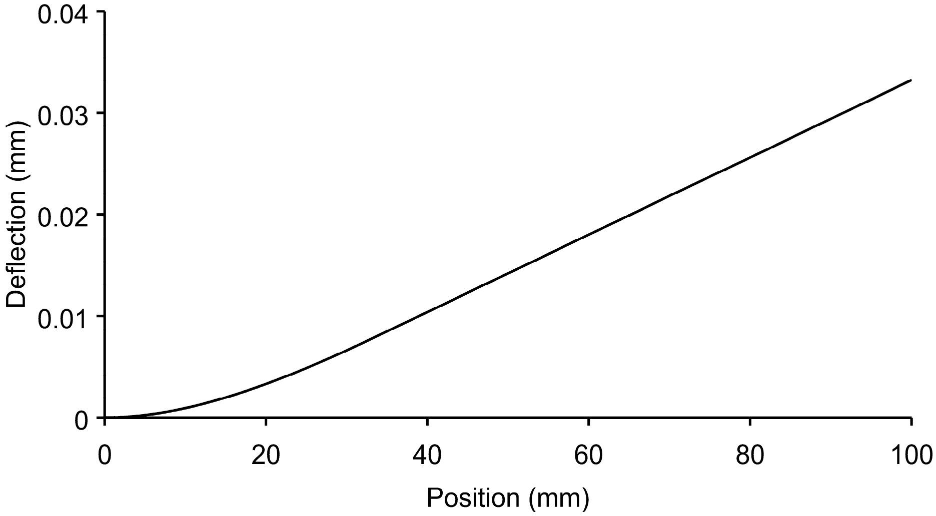

Figure 14: Beam Deflection along the length of the beam (Brass, 0.01” thick, 0.25” wide) with a 5 mN load applied at 38.8 mm.

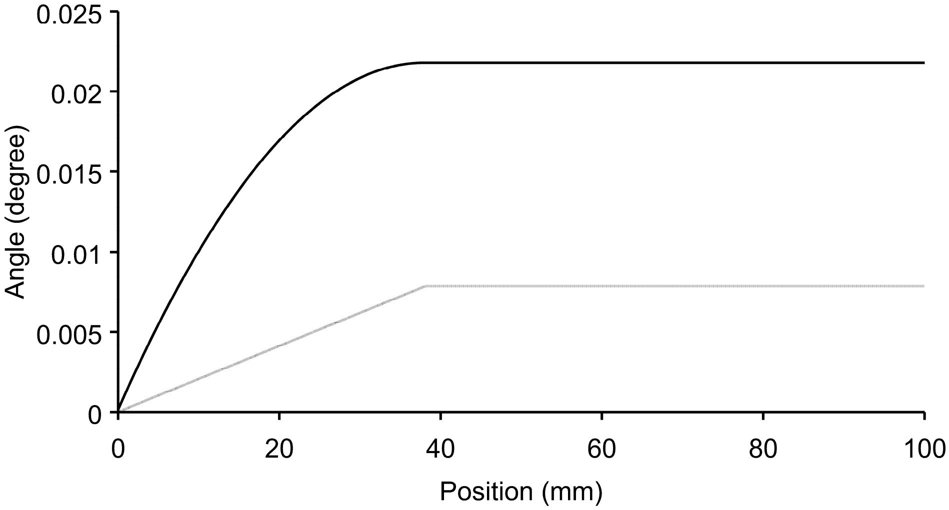

Figure 15: Beam Angular Deformation along the length of the beam (Brass, 0.01” thick, 0.25” wide) with a 5 mN load applied at 38.8 mm. Solid line represents the slope of the beam caused by beam bending and dashed line represents angular torsion caused by off axis loading.

Beam Calibration

The results from the magnetic field modeling analysis and the beam bending analysis formed the basis for the development of four force sensors capable of measuring four different force ranges. Based upon the results, four beams were built using brass of varying thickness (0.01”, 0.016”, 0.02”, 0.024”). Figure 16 plots calibration results for each of the four sensors including an overlay of the linear regression results for each of the four sensors. The standard error of estimate for the linear regression analysis is 0.028, 0.043, 0.093, 0.192 mN for the B10, B16, B20, B24 force sensors, respectively.

Mechanical Characterization

Single layer bovine vascular smooth muscle cell sheets and silk fibers were mechanically characterized using the Hall-Effect based force sensor. Figure 17a plots the raw force data for a single layer bovine vascular smooth muscle cell sheet as a function of strain. Normalizing by the cross-sectional area of the cell sheet indicated that the cell sheet failed at a corresponding stress of 400 kPa and a Young’s modulus of 1.6 MPa. Figure 17b also shows force sensor output for the mechanical characterization of an individual silk fiber. The force-elongation curve shows the silk fiber bearing no load, followed by a sharp, linear force curve. When converted from force to stress, it is estimated that the silk fiber fails at 8 kPa and has a Young’s modulus of 10 kPa.

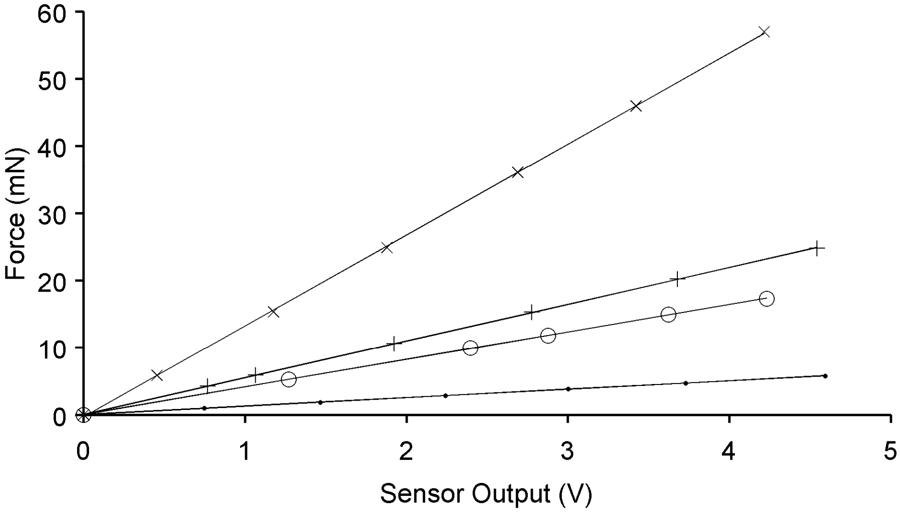

Figure 16: Hall-Effect force sensor calibration results for the B10 (dot), B16 (o), B20 (+) and B24 (x) sensors (sensor details are documented in Table 3 below) Solid lines represent the linear regression fit for each of the different sensors (N=6).

Specification	**B10**	**B16**	**B20**	**B24**
Material	Brass	Brass	Brass	Brass
Beam Size	4” x ¼” x 0.01”	4” x ¼” x 0.016”	4” x ¼” x 0.020”	4” x ¼” x 0.024”
Sensitivity [mN/V]	1.258	4.0967	5.479	13.42
Regression fit (R^2)	0.9999	0.9999	0.9999	0.9997
Force Range [mN]	6.29	20.48	27.397	67.114
Resolution [µN]	1.6	5.33	7.12	17.06

Table 3: Summary of the Hall-Effect Force Sensor Calibration Experiments.

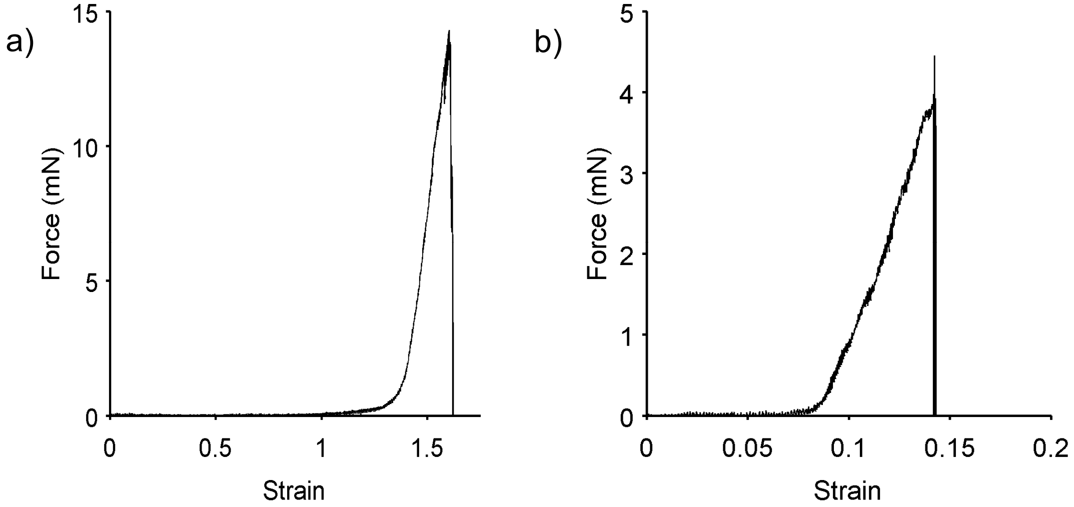

Figure 17: Example force-strain curves measured using the Hall-Effect force sensor (a) silk fibers and (b) single layer bovine vascular smooth muscle cell sheets.

Discussion

This work has developed an accurate, inexpensive biomechanical force sensor that is easy to manufacture and adaptable to measure forces in multiple ranges. Each force sensor can be quickly manufactured without expensive or complex fabrication methods, and the force range can be tailored for a specific application by changing the material or dimensions of the thin cantilever beam. The Hall-Effect sensor and magnets are inexpensive about \$2 and \$0.20 respectively.

The uniaxial tensile testing apparatus was designed to incorporate standardized, commercial components wherever possible. For example, the linear actuator and testing cell are based upon COTS components. The specific force range needed to characterize the cell sheet tissue constructs is often not known *a priori*. This lack of information can preclude the option of purchasing an expensive commercially available force sensor with limited force measurement range. For example for our mechanical characterization research, the force range required to mechanically characterize cell sheet-based tissue samples could vary by several orders of magnitude, given the expected strength differences between single layer cell sheet and multi-layered cell sheet tissues. Therefore, it was preferable to build a custom force sensor with a design that could be easily modified to measure forces in different force ranges. Such an approach enabled building force sensors on demand quickly, inexpensively, and without complex manufacturing techniques.

Measuring the mechanical properties of a cell sheet based tissue via uniaxial tensile testing not only requires precise force measurements, but also accurate control and knowledge of the material strain and strain rate. As shown earlier in Figure 1, one end of the tissue is connected to the force sensor and the other end is connected to the linear actuator. The force sensor design uses deflection of a thin, cantilevered beam to measure forces, but the beam deflection must be accounted for in calculating the actual strain within the tissue. The actual tissue strain can be determined via the following equation:

$$\varepsilon_a = \varepsilon_i - \frac{d_f}{L_0} \qquad (7)$$

, where: ϵ_a represents the actual strain state of the tissue, ϵ_i represents the measured strain, and the second term on the right hand side of the equation is a strain correction. In this term d_f is the loading point deflection and L_0 is initial sample length. A stiffer force sensor would minimize d_f / L_0, leading to smaller beam displacement correction when determining the actual strain of the tissue. For example, when testing a cell sheet, the introduced by ignoring beam displacement is typically less than 1% and this error can be accounted for after mechanical testing using Equation 7. Incorporating a closed feedback loop system into the linear actuator that accounts for force sensor beam deflection could avoid strain correction, but it could also lead to further errors associated with electrical noise and inaccurate control parameters. Also, linear actuators experience backlash when changing direction, leading to decreased positional accuracy.

Cantilevered beam-based force sensors commonly use strain gauges or piezo-resistive elements as the active sensing elements. For example, wires within a strain gauge change resistance when strained. These sensors are mounted at the base (root) of the beam, the site of maximal surface strain. The strain on the surface of a beam increases linearly with the thickness of the beam when subject to the same beam deformation shape. Therefore, thin beams will have to undergo increased beam tip deflection to achieve similar ranges of surface strain as thicker beam and achieve similar level of force sensing performance as the Hall-Effect based force sensor design presented in this thesis. A commercial 200 mN strain gauge force sensor (Strain Measurement Devices) deflects greater than 2.2 mm at maximum load, which would create strain errors on the order of 20%. Furthermore, these sensors produce output voltages in the mV range and thereby require external signal conditioning (amplification and noise filtering) to generate voltage differences measurable by typical data acquisition (DAQ) systems. Also, the physical separation between the strain gage sensor and signal amplifier and conditioner makes these sensors susceptible to electromagnetic interference (EMI). The Hall-Effect sensor produces small voltages, but signal amplification and conditioning occurs within the integrated circuit package making them much less susceptible to EMI.

The sensor design presented here is not without limitations, although the limitations are common to other small force measurement techniques. Environmental mechanical noise is unavoidable, and this noise can significantly degrade measurement quality when measuring small forces. For our force sensor design, the cantilever beam is constructed using a thin, brass beam that has a low natural frequency of vibration and is strained in the fully elastic regime. When unaccounted for, mechanical noise has the potential to create modal vibrations that dampen slowly. Due to the low natural frequency of vibration, this sensor is unsuitable for dynamic force measurements.

Fortunately, it is possible to mitigate the environmental noise by conducting measurements on vibration isolation tables to account for mechanical vibrational noise and physically enclosing the apparatus to account for noise due to convective airflow. Because the beam funnels the noise into its natural vibrational noise frequencies, a low pass filter can be also used to significantly reduce vibrational noise. These issues are not unique to this sensor design, but are common issues that plague cantilevered beam force sensor designs in general, particularly when used in urban environments or in multi-story buildings.

The forces sensor described in this thesis is capable of measuring forces in the force range required to measure mechanical properties of a variety of biological materials, such as single layer cell sheets and silk fibers. The benefits of our design are numerous and significant: custom sensors can be manufactured quickly without the need for costly, complex manufacturing techniques and without sophisticated signal conditioning circuitry. Moreover, the sensor is stiff enough to minimize strain-related experimental errors common when making measurements with strain gauge-based force sensors. While the sensor presented in this thesis was designed to perform uniaxial tensile tests on biological samples, the general sensor could form the framework for sensors using different beam geometries and for applications beyond uniaxial tensile testing.

Chapter 3: Robust, thermo-responsive PDMS substrates for the growth of contractile, aligned, vascular smooth muscle cell sheets

Introduction

Cardiovascular disease remains a leading cause of mortality in the United States[6]. Designing tissue engineered constructs to properly function under physiological loads is essential for developing a functional replacement tissue[37]. Moreover, mechanical considerations are essential when engineering arterial tissue, because large hemodynamic forces can cause graft failure and cellular dysfunction[122]. It is known that the complex cellular and extracellular structure of the medial layer of an artery determines the nonlinear mechanical properties of arterial tissue[29]. Vascular smooth muscle cells and extracellular matrix within individual layers of the tunica media have been shown to align helically down the length of the artery with successive layers aligned in different directions[11]. Therefore, a tissue engineering strategy that replicates the native tissue structure has the potential to overcome problems such as anastomotic intimal hyperplasia and graft thrombosis that plague current strategies[123]. Here we hypothesize that this can be achieved with a bottom-up tissue engineering strategy using cell sheets – a confluent monolayer of cells and extracellular matrix – as the basic functional building block. Previously, we have shown that single layer, aligned vascular smooth muscle cell sheets can be cultured successfully to have similar structure as individual layers within the media of the artery[116]. Furthermore, we have shown that vascular smooth muscle cell sheets with structural alignment (cellular and extracellular) are stiffer in the direction of alignment than perpendicular to the direction of alignment[93].

Strategies for growing cell sheets can be based upon a number of different substrate technologies such as thermo-responsive substrates, enzymatically digested substrates, and thermo-responsive hydrogels. While these methods use different underlying substrate technology, cell sheets can be non-destructively harvested as an intact monolayer. Thermo-responsive substrates remain one of the most common cell sheet substrate technologies. Okano *et al.* developed a method to graft N-isopropylacrylamide (NIPAAm) onto tissue culture plastic using electron beam irradiation, creating a thermo-responsive surface that would allow cell attachment at 37ºC and cell detachment below 32ºC. Since this initial development, much work has been devoted to understanding the thermo-responsive nature of NIPAAm-based substrates.

Recently, we have shown that thermo-responsive poly-dimethylsiloxane (PDMS) substrate makes an ideal platform for culturing and harvesting arterial tissue[9–11]. PDMS substrates can easily be micropatterned, the substrate stiffness can be controlled, and the substrate can be stretched for mechanical conditioning[76,125]. In this study, we developed a method for the long-term culture of aligned, contractile, vascular smooth muscle cell sheets on thermo-responsive PDMS substrates and then showed that these cell sheets are both mechanically and structurally anisotropic. Building upon previous work in our lab, we used benzophenone to initiate the free radical polymerization of N-isopropylacrylamide onto the surface of PDMS substrates and showed that cell attachment correlates with NIPAAm surface density measurements. To allow the long-term culture of contractile, vascular smooth muscle cell sheets on these substrates, we coated the substrate surface with 3-aminopropyltriethoxysilane to vastly improve cell attachment and sheet formation. Using this substrate platform, we were able to grow non-patterned cell sheet and patterned cell sheets that are structurally and mechanically anisotropic. To our knowledge, this is the first demonstration of mechanical anisotropy in single layer, aligned cell sheets.

Methods

PDMS Substrate Preparation

Polydimethylsiloxane (PDMS) substrates were prepared by mixing PDMS base with PDMS curing agent (Dow Corning, Midland, MI) in a 10:1 ratio. The PDMS was then degassed under high vacuum until all bubbles had been removed. The PDMS mixture was then poured into either a 100 mm petri dish or a micropatterned silicon wafer and then degassed under high vacuum a second time. PDMS was then cured for at least 12 hours at 80˚C. Cured PDMS substrates were then cut into 4 x 2 cm substrates and rinsed with 2-propanol (Sigma-Aldrich, St Louis, MO). Micro-fabricated silicon wafers were prepared as previously described[125].

Free radical Polymerization of NIPAAm onto PDMS Surface

PDMS substrates were soaked in 20% [w/v] benzophenone in acetone for 3 min and immediately dried. Substrates were then rinsed with excess de-ionized water and then dried at room temperature for 60 min. N-isopropylacrylamide solution composed of 20%

[w/v] N-isopropylacrylamide (Acros Organics, Geel, Belgium), 0.5% benzyl alcohol (Sigma, St. Louis, MO), 5 mM sodium periodate (Sigma) was desiccated for 2 hr under vacuum. Substrates were then submerged under the NIPAAm solution and then placed inside an airtight grafting chamber that was purged of air for 1 min. To initiate the free radical polymerization of NIPAAm onto the PDMS surface, the substrates were then exposed to 55 mW/cm^2, 365 nm, UV irradiation for 3 min. The NIPAAm-coated PDMS (NIPAAm-PDMS) substrates were then immediately removed from the monomer solution and rinsed with excess deionized water. Subsequently, substrates were soaked in alternating solutions of acetone and ethanol to remove any excess benzophenone and NIPAAm monomer.

APTES Modification of NIPAAm-PDMS Surface

The surface of the NIPAAm-PDMS substrates was further modified by incorporating 3-aminopropyltriethoxysilane (APTES; Sigma) into the substrate surface. APTES solution was composed of 10% APTES solution [v/v] mixed with 200-proof ethanol and ‘activated’ with the addition 0.5% water to the solution. To incorporate APTES into the NIPAAm-PDMS surface, the substrates were submerged in APTES solution and baked at 80°C for 2 hours under vacuum. After APTES surface modification, the substrates were soaked in deionized water for multiple days to remove any excess APTES.

Diffusion Model of Benzophenone

A diffusion model was implemented to predict the concentration of benzophenone on the surface of the PDMS substrate. A schematic of the boundary of the diffusion model can be seen in Figure 19. Because the reservoir of benzophenone is much larger than the amount of BP solution imbibed in the substrate, the right boundary condition can be modeled as a constant concentration, Dirichlet boundary condition. The other side of the substrate is a zero flux boundary condition where $dC/dx = 0$. For these two boundary conditions, an analytical solution to Fick's law is well established. The total mass of absorbed benzophenone can be determined by integrating the analytical solution through the thickness for the different soaking times. Using the analytical results, we fit the experimental soaking data to determine the benzophenone diffusivity. We used this experimentally derived diffusion coefficient in a numerical model (finite difference) to show variation of benzophenone spatially and temporally for different experimental conditions. The numerical model used the boundary and initial conditions shown in Figure 19.

Surface Characterization of Substrates

Attenuated total reflection infrared spectroscopy (ATR-FTIR) data was collected using a Nicolet (Thermo-Fisher, Waltham, MA) spectrometer. Measurements were taken with a spectral resolution of 1.93 cm^{-1} over the range of 400 – 4000 cm^{-1}. The FTIR data were analyzed by taking the ratio of the 1650 cm^{-1} amide absorbance peak associated with the pNIPAAm to the 2900 methyl cm^{-1} peak associated with the PDMS. Surface concentration of NIPAAm was estimated by adsorbing known amounts of polymerized N-isopropylacrylamide (pNIPAAm) onto the surface of PDMS samples and measuring peak absorbance via FTIR. Water contact angle measurements were performed on a Kruss DSA100 Goniometer with a temperature controlled chamber (within 0.01ºC) connected to a Polyscience Digital Temperature Controller. Substrates were placed directly on the surface of the heating block and allowed to reach a constant temperature before water contact angle measurements were taken (N=8).

Cell Culture

Bovine vascular smooth muscle cells (bVSMCs) were acquired form Coriell (Camden, NJ). bVSMCs were cultured in low glucose Dulbucco's Modified Eagle Medium (Life Technologies, Grand Island, NY) supplemented with 10% fetal bovine serum (Hyclone, Logan, UT), 1% Anti-biotic/anti-mycotic (Life Technologies, Grand Island, NY), and 1% L-glutamine (Life-Technologies, Grand Island, NY) in an incubator at 37˚C and 5% CO_2. Cell sheets were treated with 50 µg/mL ascorbic acid (Sigma) after reaching confluence. Cells were passaged at 90% confluence and cells were only used within passages 9–13. NIPAAm-PDMS substrates were prepared for cell seeding by first incubating at 37˚C for 30 min and then by incubating the substrates in smooth muscle cell media for at least 2 hr. No special preparation was required for APTES-NIPAAm-PDMS substrates, and cells were directly seeded onto the substrates without pre-incubation. Bovine vascular smooth muscle cells were seeded onto the surface of flat and patterned substrates with a density of 45,000 cells/cm^2 and 60,000 cells/cm^2 cells, respectively. Different seeding densities were used to ensure that flat and patterned cell sheets would reach confluence at the same time. Cell sheets were grown for 1–2 weeks in culture before being detached. Cell sheets were transferred onto a gelatin mold composed of 7.5 % [w/v] Type A bovine gelatin dissolved into low glucose DMEM by incubating the cell sheet for 20 minutes at 4ºC.

F-Actin Staining

Cells sheets were rinsed with pre-warmed PBS and then fixed in 4% paraformaldehyde in PBS for 10 minutes at room temperature. Cell sheets were rinsed with PBS and then permeabilized with 0.1% Triton X-100 in PBS for 10 minutes. Cell sheets were then rinsed with PBS, blocked with 1% BSA for 1 hour. Cell sheets were stained with 1:100 FITC-phalloidin (Life Technologies, Grand Island, NY)) and 1:1000 Hoechst (Life Technologies, Grand Island, NY)) PBS containing 1% BSA for 1 hours. Samples were rinsed with 1% BSA in PBS and then rinsed with PBS. Samples were then imaged on an Axiovert S100 microscope (Zeiss, Germany).

Cell Alignment Quantification

Cellular alignment was quantified by applying a 2D Fast Fourier Transform (FFT) based method to images of the cellular F-actin structure using a previously published method[126].

Images of the F-actin structure were converted into the Fourier domain in ImageJ (NIH, Bethesda, MD), which produces output that indicate the dominant direction of the F-Actin. To determine predominant direction of the F-actin fibers, image intensity was summed in the different radial directions using the Oval Profile Plot ImageJ plugin. These data were normalized to produce fiber alignment probability distribution over the different angular directions from 0 to 180 degrees.

Results

Preparation of Thermo-Responsive PDMS substrates

NIPAAm is grafted to PDMS substrates via free radical polymerization using benzophenone to initiate the reaction. It has been established the ability of cells to adhere to a NIPAAm-coated surface depends upon the length and surface density of NIPAAm chains[71,127]. Control of the surface density of NIPAAm chains on the PDMS surface depends upon being able to control the surface density of benzophenone. To understand the relationship between soaking time and surface concentration of benzophenone, we experimentally measured the amount of benzophenone absorbed into the PDMS bulk by measuring UV absorbance at 345 nm. Figure 18 shows the total molar mass of benzophenone absorbed into the PDMS bulk for different soaking times and solvents (ethanol and acetone). The total amount of benzophenone absorbed into the bulk of the PDMS substrate increases with soaking time and benzophenone absorption is faster when dissolved in acetone compared to ethanol. In both solvents, the initial rate of absorption is quite fast, but slows down at longer soaking times. Next, we estimated the diffusion coefficient of benzophenone in dry PDMS by fitting the experimental data with the modeling results from an analytical model of 1-D diffusion as discussed previously. As shown in Figure 18, this computational prediction shows reasonable agreement with experimental data. The diffusion coefficient was determined to be 1.5^{-12} m^2/s and 0.9^{-12} m^2/s for benzophenone dissolved in acetone and pure ethanol, respectively. The difference in benzophenone absorption mirrors differences in the diffusion coefficient of pure ethanol and acetone into pure PDMS[128]. Figure 20 shows results from the diffusion simulations. In Figure 20, panel-a shows the initial concentration profile of the benzophenone through the thickness immediately after soaking the substrates for 1–9 minutes in 20% [w/v] benzophenone in acetone. Panel-b shows the evolution of the concentration profile after air drying for 60 minutes. Panel-c shows the evolution of the surface concentration of benzophenone over a 60 minute dry time, and panel-d shows the surface concentration as a function of soak time when dried for 60 minutes. The model simulation results are important for several reasons. First, having this information simplified the number of processing conditions by clarifying the interrelationships among soaking time, benzophenone concentration and drying time parameters and by providing an estimate for the resulting surface concentration of benzophenone for various combinations of processing conditions. It also enabled the ultimate selection of robust processing conditions that were less sensitive to sequence timing.

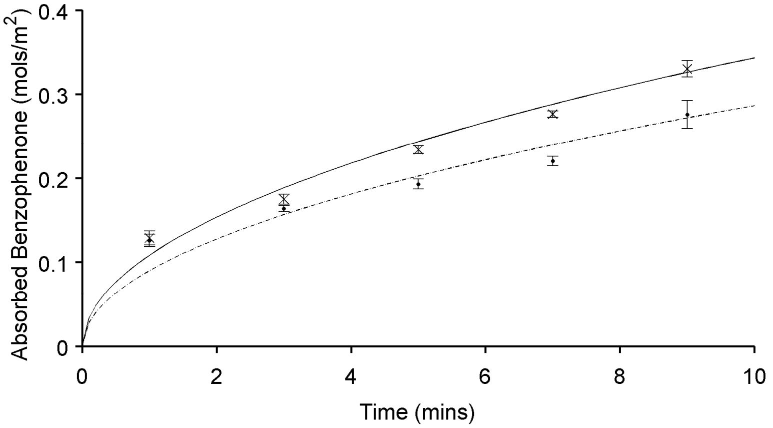

Figure 18: Molar mass of benzophenone absorbed into PDMS bulk when soaked in 20% [w/v] benzophenone dissolved in acetone (solid) or pure ethanol (dashed) for different time durations.

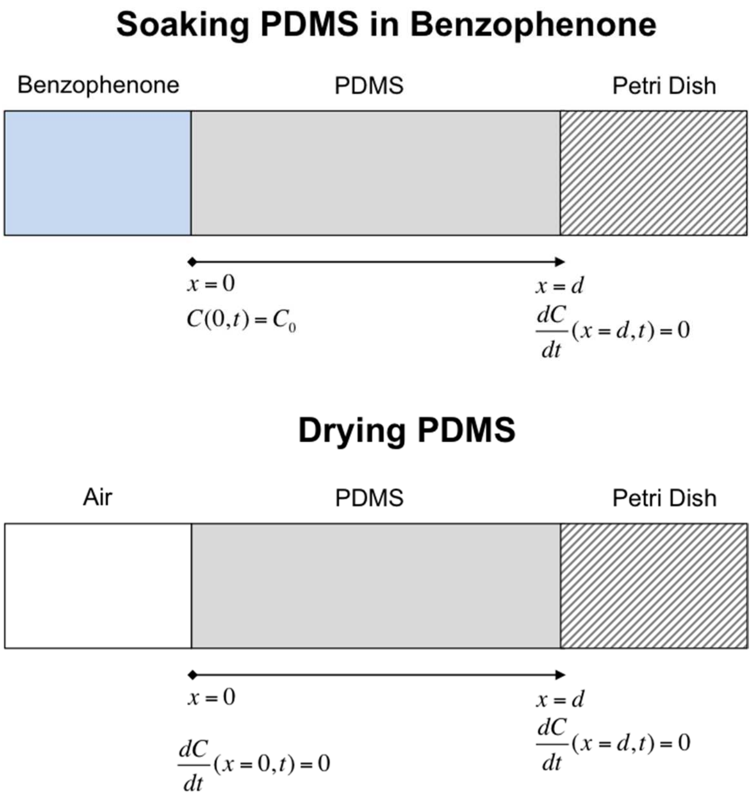

Figure 19: Boundary conditions for the finite different model of the diffusion of benzophenone into the PDMS bulk and diffusion of benzophenone during substrates drying. Top: During benzophenone soaking the PDMS surface exposed to benzophenone solution. Bottom: During drying one face is exposed to air allowing the evaporation of imbibed acetone, while the other face is bounded by the petri dish.

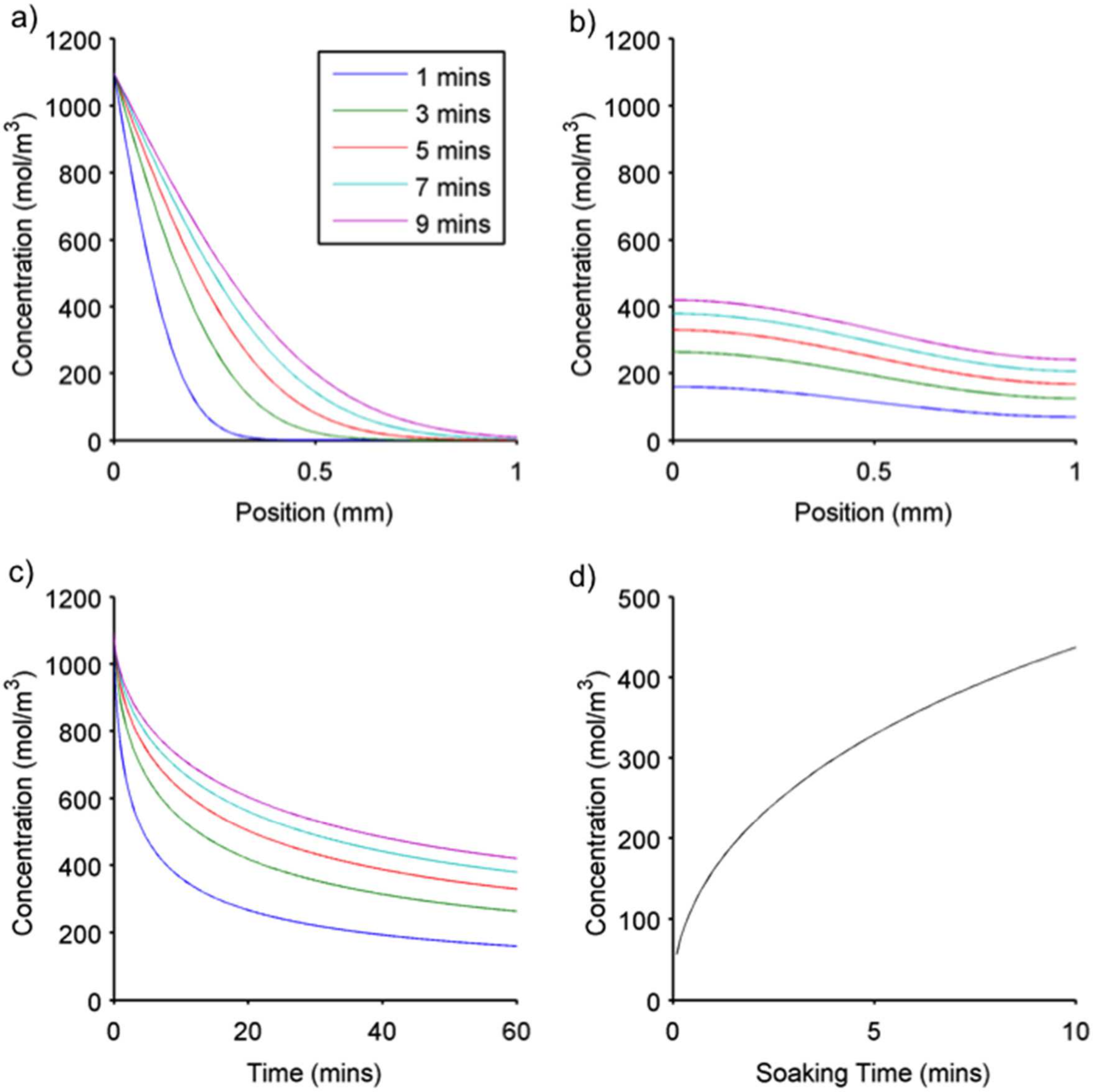

Figure 20: Benzophenone concentration through the thickness of a 1 mm thick PDMS substrate immediately after soaking in a 20% [w/v] benzophenone solution for 1,3,5,7 and 9 minutes (a) immediately after soaking the substrates and (b) 60 minutes after drying the substrates. (c) Surface concentration of benzophenone for different soaking times (d) Surface concentration of benzophenone for different soaking time durations after 60 minute dry time.

Benzophenone Diffusion into PDMS

The experimentally measured diffusion coefficient for benzophenone (in acetone) into PDMS is larger than previously reported measurements[128]. This difference was actually expected because in our experiments the benzophenone was diffusing into dry PDMS, whereas previous reports used PDMS that had been soaked in acetone before exposure to benzophenone. The development and experimental validation of a diffusion model of photo-initiator is essential for understanding how PDMS geometry impacts the surface concentration. This is important not only for flat substrates, but even more for other geometries such micropatterned substrates because our ultimate goal is to produce cell sheets with anisotropic properties to mimic native tissue.

Figure 21 shows representative transmission spectra for bare PDMS and NIPAAm grafted PDMS. Both the blank PDMS and NIPAAm-PDMS substrates show an absorbance peak around 2900 cm^{-1}, corresponding to C-H stretching within the methyl groups of the PDMS. NIPAAm-PDMS substrate FT-IR spectra shows clear peaks at 1650 cm^{-1} and 1540 cm^{-1} that correspond to the C=O stretching and N-H bending within the NIPAAm structure, respectively. The broad peak near 3300 cm^{-1} corresponds to the N-H stretching within the NIPAAm.

We determined the relationship between the surface initiator density of benzophenone and the eventual surface graft density of NIPAAm after UV exposure. This was achieved by soaking PDMS substrates in benzophenone for different time durations and then exposing the substrates to 2 and 3 min of UV irradiation. Figure 22 shows the representative FT-IR spectra for PDMS after UV exposure for several of the different grafting conditions. The grafting conditions are labeled, BPx-UVy where x and y correspond to the time duration in minutes of exposure. NIPAAm grafting on the PDMS surface was measured using FT-IR spectroscopy.

To quantify the surface graft density of NIPAAm on the PDMS surface, polymerized NIPAAm (pNIPAAm) was adsorbed onto the surface of PDMS substrate, and the FT-IR ratio between the 1650 cm^{-1} NIPAAm absorbance peak and the 2900 cm^{-1} PDMS absorbance peak was measured. The relationship between pNIPAAm surface density and FT-IR ratio was fit using linear regression (R^2= 0.9893), yielding a direct method of measuring NIPAAm surface density. Figure 23 plots the surface density of NIPAAm as a function of benzophenone soaking time and as expected, increasing the initial surface concentration of benzophenone leads to increased surface graft density of NIPAAm under the same UV exposure time. Similarly, when the substrates are exposed to longer UV exposure durations, the graft density of NIPAAm on the surface increases. This data suggests that we have the ability to control the surface graft density of NIPAAm onto the surface of PDMS with reasonable control.

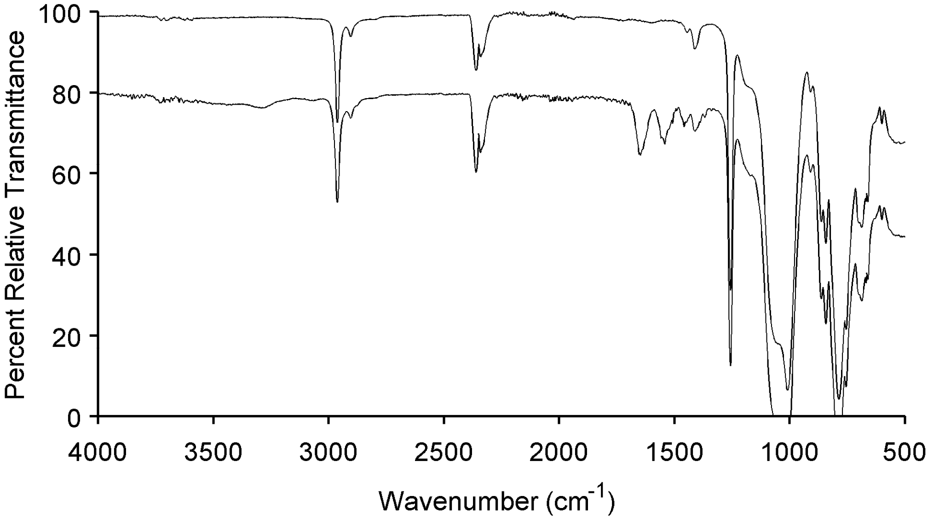

Figure 21: Fourier Transformed Infrared Spectrum for blank PDMS (top) and NIPAAm grafted PDMS (bottom).

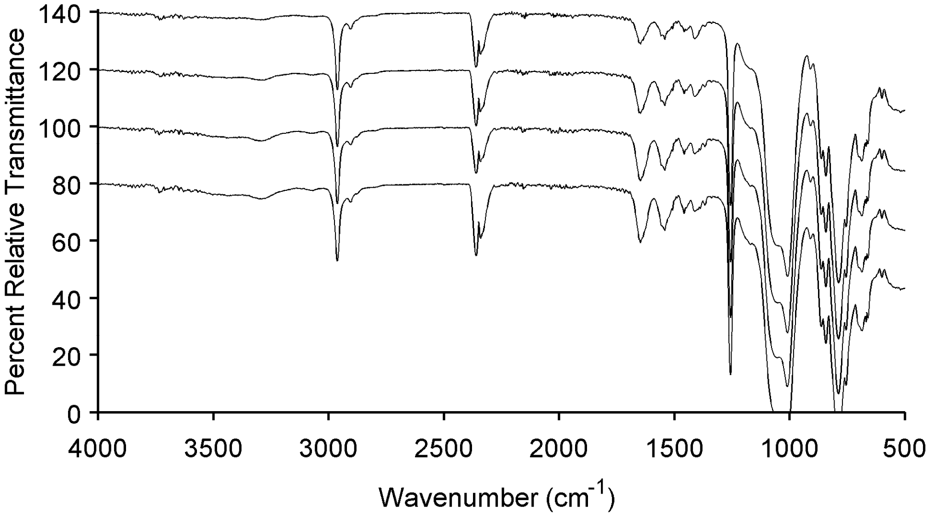

Figure 22: FT-IR Transmission spectra for NIPAAm grafted PDMS substrates. The four spectral curves (from top to bottom) correspond to grafting conditions: BP1-UV3, BP3-UV3, BP5-UV3, BP7-UV3.

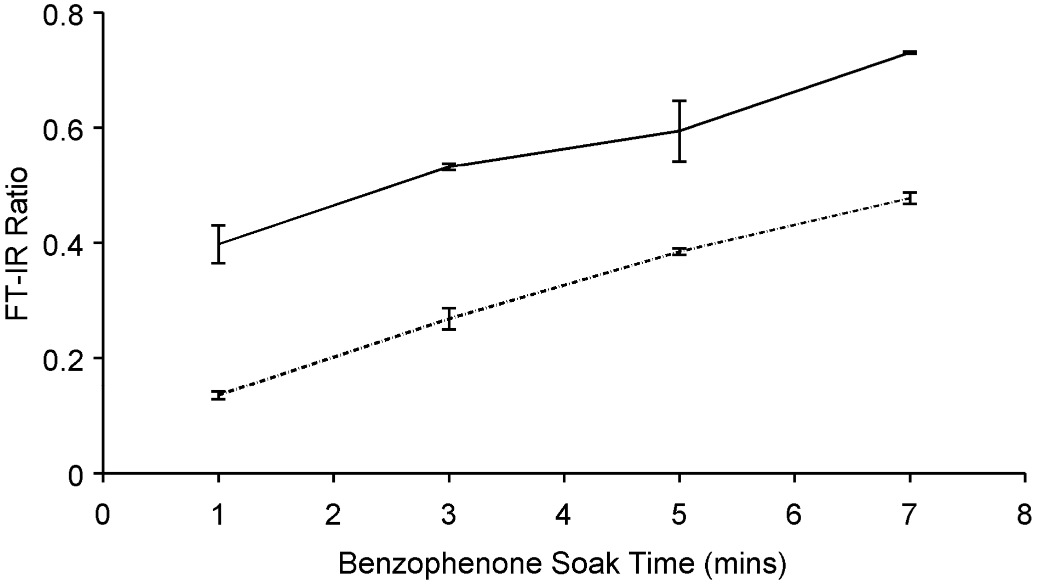

Figure 23: Mean Ratio of FT-IR peak absorbance of the 1650 cm^{-1} NIPAAm amide peak to the 2900 cm^{-1} PDMS methyl peak for substrates soaked in 20% (w/v) benzophenone for 1,2,5,7 minutes and exposed to UV for 2 minute (dashed) or 3 minutes (solid). Error bars represented the standard error (N=5) per sample.

Because we can control the density of NIPAAm graft density, we tested how the graft density of NIPAAm impacted bovine vascular smooth muscle cell attachment. To accomplish this, vascular smooth muscle cells were seeded onto substrates grafted with different benzophenone soak times and seeded with bovine vascular smooth muscle cells. Figure 25 shows bVSMCs 24 hours after being seeded onto four different substrate conditions. When these cells are seeded onto blank PDMS, minimal cell adhesion occurs. At lower graft densities, bVSMCs adhere well until reaching the optimal ratio of 0.4–0.5, which corresponds to a NIPAAm surface density of approximately 15 μg/cm^2. At surface densities greater than 20 μg/cm^2, the surface density becomes unsuitable for cell attachment. Substrates with a grafting density in the range of 10–20 μg /cm^2 are optimal for cell attachment, yielding a non-destructive method to evaluate substrate quality. This result differs from previously published work within our lab where no relationship between FT-IR data and cell attachment was determined[129]. Yet, the dependence of cell attachment on NIPAAm surface graft density has been reported by others groups[71,80,81,83]. Okano *et al.* showed that when NIPAAm was grafted to the surface of polystyrene dishes at densities of 1.4 μg /cm^2 cells could adhere, but when the density was increased to 2.9 μg /cm^2 cells could not attach. Interestingly, when grafting NIPAAm onto PDMS surfaces, the amount of NIPAAm graft densities that correspond to cell is an order of magnitude higher than for polystyrene dishes. However, when grafting NIPAAm onto PDMS using electron beam irradiation to initiate the reaction, higher surface densities of NIPAAm (11.9 μg /cm^2) corresponded to optimal cell attachment, which is similar to the results reported here[80]. Interestingly, this study did not show successful cell sheet formation[80].

The grafting scheme is a UV initiated free-radical polymerization, which makes the process sensitive to environmental factors. Furthermore, the process is sensitive to heterogeneities that arise during grafting caused by variability in benzophenone surface concentration, UV exposure, and oxygen content during polymerization inherent to bench-top research. Each of these factors can lead to both spatial variability and batch-to-batch variability, making it essential to establish a non-destructive method to evaluate substrate quality.

We found that optimizing the grafting process for bVSMC attachment did not guarantee long-term culture of vascular smooth muscle cell sheets. While possible to grow cells sheets on the NIPAAm surface, frequently the bVSMC cell sheets would not form confluent cell sheets or detach prematurely. To improve the quality of cell sheets, we embarked upon further surface modification of the NIPAAm surface.

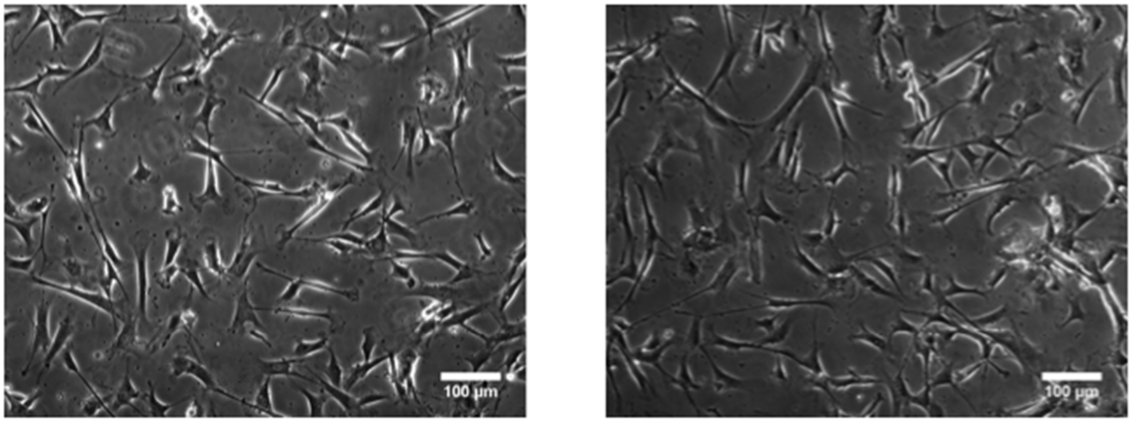

BP 1 – UV 3 **BP 3 – UV 3**

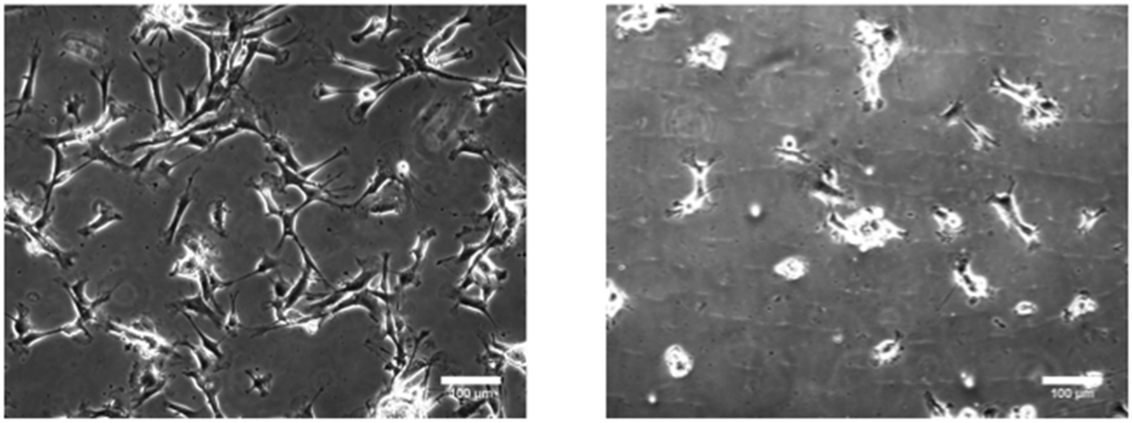

BP 5 – UV 3 **BP 7 – UV 3**

Figure 24: Cell seeding results onto NIPAAm-PDMS substrates soaked for 1,3,5,7 minutes in 20% [w/v] benzophenone in acetone and exposed to 3 minutes of UV irradiation (65 mW/cm^2) and seeded with bVSMCs at 15,000 cells/cm^2). Images taken 24 hours post seeding and scale bar corresponds to 100 μm.

Previous reports have demonstrated that 3-aminopropyltriethoxysilane (APTES) can improve cell attachment by adding extra primary amine groups to the surfaces thus facilitating cell attachment[73,130]. Using APTES as a synthetic cell adhesion promoter, we incorporated APTES into the NIPAAm-PDMS substrates surface by baking the substrates in a solution of 10% APTES in ethanol. Figure 26 shows bVSMCs attachment when seeded onto both NIPAAm-PDMS and APTES substrate with an initial seeding density of 15,000 cells/cm^2. Cells seeded onto the APTES modified surface show improved attachment compared to NIPAAm only substrates. More importantly, the incorporation of APTES into the NIPAAm-PDMS reduces the frequency of cell sheets detaching or ripping apart. FT-IR data collected on NIPAAm substrates before and after modification with APTES showed spectra changes in the FT-IR spectra. Figure 25 plots representative FT-IR spectra of the same substrates collected before and after APTES modification. Interestingly, the FT-IR spectra show a decrease in the peaks corresponding to the amide bonds of the NIPAAm (1650 cm^{-1}), while also exhibiting increased peak absorbance in the broadband wavenumbers (3000–3500 cm^{-1}).

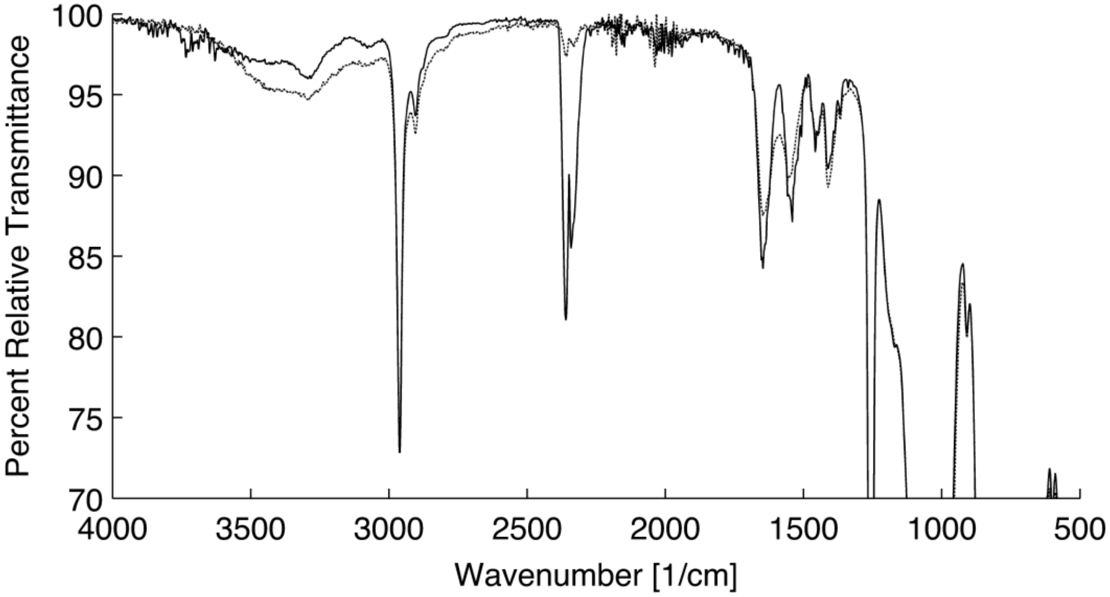

Figure 25: FT-IR Spectra for NIPAAm-PDMS substrates before (black) and after (gray) surface modification with APTES.

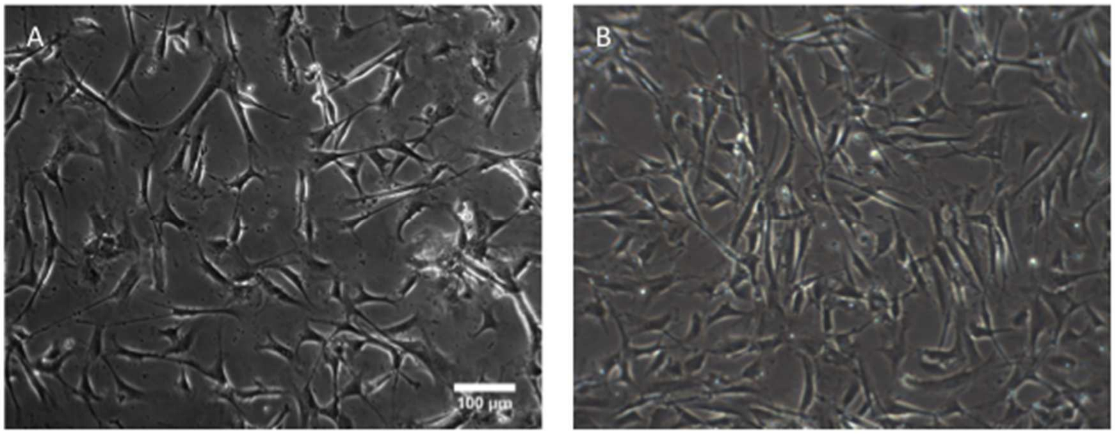

Figure 26: Representative image of vascular smooth muscle cell attachment and spreading (15,000 cell/cm^2 seeding density) 24 hours after seeding on A) NIPAAm-PDMS substrates and B) APTES-NIPAAm-PDMS substrates.

Water contact angle measurements were conducted on both APTES-modified and unmodified substrates to determine whether APTES modified NIPAAm-PDMS surface were still thermo-responsive. Figure 27 shows sessile water contact angle measurements for BP3-UV3 substrates – the optimal grafting conditions – as a function of temperature. Above 37˚C, the water contact angle is about 105˚ and as the temperature drops, the water contact angle drops until it reaches approximately 85˚. Water contact angle measurements for the optimal grafting conditions (BP3-UV3) are higher than results published by Rayatpisheh *et al.* for a similar, but different method of grafting NIPAAm to PDMS. This study reported water contact angle measurements that varied from 57˚to 73º at 20˚C and 37˚C, respectively[79]. However, in the same study the water contact angle of blank PDMS was measured to be 97˚, which is significantly lower than the known water contact angle for PDMS of 110˚ [75,79]. This suggests that these measurements are underestimating the actual water contact angle.

Figure 28a plots water contact angle for NIPAAm grafted PDMS as a function of benzophenone soak time for substrates exposed to 3 minutes UV irradiation at both 42°C and 22°C. All four different conditions show statistically significant difference in water contact angle between 42°C and 22°C ($p<0.05$). Figure 28b plots water contact angle measurements for APTES coated NIPAAm-PDMS substrates grafted under the same conditions as panel-a. APTES incorporation only impacts substrates with the lowest grafting densities of NIPAAm (BP1-UV3), causing the substrate to have no statistically significant change in water contact angle when the temperature changes from 42°C to 22°C ($p=0.067$). However, the incorporation of APTES into NIPAAm-PDMS surfaces with higher grafting densities (BP3-UV3 to BP7-UV3) does not inhibit the substrates from undergoing statistically significant differences in water contact angle between 42˚C and 22˚C. Figure 28 shows a sudden drop in water contact angle at a benzophenone soaking time of 5 minutes. This particular substrate had high levels of spatial variability in surface density of NIPAAm when analyzed with FT-IR, which could have contributed to the drop in water contact angle at 42˚C. More importantly, these data highlights the potential negative implications of surface variability towards achieving a robust substrate platform as well as the importance of correlating cell attachment to NIPAAm surface density.

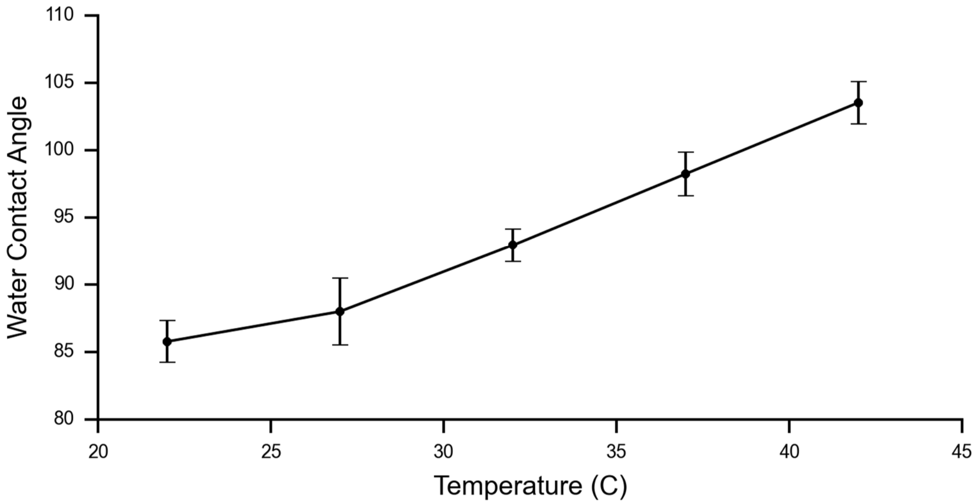

Figure 27: Mean water contact angle for NIPAAm-PDMS substrate grafted with BP3-UV3 conditions as a function of temperature (N=9, ± SEM).

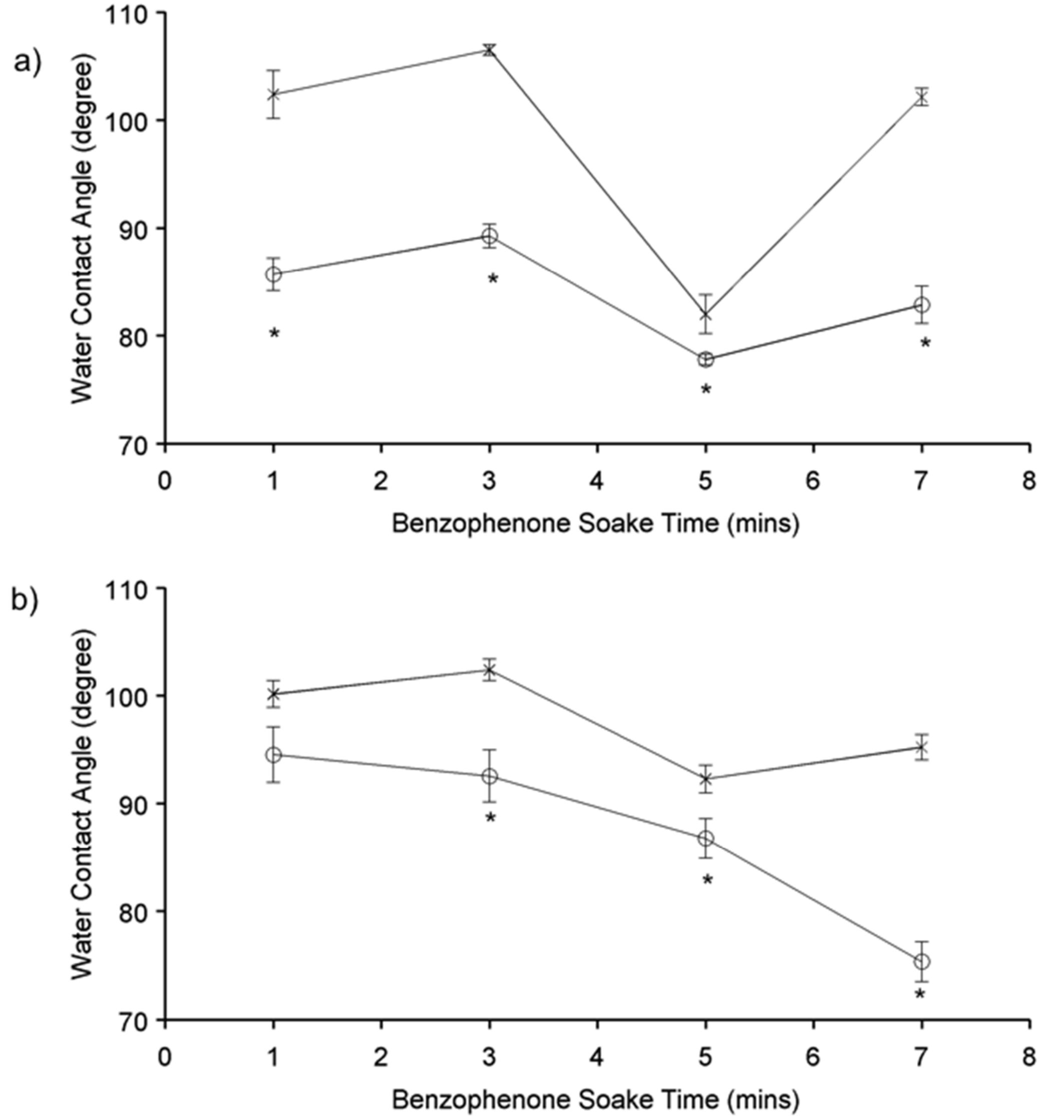

Figure 28: Water contact angle as a function of benzophenone soak time when exposed to 3 minute UV for a) NIPAAm-PDMS and b) APTES-NIPAAm-PDMS at 42˚C (x) and 22˚C (circle). Asterisks correspond to statistically different water contact angle between 42˚C and 22˚C for each benzophenone soak time (t-Test; $p<0.05$).

The experimental characterization of the APTES-coated surfaces suggests that APTES is forming a network within the polymerized NIPAAm chains. Water contact angle measurements between NIPAAM substrates before and after APTES treatment shows that the APTES substrates remain thermo-responsive, but the difference in water contact angle between 22˚C and 42˚C decreases slightly. As can be seen in Figure 28, the APTES network only impacts substrates with lower grafting densities of NIPAAm, whereas at higher surface densities incorporating APTES has no impact upon the change in water contact angle of the surface. This data suggests that APTES is not incorporating into the surface of these substrates because of the higher surface density of NIPAAm on the surface. FT-IR data collected before and after APTES surface modification shows significant differences; but interestingly shows decreased absorbance in 1650 cm^{-1} amide peaks of the NIPAAm. The FT-IR data suggests that incorporation of APTES causes formation of hydrogen bonds between the NIPAAm and APTES structures[131]. This is consistent with results from Newby *et al*. where they created a spin-coated, thermo-responsive glass based APTES-pNIPAAm cell culture platform and reported hydrogen bonding between pNIPAAm chains and the APTES structure of the surface of the PDMS[131].

Vascular Smooth Muscle Cell Sheets Structure

Bovine vascular smooth muscle cell sheets were grown on both patterned and non-patterned APTES substrates. Figure 29 shows images of a pair of cell sheets after 2 weeks in culture and 7 days of ascorbic acid treatment that had not been detached from the substrate. Phase-contrast images of the cell sheet show no cellular alignment while cells grown on micropatterned substrates for aligned cell sheets show directional alignment. While directional alignment is difficult to see in the phase-contrast microscopy image, the F-actin structure shows clear directional alignment on the micropatterned substrates, whereas cells grown on non-patterned substrates show no directional dependence. Cell alignment was quantified using a 2D Fourier Transform-based quantification method, and the structural differences become clear. The non-patterned cell sheet F-actin structure shows no preferential direction, as the distribution is flat. On the other hand, the aligned cell sheet shows preferential alignment in the direction of the micropattern.

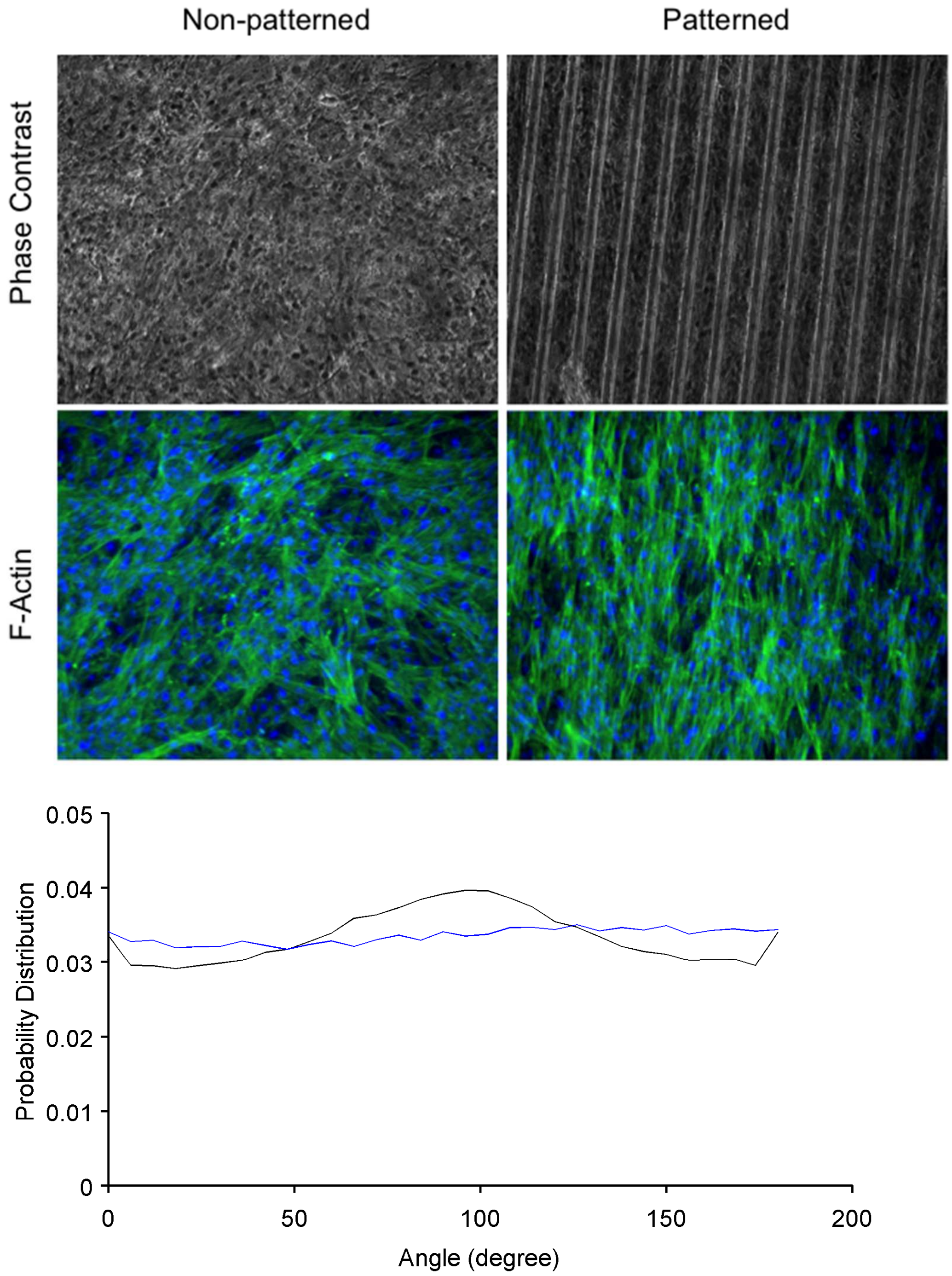

Figure 29: Phase contrast images and the F-actin structure of vascular smooth muscle cell sheets grown on non-patterned and patterned substrates for 13 days with 7 days ascorbic acid treatment. The figure shows F-actin orientation for aligned (black) and non-aligned (blue) cell sheets using the 2D FFT method for the cell sheet images.

Chapter 4: Mechanical behavior of aligned vascular smooth muscle cell sheets for arterial tissue engineering

Introduction

This chapter combines the work on force sensor development in Chapter 2 and the cell sheet development from Chapter 3 to form the nexus of this dissertation. As stated before, any functional engineered tissue must have the necessary mechanical properties to function properly[37]. For arterial tissue, engineering mechanics are especially important because large hemodynamic forces can cause graft failure and cellular dysfunction[122]. As described earlier, the complex cellular and extracellular structure of the medial layer of an artery determines the nonlinear mechanical properties of arterial tissue[29]. A tissue engineered construct that replicates the native tissue structure has the potential to overcome problems such as anastomotic intimal hyperplasia and graft thrombosis that plague current strategies[123].

Previous work has applied biomechanics to arterial tissue engineering. Gavin *et al*. showed that dynamic stimulation of arterial tissue grown using self-assembly induces structural anisotropy and stiffening due to increased structural alignment[132]. This study only demonstrated increased stiffness caused by alignment over non-aligned tissues and did not show difference in the mechanics between the aligned and transverse direction.

A tissue engineering approach based upon cell sheets is an attractive strategy because it has been shown that single layer, aligned vascular smooth muscle cell sheets can be cultured successfully[116]. Previously, we had shown that vascular smooth muscle cell sheets grown for 6 weeks on patterned PDMS substrates were structurally and mechanically anisotropic[93]. However, the cell sheets only showed a 50% strength and modulus increase in the direction of alignment compared to the transverse direction. This study also showed that these sheets were multiple cell-layers thick, but cell alignment diminished as the cell sheet thickened. Therefore, we hypothesized that culturing cell sheets for a shorter time duration would have several distinct advantageous over previous methods. Shorter time durations would lead to single layer cell sheets with more uniform cell alignment and this higher structural organization would in turn lead to greater mechanical anisotropy.

To test this hypothesis, the research reported in this chapter uses the force sensor design described in Chapter 2 along with the substrate platform presented in Chapter 3. We show that cells grown on flat and patterned substrates do not alter the amount of extracellular matrix secretion by the smooth muscle cells, but does cause cellular alignment and collagen alignment in the cell sheets. We then characterized the mechanics of the aligned cell sheets to show that cell sheets are significantly stiffer (800%) in the alignment direction, but fail at lower engineering strains (80%) in the alignment direction compared to the transverse direction. Using a generalized version of a phenomenological model developed by Lanir, we then modeled the stress-strain behavior of the cell sheet based tissues to better extract the incremental tensile modulus[109].

Methods

Cell Sheet Culture

Cell sheets were cultured for subsequent mechanical testing. These sheets were grown using the methods described in detail within Chapter 3 of this thesis. In brief, bovine vascular smooth muscle cells were seeded onto flat and patterned thermo-responsive PDMS substrates with a seeding density of 45,000 cells/cm^2 and 60,000 cells/cm^2, respectively. Seeding density was varied based upon substrate to ensure that flat and patterned cell sheets reached confluence concurrently. Cells were allowed to grow to confluence and then treated with 50 μ/mL of ascorbic acid daily. Ascorbic acid treatment continued until cell sheets were harvested. After detachment, the length and width of the cell sheet were measured and normalized by dividing by the length and width of the substrate to measure the linear contraction of the cell sheet.

Cell Sheet Decellularization

Bovine vascular smooth muscle cell sheets were decellularized by incubating the cell sheets with a solution of 0.1% Triton-X 100 and 200 mM sodium hydroxide for 30 minutes at room temperature.

Picrosirius Collagen Staining

Cell sheets were rinsed twice with warm PBS and then incubated at room temperature with 4% paraformaldehyde for 10 minutes. After this, cell sheets were rinsed two times in deionized water for 2–3 minutes and then incubated in 0.1% picrosirius red (Electron Microscopy Sciences, Hatfield, PA), at room temperature for 90 minutes. Cell sheets were then rinsed in 0.5% acetic acid for 2 minutes twice and then rinsed briefly in deionized water. Cell sheets were soaked in 70% ethanol for 30 seconds and the dipped in 95% ethanol and 100% ethanol to dehydrate the sample. Cell sheets were then immersed briefly in xylene and allowed to dry overnight. Stained cell sheet samples were then imaged on an Axiovert S100 (Karl Zeiss, Germany).

Collagen and Elastin Quantification

Soluble and pepsin-soluble collagen content was measured using the commercially available Sircol Collagen Assay (Biocolor, UK) kit. Samples were incubated at 4 C in 0.1 mg/mL of porcine pepsin (Sigma) in 0.5 M acetic acid for 24 hours. Tissue samples were then incubated for 30 minutes in 1 mL of Sircol Dye reagent at room temperature, centrifuged at 12,000 RPM for 10 minutes and then incubated in a Acid-Salt wash to release unbound dye reagent. Samples were then incubated in a solution of sodium hydroxide and surfactants to release the dye bound to the collagen. After a five-minute incubation at room temperature, absorbance measurements were conducted using a plate reader.

Fastin Elastin Assay

The elastin content of the smooth muscle cell sheets was measured using the Fastin kit (Biocolor, UK). Cell sheets were detached and cut into strips and the wet mass was recorded. Elastin was then solubilized by heating the samples for 60 minutes at 100^{o}C in 0.25 M oxalic acid. Samples were centrifuged for 10 minutes at 12,000 RPM and the supernatant was aspirated. The remaining tissue extract was suspended in 750 μL of the

Fastin Elastin Precipitating reagent for 10 minutes at room temperature. Samples were then centrifuged at 12,000 RPM for 10 minutes and then excess solution was aspirated. The samples were then incubated at room temperature under gentle mechanical agitation for 90 minutes in 1 mL of the Elastin Dye Reagent and then again centrifuged for 10 minutes at 12,000 RPM. Excess solution was removed from each sample and then the Fastin dye dissociation reagent was added to release the bound Elastin Dye. Finally, 200 μL of each sample was transferred to a 96 well plate and absorbance measurements were conducted at 513 nm.

Mechanical Testing

Cell sheets were detached from the substrates by incubating the cell sheets at room temperature PBS until the cell sheet detached, which took approximately 10-20 minutes. After detachment, the sheet dimensions were measured with a micrometer. Figure 30 shows how multiple cell sheet strips were cut from individual cell sheets in both the direction of alignment and the transverse direction (i.e., perpendicular to alignment). For non-patterned cell sheets, the direction of alignment was chosen arbitrarily. Cell sheets strips were approximately 8 mm long and 3 mm wide, and these dimensions were measured and recorded for each cell sheet. Following attachment to the grips of the tensile testing device shown in Figure 4, cell sheet strips were stretched until they began to bear load. The sample length and width at that point were then measured to enable post-test calculation of engineering stress and strain. Cell sheet strips were stretched 3 cycles to 20% pre-strain cycles before mechanically loading the tissue sheets to ultimate failure. All cell sheet mechanical tests were conducted with a strain rate of 0.01/ second.

Mechanical Analysis

Force-extension curves collected from the uniaxial tensile test were analyzed using a custom MATLAB program. First, the force data was down sampled to 5 samples/second by calculating the mean force over each 0.2 second time increment. Engineering stress-strain curves were calculated using standard methods and the measured values of force, cross-sectional area, and specimen elongation recorded during the test. The tangent modulus was measured in MATLAB by manually choosing the linear region of the stress-strain curve as shown in Figure 30. The linear region of the stress-strain curve was fit using linear regression, and the slope of the fit is the tangent modulus for the specimen.

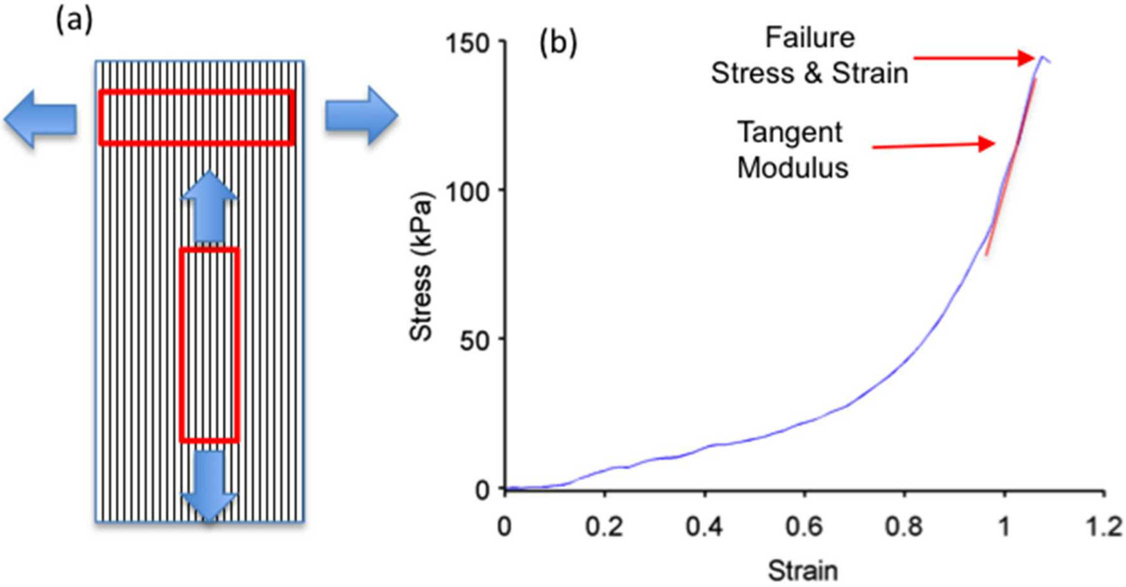

Figure 30: Cell Sheet Mechanical Testing Procedure (a) cell sheet strips are cut in the parallel and transverse to alignment for mechanical testing (b) A representative stress-strain curve for a cell sheet with the tangent modulus and the definition of failure stress and failure strain labeled.

Cell Sheet Mechanical Modeling

The mechanical behavior of cell sheets were modeled using a hyper-elastic strain energy based function developed by Lanir[109]. The strain energy function can be expressed by the following equations.

$$\psi = c_1\left\{\exp\left(c_2(\mathrm{I}_4^{1/2}-1)\right)-1\right\} \tag{8}$$

$$\mathrm{I}_4 = M^T C M \tag{9}$$

$$M = \begin{pmatrix} \sin(\alpha) \\ \cos(\alpha) \\ 0 \end{pmatrix} \tag{10}$$

, where c_1, c_2 are fitting parameters, I_4 is the fourth order tensor invariant and *M* is the unit direction representing the fiber alignment direction. The fiber alignment is represented by the angle α, corresponding to an angle between the modeled fiber alignment direction and the aligned direction of the cell sheet. Because the experimental data is uniaxial and the material is assumed to be incompressible (*det(F)=1*), *F* simplifies to the following form:

$$F = \begin{pmatrix} \lambda_1 & 0 & 0 \\ 0 & \lambda_1^{-1/2} & 0 \\ 0 & 0 & \lambda_1^{-1/2} \end{pmatrix} \tag{11}$$

Where $\lambda_1$is the stretch due to uniaxial extension and can be defined as $\lambda = \epsilon + 1$ where ε is the engineering strain. Using the strain energy function above with all of the other assumptions and results, the Cauchy stress tensor can be determined using the following equation[133].

$$t = -pI + F\frac{\partial \Psi}{\partial C}F^{T} \tag{12}$$

, where t is the Cauchy stress tensor, F is the deformation gradient and C is the Right Cauchy-Green tensor $(F^{T}F)$. The Cauchy Stress tensor represents the stress in the deformed configuration with respect to the strain state in the deformed configuration. However, the experimental data collected relates the stress of the cell sheet in the deformed configuration with respect to the initial configuration, known as the 1st Piola-Kirchoff (PK) Stress. The Cauchy stress tensor can be converted to the PK Stress using the following transformation:

$$P = J\, t\, F^{-T} \tag{13}$$

Where P is the 1st PK Stress, J is the det(F) (which is assumed to be 1) and F is the deformation gradient. Using the above equations, the strain energy can be represented by the following equation.

$$P = -p\, F^{-T} + \{c_1 \exp[c_2(I_4 - 2I_4^{1/2} + 1)](c_2(1 - I_4^{-1/2})\} F\, M \otimes M\, FF^{-T} \tag{14}$$

In this equation, P is the 1st PK stress, p is a hydrostatic pressure, M is the fiber alignment direction, F is the deformation gradient tensor, I_4 is the fourth order tensor invariant defined by $M'CM$ where C is the left Cauchy-Green tensor. Note that the quantity within the brackets and the hydrostatic pressure term, p, are all scalar quantities and every other quantity is a second order tensor. The model simplifies considerably considering that it is being fit to uniaxial tensile data. Because the direction transverse is not loaded it can be assumed that the stress in that direction is zero, allowing the unique determination of the hydrostatic term, p. Once the hydrostatic term is known, the stress state can be uniquely determined for given c_1, c_2, α values.

This model was applied to the experimental data by using the Levenberg-Marquardt Algorithm (MATLAB, Mathworks, Inc.). The model was used to fit mechanical data from cell sheets in both directions (aligned and transverse) simultaneously, yielding one set of fitting parameters to describe the mechanical response in both directions. For non-patterned cell sheets, aligned and transverse directions were chosen randomly. The parameters in Table 4 were used to seed the optimization routine. When the model clearly converged to a sub-optimal solution, different seeding parameters were used until the algorithm converged to an appropriate fit.

	$\boldsymbol{\alpha}$	$\boldsymbol{c_1}$	$\boldsymbol{c_2}$
Seed	20	1000	10
Lower Bound	0	10,000	1
Upper Bound	90	100,000	200

Table 4: Model Optimization Parameters: The Levenberg-Marquardt algorithm parameter optimization space was seeded with initial conditions and bounded by upper and lower limits.

Results

Cell Sheet Extracellular Matrix Content

As the vascular smooth muscle cell sheets are grown in culture, the cells produce extracellular matrix. Because the collagen and elastin (along with proteoglycans) structure within the artery dominate the passive mechanical properties of native arterial tissue, we measured the collagen content within the smooth muscle derived cell sheets. As can be observed in Figure 31 there was no difference in the collagen content in the aligned and non-aligned cell sheets. After this culture duration, there is significantly less collagen per mass compared to a native rabbit aorta control, which has been measured to have 30 μg/mg when measured using the same method. This data suggest that any differences in mechanical properties of patterned and non-patterned cell sheets should be due structural differences in the cell sheets and not compositional differences between patterned and non-patterned cell sheets since both sets of cell sheets have similar levels of collagen.

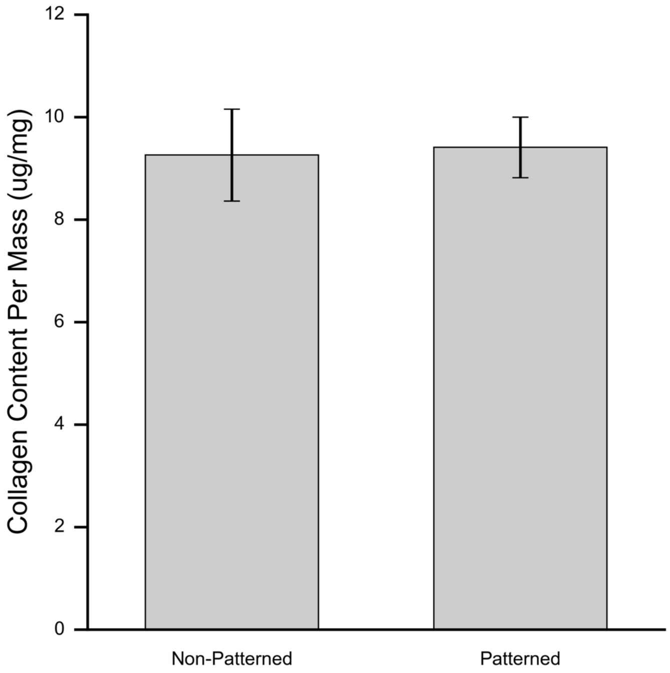

Figure 31: Soluble and pepsin soluble collagen content in cell sheets for both non-patterned and patterned bovine vascular smooth muscle cell sheets after 12 days in culture and 5 days of ascorbic acid treatment (50 µg/mL). Plots shows mean collagen mass per wet cell sheet mass ± SEM (µg /mg) with N=3 with duplicated measurements. There is no difference between patterned and non-patterned cell sheet ($p = 0.87$) when analyzed using Student's t-Test.

Vascular smooth muscle cell sheet structure

Vascular smooth muscle cells that form a confluent cell sheet on a patterned substrate retain their alignment, whereas cells grown on non-patterned substrates show no preferential direction of alignment. Figure 29 shows phase contrast images and fluorescent images of the F-actin structure for both patterned and non-patterned cell sheets while still attached to the substrates after being fixed with paraformaldehyde. The underlying micropattern can clearly be seen on the patterned phase-contrast image and there is clear cell alignment in the direction of the micropattern as compared to the non-patterned cell sheet. Figure 29 also shows clear differences in the F-actin structure of the cell sheets grown on non-patterned and patterned substrates. Because the phase-contrast images and F-actin images were taken with the same orientation, it is clear that the cells align in the direction of the micropattern. Figure 32 shows non-patterned and patterned phase contrast images of the cell sheet collagen structure when stained with picrosirius red dye. Collagen shows preferential alignment in the aligned cell sheet while the non-patterned cell sheets is randomly aligned. Analysis of the collagen structure with the 2D Fourier Transform-based method shows a modest alignment in the patterned cell sheet. The patterned cell sheet shows preferential alignment at 142° and the non-patterned cell sheet shows no preferential alignment.

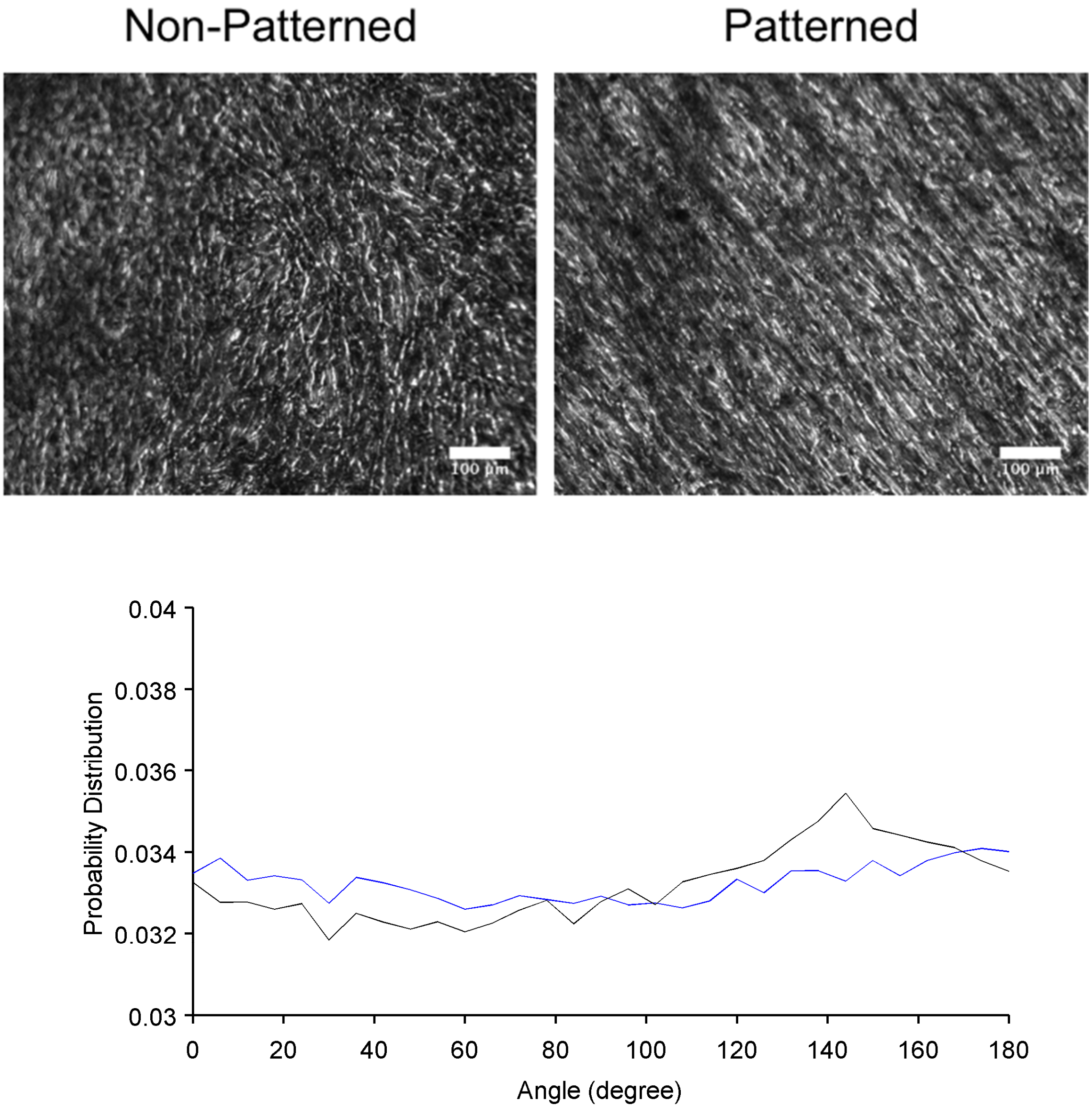

Figure 32: Top) Bovine vascular smooth muscle cell sheets stained with picrosirius red stain. Bottom) Collagen Alignment quantified using the 2D FFT algorithm.

Cell Sheet Contraction

When vascular smooth muscle cell sheets grown on thermo-responsive PDMS substrates detach from the substrates, the cell sheet shrinks two-dimensionally while maintaining the shape of the original substrate. Figure 33 shows a detached cell sheet from non-patterned substrates next to the substrate from which it was detached. Clearly, the cell shape has contracted upon release while maintaining the shape of the original substrates. The non-patterned cell sheet contracts uniformly in both directions, whereas the aligned cell sheet contracts more in the direction of alignment than in the transverse direction. This trend is also observed for vascular smooth muscle cell sheets that have been cultured for different time durations; the associated data is shown in Figure 34. The contraction ratio represents the linear contraction upon release (i.e., the width of the cell sheet upon release normalized by the width of the cell sheet before release). For the non-patterned cell sheets, cell sheet contraction is isotropic in both directions whereas the patterned cell sheet contracts more in the direction of alignment compared to the transverse direction.

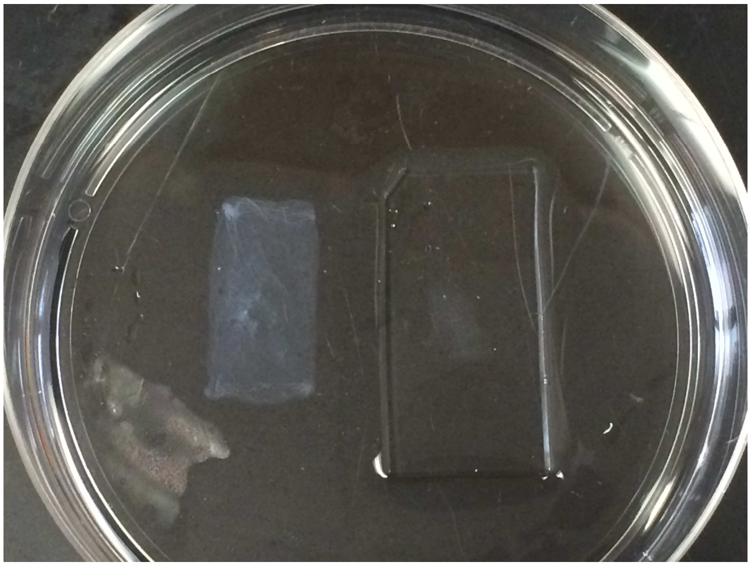

Figure 33: Cell sheet contraction for non-patterned cell sheets cultured with bovine vascular smooth muscle cells for 21 days in culture with 14 days ascorbic acid treatment. For scale, the PDMS substrate measures 2x4 cm.

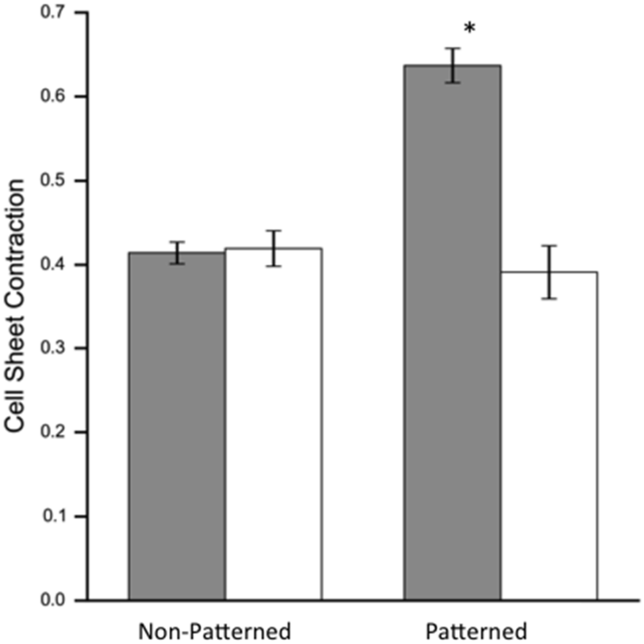

Figure 34: Linear cell sheet contraction in the direction of alignment (white) and the direction perpendicular to alignment (gray) for bovine vascular smooth muscle cell sheets. Cell sheets grown on non-patterned substrates show no directional dependence in cell sheet contraction (t-Test: p=0.82) while cell sheets grown on patterned substrates contact a greater amount in the aligned direction compared to the non-aligned direction (t-Test: p=0.001)

Cell Sheet Mechanics

Aligned Mechanics

Uniaxial tensile tests were performed on non-patterned and patterned cell sheets to determine whether the structural alignment induced mechanical alignment. The details from this set of experiments are included in Table 5. Both the tangent modulus and the failure engineering stress are larger in the alignment direction than transverse direction. Interestingly, the aligned cell sheets (in both directions) failed at lower levels of strain compared to the non-patterned cell sheets, which typically failed around 75% strain.

Because of the significant variability between samples, the amount of anisotropy of individual cell sheets was determined by calculating the ratio of the tangent modulus, failure stress and failure strain in the alignment compared to the transverse direction for individual cell sheets. A comparison between the mechanical properties of non-patterned and patterned cell sheets is shown in Figure 36. As expected, the non-patterned cell sheets have no directional dependence. The mean failure stress, failure strain, and tangent modulus ratios are all approximately 1. On the other hand, patterned cell sheets are approximately 8x stiffer and have a failure stress that is nearly 4.5x times larger in parallel direction compared to the transverse direction. Interestingly, when these data were normalized using this method, the patterned cell sheets failed at lower strains in the direction of alignment than in the transverse direction.

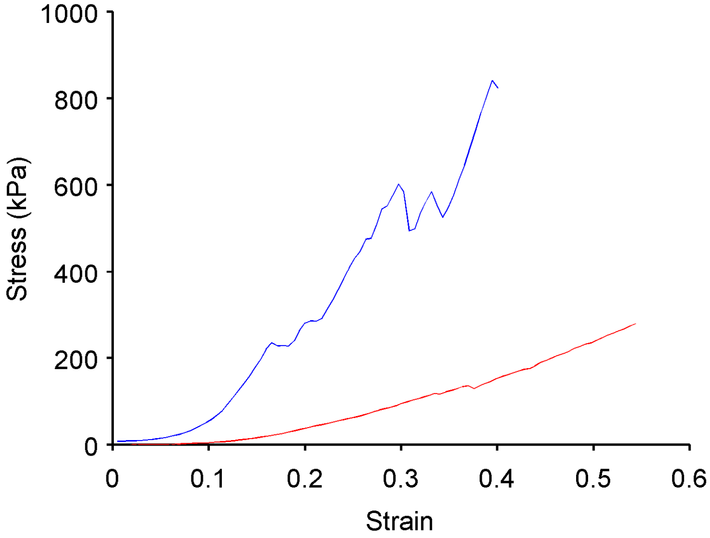

Figure 35: Stress-strain curve for cell sheet in the aligned (blue) and transverse directions. Cell sheet was cultured or 21 days in culture and subject to 14 days ascorbic acid treatment.

Direction	**Tangent Modulus (kPa)**	**Failure Stress (kPa)**	**Failure Engineering Strain**
Parallel	2980±1177	410 ±140	0.43 ± 0.1
Perpendicular	474 ± 107	155 ± 40	0.50 ± 0.06
Non-Patterned	1009 ± 147	225 ± 28.5	0.75 ± 0.05

Table 5: Mechanical Properties of non-patterned and patterned vascular smooth muscle cell sheets (N=8)

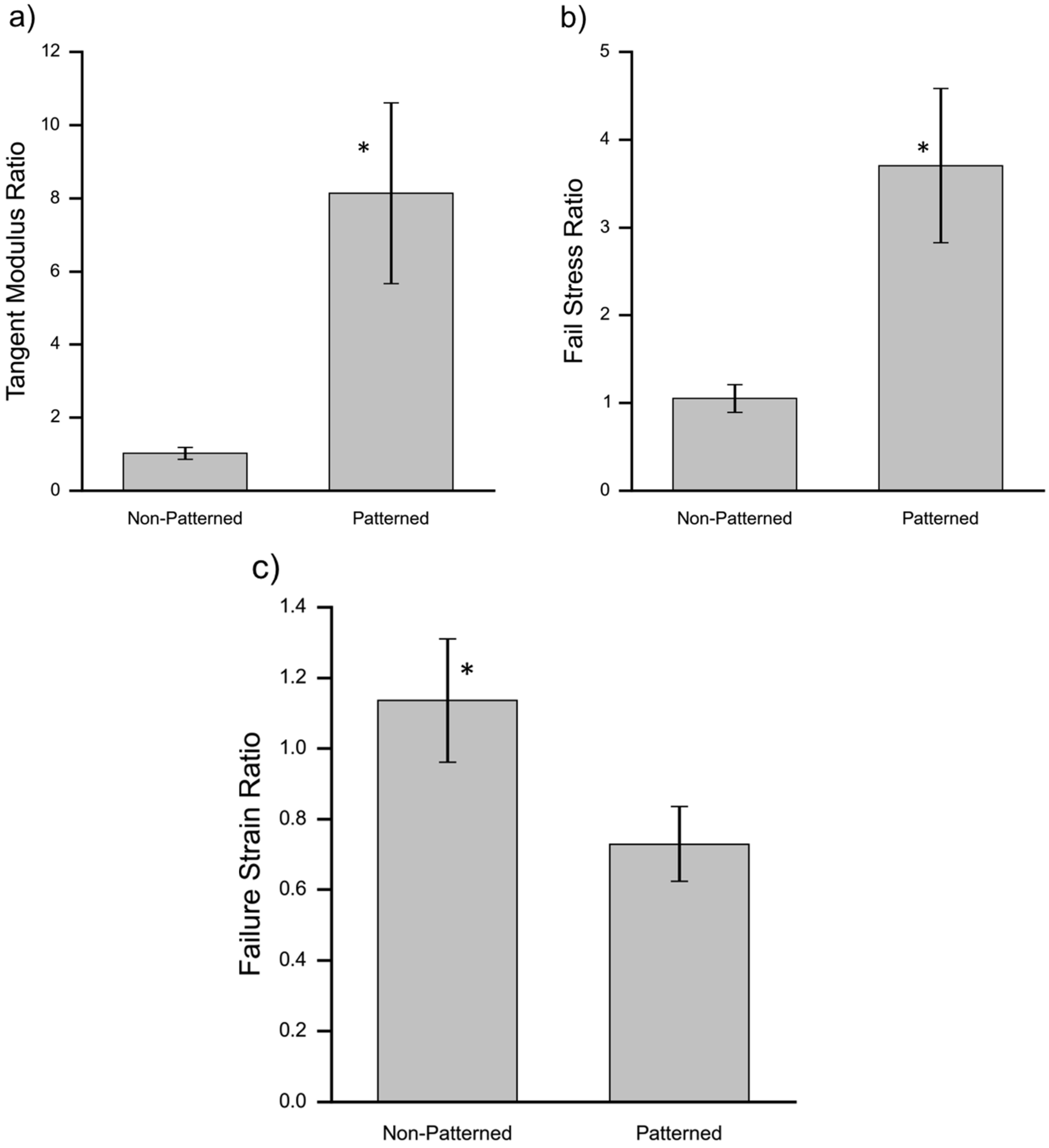

Figure 36: Mean ratio of the a) tangent modulus, b) engineering failure stress and c) engineering failure strain in the direction of alignment compared to the direction transverse to alignment. Asterisks imply statistical significance (t-Test; $p<0.05$) Tangent modulus ratio and failure stress ratio were both significantly larger ($p=0.034$) and ($p=0.029$), respectively for cell sheets grown on patterned substrates ($N=8$) compared to non-patterned cell sheets ($N=8$). The failure strain of non-patterned cell sheets was larger than the failure strain of patterned cell sheets ($p=0.03$)

Decellularized Cell Sheet Mechanics

To determine the relative contribution of the different load bearing constituents of the cell sheets, uniaxial tensile tests were performed on cell sheets before and after cell sheet decellularization. For this experiment, cell sheets were cultured on patterned substrates and cultured for 12 days and treated with ascorbic acid for only 5 days. Cell sheets were subsequently detached from the substrate and then mechanically characterized before and after decellularization in both the aligned and transverse direction. The parallel cell sheet strip was stretched to 20% engineering strain repeatedly until the stress-strain curve didn't change. Because the strip in the perpendicular direction was much more extensible than the parallel strip, it was stretched to 30% engineering strain.

After decellularization, both cell sheet strips begin bearing load at approximately the same strain as before decellularization. The tangent modulus for each of the samples before and after decellularization is summarized in Table 6. The tangent modulus for the parallel sample decreased 14.4% while the perpendicular sample decreased 39.5%. The maximum engineering stress at the samples respective maximum strains (20% and 30% for the aligned and transverse sample, respectively) decreased 17.4% and 38.5%.

	Normal	**Decellularized**	**% Decrease**	**Difference**
Tangent Modulus (kPa)				
Parallel	2436	2086	14.4	350
Perpendicular	389	234	39.8	155
Maximum Stress (kPa)				
Parallel	113.7	93.9	17.4	20
Perpendicular	27.8	17.1	38.5	11

Table 6: Mechanical properties of aligned cell sheets before and after decellularization. Data in the normal and decellularized columns correspond to measurements taken before and after decellularization. % Decrease is a measure of the % decrease after decellularization and the difference is calculated as the parameter difference before and after decellularization.

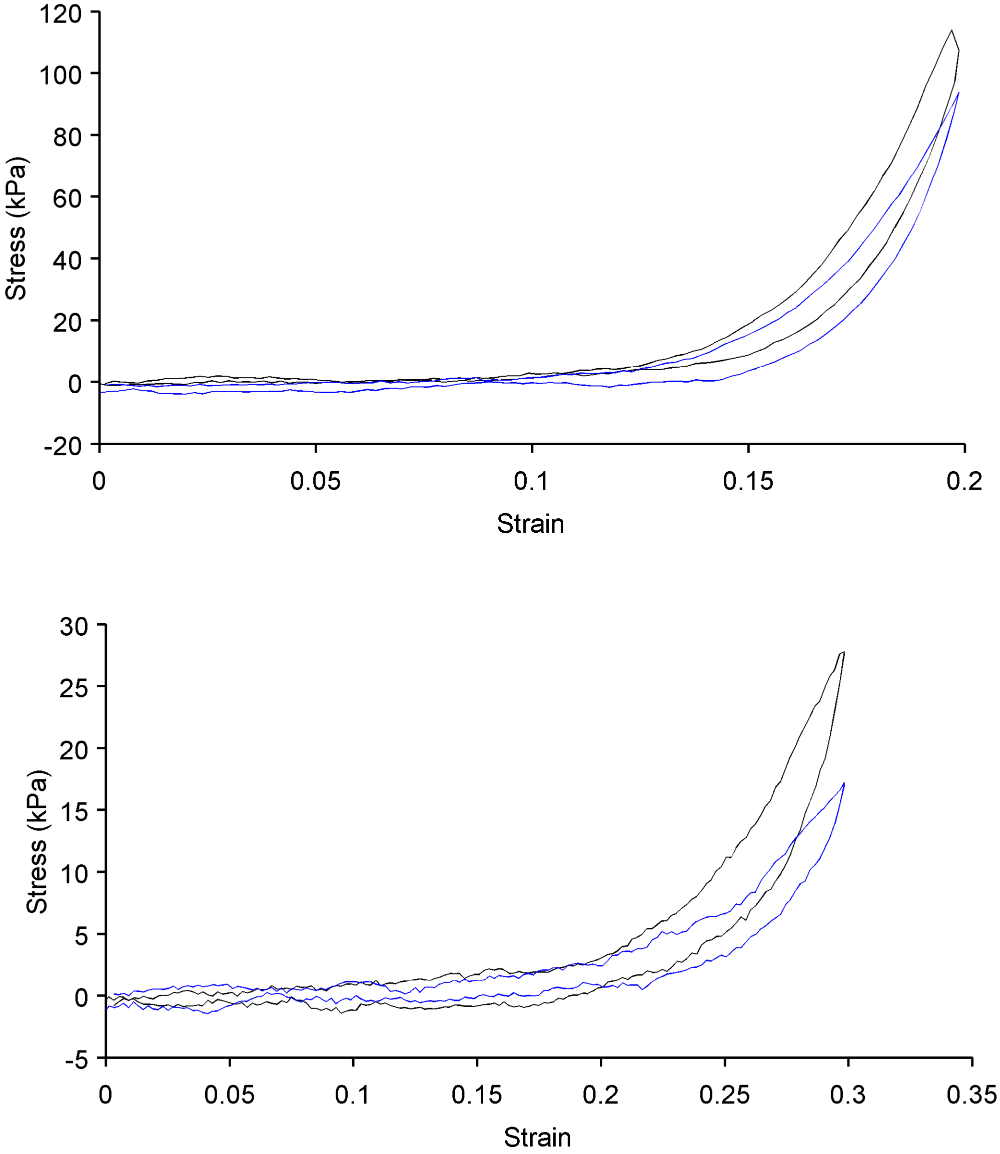

Figure 37: Engineering stress-strain curves for (Top) cell sheets in the direction of alignment before (black) and after (blue) decellularization and (Bottom) for cell sheet stress-strain curve in the direction perpendicular to alignment before (black) and after (blue) decellularization.

Modeling Results

The cell sheet stress-strain behavior was modeled using a hyper-elastic constitutive model developed by Lanir for the application to connective tissue[109]. For individual sheets, the stress-strain behavior was fit in both the aligned and transverse directions simultaneously and one set of fitting parameters were used to describe the mechanical behavior in both directions. Figure 38 shows a typical stress-strain curve for one aligned cell sheet where two samples were cut from the same sheet in both directions. The black and blue curves correspond to the aligned and transverse direction of the cell sheet, respectively. The dashed lines represent the experimental data and the solid lines represent the model fit. As can be seen in Figure 38, the model captures the stress strain behavior of the cell sheets in both directions while predicting an average angular alignment of 6.92°, which is similar to the assumed alignment direction. Figure 39 plots the stress-strain relationship for non-patterned samples cut from the same cell sheets.

The modeling results for 11 cell sheets (6 patterned, 5 non-patterned) are collected in Table 7. The modeling results for the aligned cell sheets show that the average predicted alignment direction is 11° (SEM=2.51) while the cell sheets grown on non-patterned substrates have an average fiber alignment of 45.3 (SEM=.53). The difference between the two fiber alignment predictions is statistically significant ($p<0.0005$). There is considerable variability between the fitting parameters c_1, c_2. While the optimization routine was bounded by an upper bound, a sufficient model prediction for the samples N1007 was not possible within that range. Therefore, the model upper limit was relaxed for that individual sample.

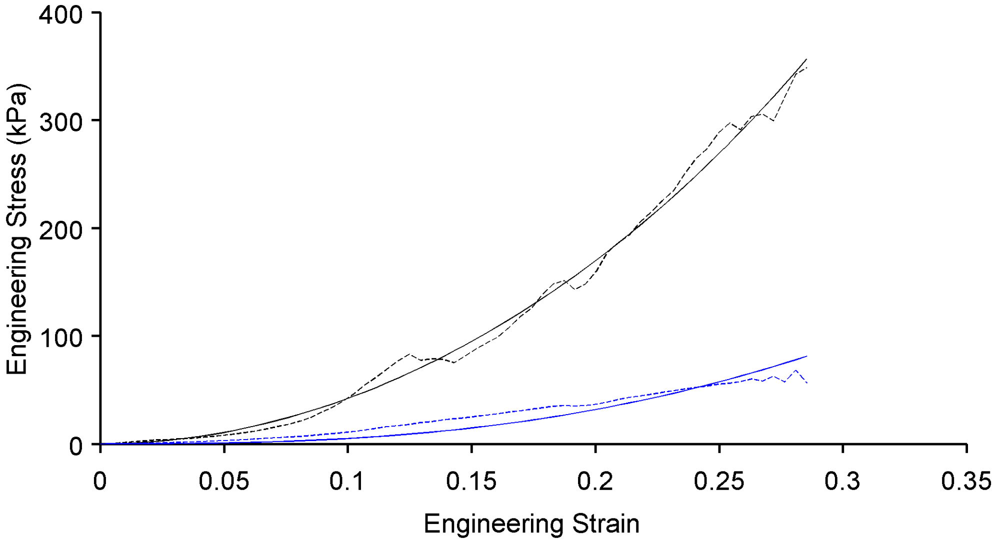

Figure 38: Stress-strain curve for aligned cell sheet in the alignment direction (black-dash) and transverse direction (blue-dash) with modeling results overlaid (solid). This sample corresponds to A105 from Table 7.

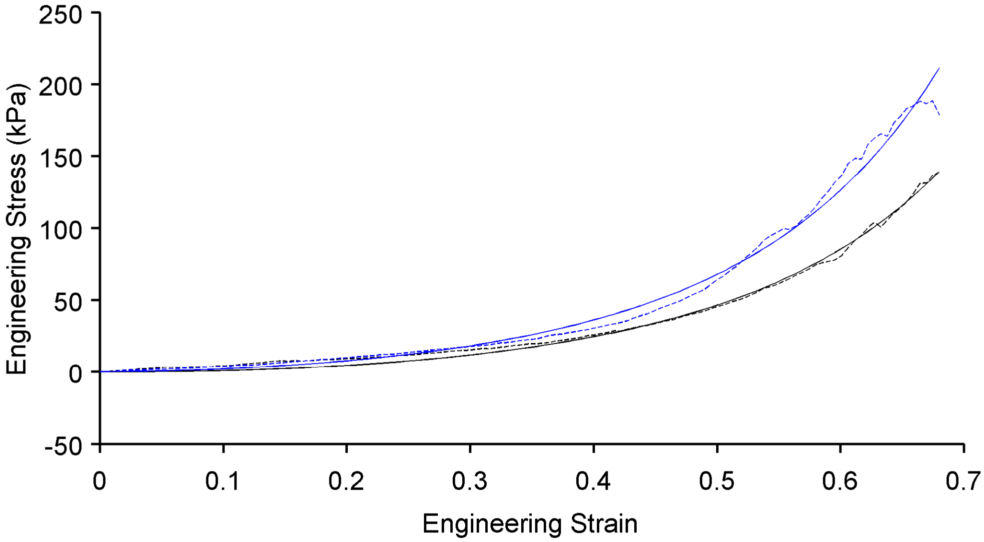

Figure 39: Stress-strain curve for aligned cell sheet in the alignment direction (black-dash) and transverse direction (blue-dash) with modeling results overlaid (solid). This sample corresponds to N1006 from Table 7.

	Angle	C1	C2
Patterned			
AM107	9.40	62004.28	10.64
AM104	22.13	20721.86	56.86
AM105	6.92	40382.36	12.61
AM109	4.00	10133.74	27.38
AM108	10.92	15035.98	17.92
AM102	10.98	100000.00	2.70
Non-Patterned			
N1009	44.15	9474.57	114.51
N1008	45.29	99955.21	50.11
N1006	46.01	47425.40	10.52
N1000	43.82	36156.70	32.07

Table 7: Model Fit Parameters for the constitutive relationship based upon the Lanir Strain Energy Function.

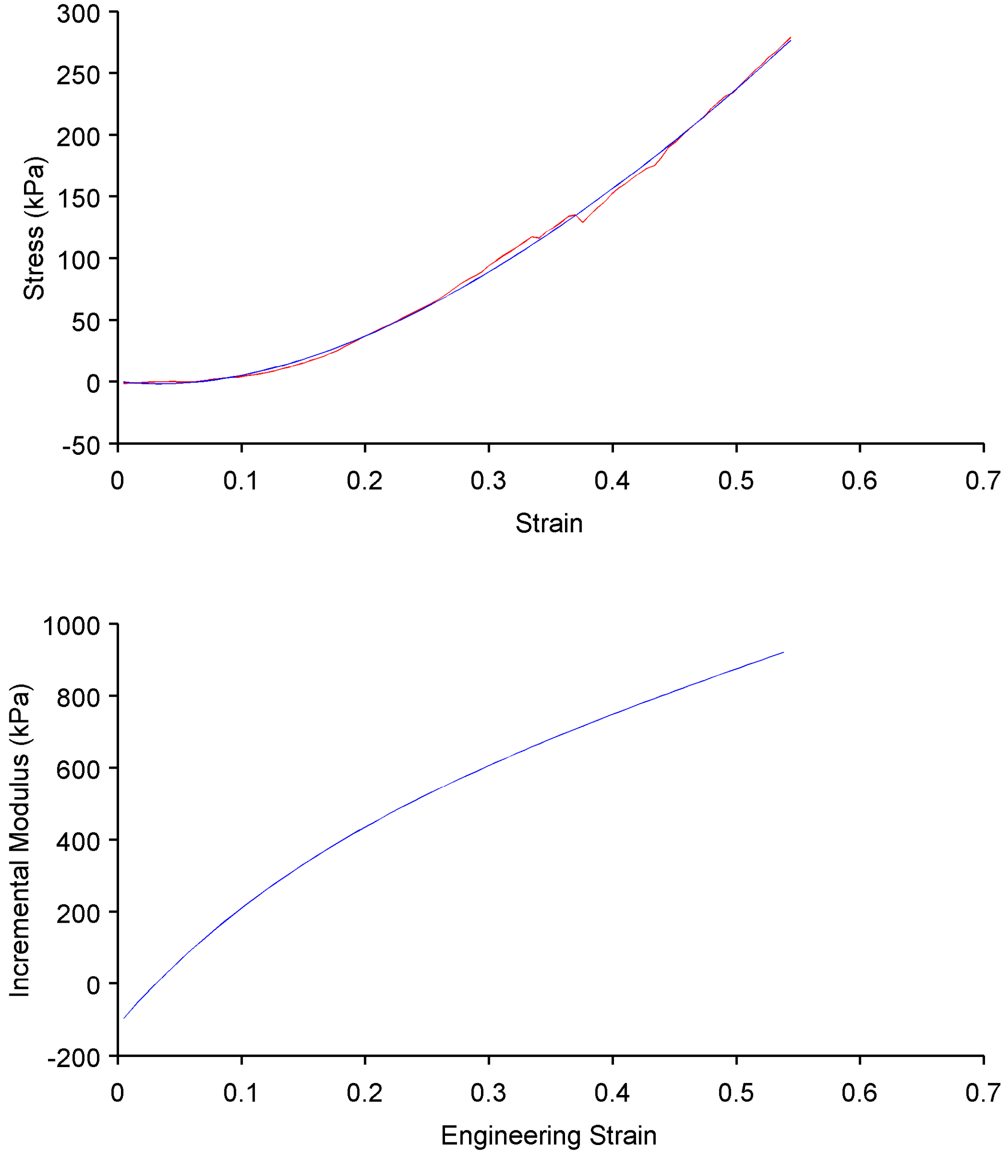

Figure 40: (Top) Stress strain Curve for an aligned cell sheet (red) with model fit overlaid (blue). (Bottom) Incremental modulus for the aligned cell sheet calculated from the model fit.

Discussion

Cell Sheet Composition and Structure

Cell sheets grown with mature bovine vascular smooth muscle cell sheets produce collagen. Measurements of the collagen content in cell sheets cultured for 11 days with only 4 days of ascorbic acid treatment suggest that the amount of collagen is significantly lower than native arterial tissue. Collagen content can be increased by increasing the cell sheet culture duration or applying mechanical stretching[76,134]. There was no significant difference between the collagen secreted by cells grown on non-patterned and patterned substrates (t-Test, $p=0.87$). This result corroborates previous results that showed that micropatterned substrates did not influence collagen and elastin production in vascular smooth muscle cells and fibroblasts[93,135]. However, previous research has also shown that cell alignment leads to increased contractile protein expression (myosin heavy chain and α-actin) in vascular smooth muscle cells[136,137]. The collagen quantification method cannot measure insoluble collagen, suggesting that the collagen measurements underestimate the total amount of collagen in the cell sheet. While the collagen quantification provides a poor absolute measurement of collagen content, it does confirm previous results that the substrates micropattern does not impact VSMC collagen secretion. This result suggests that any mechanical differences between cell sheets grown on patterned and non-patterned substrates are caused by differences in structure (cellular or extracellular), and not by composition.

As shown in Figure 29 in Chapter 3, bovine vascular smooth muscle cell sheets have quantifiable differences in the F-actin structure when grown on patterned substrates instead of non-patterned substrates. Images of the collagen structure captured in Figure 32 show that the collagen deposition is also structurally anisotropic. Because the cell sheets are compositionally the same, differences in mechanical response are most likely caused by structural differences in the sheets.

Compared to previous data collected within our lab, cell sheets grown for 2–3 weeks had a much higher degree of mechanical anisotropy. Previous experiments showed that cell sheets grown with the same cells for 6 weeks on aligned PDMS substrates were mechanically anisotropic, but only had a 50% increase in stiffness in the parallel direction compared to the (transverse) direction[93]. In those experiments cell sheets were grown for extended periods of times and allowed to grow multiple cells layers thick. As the cell sheets grew thicker, the effect of the underlying micropatterned substrates diminished and cells became randomly oriented beyond approximately 20 μm from the substrate surface when visualizing the collagen structure using confocal microscopy. In contrast, the cell sheets reported here are only about 18 μm thick and are well aligned. Thus, we demonstrate that the higher degree of structural anisotropy leads to a greater degree of mechanical anisotropy.

The cell sheet stress-strain curves for cell sheets cultured for 2–3 weeks exhibit the strain hardening behavior typical of soft tissue. Stress-strain curves for cell sheets grown for 6 weeks in culture do not show as much strain hardening[93]. ***This suggests that stacking cell sheets grown for shorter time durations has the potential to better replicate the native tissue mechanics.*** There has been quite a bit of progress developing cell sheet technology, yet it is clear that further progress is needed and will be made. The cell sheets have promising mechanical tensile behavior, but they currently lack restorative elasticity because of inelastic deformation at high strains. The next step in developing cell sheet technology further should be aimed at increasing the elastin content of the sheets as well as building and characterizing multi-layered cell sheet tissues.

The results from the decellularization experiments demonstrate that the cellular structure has a measurable impact upon the stiffness and strength of cell sheets. Removing cells from the cell sheet, leads to two fundamental changes. First the F-actin structure no longer bears any load. Secondly, removing the cells allows a greater degree of extracellular reorientation when the cell sheet is loaded. The experiments demonstrate that decellularization impacts the ability of the cell sheet to bear load in the direction of alignment compared to the direction of alignment as the maximum stress decreased 20 kPa compared to only 10 kPa in the transverse direction. But the data also suggests how important the F-actin structure is for bearing transverse loads in the cell sheets as the tangent modulus and max stress decrease proportionally larger amounts in the direction perpendicular to alignment. Because the decellularization process modifies the cell sheet structure, future work is needed to understand how the load that F-actin structure supports in the cell sheets. To do that, treating the cell sheets with cytoskeletal inhibitors such as cytochaslin d would inhibit the F-actin structure from bearing load.

The mechanical response of aligned cell sheets before and after decellularization is different from decellularized native tissue. Mechanical characterization of native and decellularized rabbit carotid arteries demonstrated that increased arterial stiffness and higher stresses at similar strains, whereas decellularized cell sheets showed decreased stiffness and decreased stress levels[61]. The differences between data could be attributed to differences in decellularization and mechanical testing protocols. The rabbit carotid arteries were decellularized for 7 days, while the cell sheets were decellularized for only 30 minutes[61]. Also, decellularization of the carotid artery may have led to differences in the initial geometry between the native and decellularized tissue. This would potentially lead to the decellularized artery appearing stiffer because the initial length was more elongated. However, the normal (non decellularized) cell sheet dimensions were used for the cell sheet mechanical measurements. These results also suggest that decellularized cell sheet matrix has sufficient mechanical integrity to be used as an anisotropic cell-free tissue engineered scaffold similar to recently published work on decellularized fibroblast sheets[138].

Ideally, decellularization removes cells without damaging the extracellular matrix, but in reality some damage is imparted upon the extracellular matrix. Treating tissue with a base such as sodium hydroxide has been shown to reduce the mechanical properties in tissue by cleaving collagen fibrils and disrupting collagen cross-links[53,139]. However, these experiments were preliminary and suggest that further work is needed to fully decompose the relative contribution of the different cell sheet structural components.

Mechanical Modeling

The modeling results presented in this dissertation capture the stress-strain behavior of aligned and non-aligned cell sheets during extension using a model derived from a hyperelastic strain energy function proposed by Lanir. The results demonstrate that this model formulation is capable of describing the stress-strain response of the cell sheets in both the parallel and transverse directions of the cell sheets. The model also helps describe the incremental modulus for the cell sheets as shown in Figure 40 by smoothing the experimental data.

The modeling results compiled in Table 7 show that while the model can be optimized to describe the data, there is variability in the fitting coefficients c_1, c_2. No assumption is made about the fiber angle, α, during the optimization process and the angle is considered a fitting parameter. Interestingly, the model fit results shows remarkable agreement between average angular orientations of the fiber direction between the patterned and non-patterned cell sheets despite no constraints or assumptions being made for angular orientation. As expected, the non-patterned cell sheets have a predicted directional alignment at 45.3° compared to 11.0° for the patterned cell sheets. The non-patterned cell sheets angular alignment of approximately 45°, is expected because the mechanical response should be identical in both directions. The model formulation assumes that the mechanical response is determined by a set of fibers oriented in a certain direction because the model does not include an isotropic component. The isotropic matrix can be attributed to the mechanical contribution of the cells and proteoglycans, commonly referred to as ground substance.[140,141] Because of this limitation, the angle or fibril alignment that the model predicts cannot be 0°. If the fibers were aligned perfectly with an angle of 0°, the transverse direction would have no ability to bear any load. A more realistic model formulation would incorporate an isotropic strain energy function that is based on the first tensor invariant of the right Cauchy-Green deformation tensor to represent the mechanical contribution of the isotropic matrix. The model is also limited because it only incorporates one set of fibers into the model formulation. The model could be improved by incorporating two fiber families symmetric about the direction of alignment to predict the mechanical response in order to better capture the cell sheet structure. Despite the limitations of the model, it appears to have a reasonable ability to predict alignment and therefore may be useful for classifying cell sheet mechanical behavior.

Despite the model being able to describe the mechanical data, the model is limited by several assumptions. First, the model can only describe cell sheet data only in extension because the model formulation does not predict any energy loss during mechanical stretching[133]. Secondly, the model assumes incompressibility in the model formulation (i.e., during deformation volume is conserved: mathematically, $det(F) = 1$), which is not necessarily true.

The model parameter estimation shows variability between fitting parameters for different tests. First, the variability could be caused by biological variability of the cell sheets samples as the mechanical properties of the cell sheets depend entirely on the cell-derived matrix. The fitting parameter variability could also be caused by experimental errors associated with measuring the dimensions of the cell sheets. It is also possible that the optimization routine will yield differing combinations of fit parameters for different optimization starting points. Therefore, the non-unique model fit is another potential source of variability. However, it is not uncommon to have significant fitting parameter variability when applying constitutive models to native arterial tissue[27].

The modeling efforts suggest that more effort is needed to better characterize the mechanics of individual cell sheets. First, it is essential to optically track the cell sheet during deformation to better understand how the geometry changes during mechanical testing as well as to provide insight in strains that develop in the transverse direction of the cell sheet. Secondly, optically tracking the cell sheets during testing would build understanding about how the cell sheets fail. This could lead to formulation of a cell sheet failure model similar to work done by Ritter *et al.*[142].

The model presented in this dissertation is clearly capable of describing the mechanical properties of aligned and non-aligned cell sheets as well as classifying cell sheet alignment. This model represents an initial effort to model the mechanics of aligned cell sheets to eventually be incorporated into a mechanical model to predict the mechanics of stacked cell sheets. This model provides insight that can inform formulation of more refined experimental testing approaches and higher fidelity mechanical models.

Chapter 5: Future Directions

Aim 1: Develop a uniaxial tensile tester and force sensor capable of measuring the mechanics of cell sheet based tissues.

The Hall-Effect force sensor design presented in this dissertation provides accurate force measurements that characterize the mechanical properties of single layer cell sheets; yet, this sensor can be improved. As discussed in Chapter 2, the physical sensor dimensions precludes it from effectively measuring some steeper magnetic fields for some magnet pair combinations.

Hall-Effect Integrated sensors are evolving across multiple application domains. For example, a Hall-Effect sensor (Sentron, Leek, Netherlands) has recently been introduced to measure the magnetic field parallel to the face of the (HE) sensor (as opposed to normal to the face of the sensor). By measuring the magnetic field parallel to the face of the sensor, the physical constraints posed by the sensor change significantly and can enable the sensor to detect magnetic fields that otherwise would be impossible to sample. Consider that a COMSOL simulation predicts a magnetic field gradient that produces full sensor output over 2.5 μm displacement using the new Hall-Effect sensor. The magnet pair used in this dissertation produces full sensor output over a displacement of 400 μm. Increasing the magnetic field gradient that the Hall-Effect sensor measures has two fundamental impacts upon the beam design. Because the Hall-Effect sensor measures smaller tip displacements than other sensors in this regime, it increases the beam sensitivity. For example, a sensor configuration capable of measuring forces in the 0–5 mN range would potentially be able to measure forces in the 0–50 μN range.

Practically, stiffer materials are less likely to plastically deform, break and are easier to handle. Because the current sensor is relatively soft, environmental mechanical noise causes the beam to vibrate at low frequencies (<10 Hz). This makes it difficult to filter out noise. A stiffer beam reduces bending and torsional beam deformation, and thereby improves sensor performance. Future work could identify an improved sensor design and enhance both sensor accuracy and sensitivity.

Specific Aim 2: To develop a thermo-responsive substrate system for the culture of vascular smooth muscle cell sheets for arterial tissue engineering.

The work in Aim 2 of this dissertation details the development of a reliable substrate platform for the long-term growth of contractile, aligned, vascular smooth muscle-based cell sheets. The grafting method presented in this dissertation requires precise timing to control the surface concentration of benzophenone, the photo-initiator, as well as control the duration of UV exposure. This dependence upon timing makes the grafting process difficult and slightly susceptible to variability. Second, the grafting process used an excessive quantity of expensive NIPAAm monomer, while approximately 99.99% of the monomer does react with the surface and is wasted. Future work should minimize the amount of wasted monomer and decrease the time dependency of the reaction.

To overcome some of these difficulties, preliminary work has modified the grafting process to use ‘small volumes’ of NIPAAm monomer and benzophenone. Instead of soaking substrates in benzophenone for a certain length of time, the substrates are soaked in a small volume (4 uL/cm^2) of benzophenone until all solvent has been absorbed into the substrate. Similarly, the substrates are exposed to small volume of NIPAAm monomer (6 uL/cm^2) during UV irradiation. Optimal grafting conditions have yet to be determined, but the preliminary results have demonstrated that this grafting method is less sensitive to heterogeneities in surface concentration of photo-initiator and is not as sensitive to time.

Specific Aim 3: To characterize the mechanical and structural properties of vascular smooth muscle cell sheets and model their mechanical behavior.

The results from the mechanical characterization of the aligned cell sheets demonstrated that the cell sheets are stiffer in the direction of alignment compared to the direction perpendicular to alignment by nearly an order of magnitude. Unfortunately, the single layers of cell sheets undergo plastic deformation when loaded to high strains (>20%). Because the cell sheets exhibit limited elasticity, the cells sheets in their current form require further enhancement for suitability as a tissue engineered vascular graft.

Future work should be devoted towards improving the elastic properties of the cell sheet based tissues by increasing the elastin content in the cell sheets. Mature cells typically do not produce elastin in sufficient quantities, making growing an arterial tissue with mature cell derived ECM a challenge. Therefore, future work needs to be devoted towards identifying pathways to increase elastin content in these cell sheets

One method to improve the elastin content in the cell sheets might entail increasing elastin synthesis in mature vascular smooth muscle cells. For example, TGF-β and retinoic acid have been shown to lead elastin synthesis in vascular smooth muscle cells[22,143]. Increased elastin content achieved by using a neonatal cell source[22]. Then, the elastin rich cell sheet could be decellularized and the extracellular matrix sheet could be incorporated as an additional layer in an arterial graft. Lastly, the incorporation of recombinant-based elastin networks would potentially overcome this limitation. Recently, several groups have made progress producing recombinant elastin for the use in arterial tissue engineering[144].

The mechanical modeling results presented in this dissertation are preliminary and future work should be focused on model refinement to better capture the mechanical behavior of cell sheets. For example, a model developed by Gasser *et al.* incorporates fiber dispersion and could better predict the mechanical behavior of cell sheet tissues[145]. Beyond building models to predict single layer cell sheet mechanics, effort should be devoted to incorporating the mechanical models into a finite element framework such as ABAQUS to build more complex mechanical models of stacked cell sheets.

Future work should also be devoted towards characterizing the mechanics of multi-layered cell sheet based tissues with each layer having different directional alignment. These experiments should be designed to understand how alignment of individual layers relates to tissue level mechanics while also providing an experimental validation of finite element based modeling results. Future experimental and modeling studies would continue to build upon the foundation presented in this dissertation for building a cell sheet based vascular graft.

List of Abbreviated Journal Titles

Abbreviation	**Full Title**
Acta Biomater.	Acta Biomaterialia
Adv. Drug Deliv. Rev.	Advanced Drug Delivery Reviews
Adv. Mater.	Advanced Materials
Am. J. Physiol.	American Journal of Physiology
Am. J. Physiol. Heart Circ. Physiol.	American Journal of Physiology. Heart and Circulatory Physiology
Am. J. Sports Med.	American journal of sports medicine
Ann. Biomed. Eng.	Annals of Biomedical Engineering
Ann. Surg.	Annals of Surgery
Annu. Rev. Biomed. Eng	Annual Review of Biomedical Engineering
Arch Pediatr Adolesc Med.	Archives of Pediatrics and Adolescent Medicine
Arch. Surg.	Archives of Surgery
Biochem. J.	Biochemical Journal
Biomed. Mater. Eng.	Biomedical Materials Engineering
Biophys. J.	Biophysical Journal
Biotechnol. Adv.	Biotechnology Advances
Biotechnol. Prog.	Biotechnology Progress
Birth Defects Res. C. Embryo Today	Birth Defects Research Part C: Embryo Today: Reviews
Br. J. Surg.	British Journal of Surgery
Cardiovasc. Eng. Technol.	Cardiovascular Engineering and Technology
Cardiovasc. Pathol.	Cardiovascular Pathology
Cell Transplant.	Cell Transplantation
Circ. Res.	Circulation Research
Clin. Cardiol.	Clinical Cardiology
Compr. Physiol.	Comprehensive Physiology
Comput. Methods Appl. Mech. Eng.	Computer Methods in Applied Mechanics and Engineering
Curr. Opin. Biotechnol.	Current Opinion in Biotechnology

Exp. Cell Res.	Experimental Cell Research
FASEB J.	FASEB Journal
J. Biol. Eng.	Journal of Biological Engineering
J. Biomater. Sci. Polym. Ed.	Journal of Biomaterials Science. Polymer Edition
J. Biomech.	Journal of Biomechanics
J. Biomech. Eng.	Journal of Biomechanical Engineering
J. Biomed. Mater. Res. A	Journal of Biomedical Materials Research Part A
J. Biomed. Mater. Res. B. Appl. Biomater.	Journal of Biomedical Materials Research Part B: Applied Biomaterials
J. Cell Sci.	Journal of Cell Science
J. Cell. Physiol.	Journal of Cellular Physiology
J. Colloid Interface Sci.	Journal of Colloid and Interface Science
J. Elast.	Journal of Elasticity
J. Exp. Zool.	Journal of Experimental Zoology Part A: Ecological Genetics and Physiology
J. Histochem. Cytochem.	Journal of Histochemistry & Cytochemistry
J. Muscle Res. Cell Motil.	Journal of Muscle Research and Cell Motility
J. R. Soc. Interface	Journal of the Royal Society Interface
J. Thorac. Cardiovasc. Surg.	Journal of Thoracic and Cardiovascular Surgery
J. Tissue Eng. Regen. Med.	Journal of Tissue Engineering and Regenerative Medicine
J. Vasc. Surg.	Journal of Vascular Surgery
Lab. Invest.	Laboratory Investigation
Macromol. Biosci.	Macromolecular Bioscience
Mater. Sci. Eng.	Materials Science and Engineering: A
Nat. Biotechnol.	Nature Biotechnology
Nat. Commun.	Nature Communications
Nat. Mater.	Nature Materials
Nat. Rev. Mol. Cell Biol.	Nature Reviews. Molecular Cell Biology

Physiol. Rev.	Physiological Reviews
Proc. Natl. Acad. Sci. U.S.A.	Proceedings of the National Academy of Sciences of the United States of America
Proc. R. Soc. A Math. Phys. Eng. Sci.	Proceedings of the Royal Society of London A: Mathematical, Physical and Engineering Sciences
Radiat. Phys. Chem.	Radiation Physics and Chemistry
Sci. Transl. Med.	Science Translational Medicine
Tissue Eng. Part A	Tissue Engineering Part A
Trends Biotechnol.	Trends in Biotechnology
World J. Surg.	World Journal of Surgery

Bibliography

1. Lloyd-Jones, D. *et al.* Heart Disease and Stroke Statistics—2010 Update. *Circulation* **121,** e46–e215

2. Ross, R. The pathogensis of atherosclerosis: a perspective fo the 1990s. *Nature* **362,** 801–809 (1993).

3. Lusis, A. J. Atherosclerosis. *Nature* **407,** 233–241 (2000).

4. Kumar, V. a, Brewster, L. P., Caves, J. M. & Chaikof, E. L. Tissue Engineering of Blood Vessels: Functional Requirements, Progress, and Future Challenges. *Cardiovasc. Eng. Technol.* **2,** 137–148 (2011).

5. Martinez, R. M. Perspectives in Pediatric Cardiology: Surgery of Congenital Heart Disease: Pediatric Cardiac Care Consortium, 1984–1995. *Arch Pediatr Adolesc Med* **153,** 432

6. Lloyd-Jones, D. *et al.* Heart disease and stroke statistics--2010 update: a report from the American Heart Association. *Circulation* **121,** e46–e215 (2010).

7. Hillis, L. D. *et al.* 2011 ACCF/AHA Guideline for Coronary Artery Bypass Graft Surgery: Executive Summary: A Report of the American College of Cardiology Foundation/American Heart Association Task Force on Practice Guidelines. *Circulation* **124,** 2610–2642 (2011).

8. Wang, X., Lin, P., Yao, Q. & Chen, C. Development of small-diameter vascular grafts. *World J. Surg.* **31,** 682–689 (2007).

9. Mitchell, S. L. & Niklason, L. E. Requirements for growing tissue-engineered vascular grafts. *Cardiovasc. Pathol.* **12,** 59–64 (2003).

10. Ravi, S., Qu, Z. & Chaikof, E. L. Polymeric materials for tissue engineering of arterial substitutes. *Vascular* **17 Suppl 1,** S45–S54 (2009).

11. Rhodin, J. A. G. Architecture of the Vessel Wall. *Compr. Physiol.* 1–31 (2011).

12. Davis, E. C. Smooth muscle cell to elastic lamina connections in developing mouse aorta. Role in aortic medial organization. *Lab. Invest.* **68,** 89–99

13. Lüscher, T. F. & Barton, M. Biology of the endothelium. *Clin. Cardiol.* **20,** II–3–10 (1997).

14. Wolinsky, H. & Glagov, S. Structural Basis for the Static Mechanical Properties of the Aortic Media. *Circ. Res.* **14,** 400–13 (1964).

15. Wagenseil, J. E. & Mecham, R. P. Vascular extracellular matrix and arterial mechanics. *Physiol. Rev.* **89,** 957–989 (2009).

16. Owens, G. K. Regulation of differentiation of vascular smooth muscle cells. *Physiol. Rev.* **75,** 487–517 (1995).

17. Clark, J. M. & Glagov, S. Transmural organization of the arterial media. The lamellar unit revisited. *Arteriosclerosis* **5,** 19–34 (1985).

18. Holzapfel, G. A., Gasser, T. C. & Ogden, R. A. Y. W. A New Constitutive Framework for Arterial Wall Mechanics and a Comparative Study of Material Models. *J. Elast.* 1–48 (2001).

19. Karnik, S. K. *et al.* A critical role for elastin signaling in vascular morphogenesis and disease. *Development* **130,** 411–423 (2003).

20. Kielty, C. M., Sherratt, M. J. & Shuttleworth, C. A. Elastic fibres. *J. Cell Sci.* **115,** 2817–28 (2002).

21. Wagenseil, J. E. & Mecham, R. P. New insights into elastic fiber assembly. *Birth Defects Res. C. Embryo Today* **81,** 229–40 (2007).

22. Patel, A., Fine, B., Sandig, M. & Mequanint, K. Elastin biosynthesis: The missing link in tissue-engineered blood vessels. *Cardiovasc. Res.* **71,** 40–9 (2006).

23. Li, D. Y. *et al.* Elastin is an essential determinant of arterial morphogenesis. *Nature* **393,** 276–280 (1998).

24. Kadler, K. E., Holmes, D. F., Trotter, J. a & Chapman, J. a. Collagen fibril formation. *Biochem. J.* **316 (Pt 1,** 1–11 (1996).

25. Wenger, M. P. E., Bozec, L., Horton, M. a & Mesquida, P. Mechanical properties of collagen fibrils. *Biophys. J.* **93,** 1255–1263 (2007).

26. Sommer, G., Regitnig, P., Költringer, L. & Holzapfel, G. a. Biaxial mechanical properties of intact and layer-dissected human carotid arteries at physiological and supraphysiological loadings. *Am. J. Physiol. Heart Circ. Physiol.* **298,** H898–H912 (2010).

27. Holzapfel, G. A., Sommer, G., Gasser, C. T. & Regitnig, P. Determination of layer-specic mechanical properties of human coronary arteries with

nonatherosclerotic intimal thickening and related constitutive modeling. *Am. J. Physiol. Heart Circ. Physiol.* **289,** 2048–2058 (2005).

28. Wolinsky, H. & Glagov, S. A Lamellar Unit of Aortic Medial Structure and Function in Mammals. *Circ. Res.* **20,** 99–111 (1967).

29. Wagenseil, J. E. & Mecham, R. P. Vascular Extracellular Matrix and Arterial Mechanics. *Physiol. Rev.* 957–989 (2009). doi:10.1152/physrev.00041.2008.

30. Ross, R. The Elastic Fiber a Review. *J. Histochem. Cytochem.* **21,** 199–208 (1973).

31. Li, B. & Daggett, V. Molecular basis for the extensibility of elastin. *J. Muscle Res. Cell Motil.* **23,** 561–73 (2002).

32. Holzapfel, G. A. in *Collagen Struct. Mech.* (Fratzl, P.) 285–324 (Springer US, 2008).

33. Dobrin, P. B., Baker, W. H. & Gley, W. C. Elastolytic and collagenolytic studies of arteries. Implications for the mechanical properties of aneurysms. *Arch. Surg.* **119,** 405–409 (1984).

34. Han, H.-C., Ku, D. N. & Vito, R. P. Arterial Wall Adaptation under Elevated Longitudinal Stretch in Organ Culture. *Ann. Biomed. Eng.* **31,** 403–411 (2003).

35. Ballyk, P. D., Walsh, C., Butany, J. & Ojha, M. Compliance mismatch may promote graft-artery intimal hyperplasia by altering suture-line stresses. *J. Biomech.* **31,** 229–237 (1997).

36. Davies, A. H., Magee, T. R., Baird, R. N., Sheffield, E. & Horrocks, M. Vein compliance: a preoperative indicator of vein morphology and of veins at risk of vascular graft stenosis. *Br. J. Surg.* **79,** 1019–21 (1992).

37. Butler, D. L., Goldstein, S. A. & Guilak, F. Functional tissue engineering: the role of biomechanics. *J. Biomech. Eng.* **122,** 570–5 (2000).

38. Fung, Y. *Biomechanics: Mechanical Properties of Living Tissues, Second Edition*. (Springer, 1993).

39. Vande Geest, J. P., Sacks, M. S., Vorp, D. a & Vande, J. P. A planar biaxial constitutive relation for the luminal layer of intra-luminal thrombus in abdominal aortic aneurysms. *J. Biomech.* **39,** 2347–54 (2006).

40. Debes, J. C. & Fung, Y. C. Biaxial mechanics of excised canine pulmonary arteries. *Am. J. Physiol.* **269,** H433–42 (1995).

41. Billiar, K. L. & Sacks, M. S. Biaxial mechanical properties of the natural and glutaraldehyde treated aortic valve cusp-Part I: Experimental results. *J. Biomech. Eng.* **122,** 23–30 (2000).

42. Schulze-Bauer, C. a J. & Holzapfel, G. a. Determination of constitutive equations for human arteries from clinical data. *J. Biomech.* **36,** 165–9 (2003).

43. LoGerfo, F. W., Quist, W. C., Nowak, M. D., Crawshaw, H. M. & Haudenschild, C. C. Downstream anastomotic hyperplasia. A mechanism of failure in Dacron arterial grafts. *Ann. Surg.* **197,** 479–483 (1983).

44. Weinberg, C. B. & Bell, E. A blood vessel model constructed from collagen and cultured vascular cells. *Science* **231,** 397–400 (1986).

45. Elbert, D. L. Bottom-up tissue engineering. *Curr. Opin. Biotechnol.* **22,** 674–680 (2011).

46. Nichol, J. W. & Khademhosseini, A. Modular tissue engineering: engineering biological tissues from the bottom up. *Soft Matter* **5,** 1312 (2009).

47. Shinoka, T. *et al.* Creation of viable pulmonary artery autografts through tissue engineering. *J. Thorac. Cardiovasc. Surg.* **115,** 536–45; discussion 545–6 (1998).

48. Niklason, L. E. Functional Arteries Grown in Vitro. *Science* **284,** 489–493 (1999).

49. Dahl, S. L. M. *et al.* Readily available tissue-engineered vascular grafts. *Sci. Transl. Med.* **3,** 68ra9 (2011).

50. Brennan, M. P. *et al.* Tissue-engineered vascular grafts demonstrate evidence of growth and development when implanted in a juvenile animal model. *Ann. Surg.* **248,** 370–377 (2008).

51. Roh, J. D. *et al.* Tissue-engineered vascular grafts transform into mature blood vessels via an inflammation-mediated process of vascular remodeling. *Proc. Natl. Acad. Sci. U. S. A.* **107,** 4669–74 (2010).

52. Hibino, N. *et al.* Tissue-engineered vascular grafts form neovessels that arise from regeneration of the adjacent blood vessel. *FASEB J.* **25,** 2731–9 (2011).

53. Gilbert, T. W., Sellaro, T. L. & Badylak, S. F. Decellularization of tissues and organs. *Biomaterials* **27,** 3675–83 (2006).

54. Schaner, P. J. *et al.* Decellularized vein as a potential scaffold for vascular tissue engineering. *J. Vasc. Surg.* **40,** 146–53 (2004).

55. Cho, S.-W. *et al.* Small-diameter blood vessels engineered with bone marrow-derived cells. *Ann. Surg.* **241,** 506–515 (2005).

56. Gui, L., Muto, A., Chan, S. A., Breuer, C. K. & Niklason, L. E. Development of decellularized human umbilical arteries as small-diameter vascular grafts. *Tissue Eng. Part A* **15,** 2665–2676 (2009).

57. Badylak, S. F., Taylor, D. & Uygun, K. Whole Organ Tissue Engineering: Decellularization and Recellularization of Three-Dimensional Matrix Scaffolds. *Annu. Rev. Biomed. Eng.* **13,** 110301095218061 (2010).

58. Fu, R. H. *et al.* Decellularization and recellularization technologies in tissue engineering. *Cell Transplant.* **23,** 621–630 (2014).

59. Crapo, P., Gilbert, T. & Badylak, S. An overview of tissue and whole organ decellularization processes. *Biomaterials* **32,** 3233–3243 (2011).

60. Badylak, S. F., Freytes, D. O. & Gilbert, T. W. Extracellular matrix as a biological scaffold material: Structure and function. *Acta Biomater.* **5,** 1–13 (2009).

61. Williams, C. *et al.* Altered structural and mechanical properties in decellularized rabbit carotid arteries. *Acta Biomater.* **5,** 993–1005 (2009).

62. Miller, J. S. *et al.* Rapid casting of patterned vascular networks for perfusable engineered three-dimensional tissues. *Nat. Mater.* **11,** 768–774 (2012).

63. Murphy, S. V & Atala, A. 3D bioprinting of tissues and organs. *Nat. Biotechnol.* **32,** 773–785 (2014).

64. L'Heureux, N. *et al.* A completely biological tissue-engineered human blood vessel. *FASEB J.* **12,** 47–56 (1998).

65. Hirose, M., Kwon, O. H., Yamato, M., Kikuchi, a & Okano, T. Creation of designed shape cell sheets that are noninvasively harvested and moved onto another surface. *Biomacromolecules* **1,** 377–81 (2000).

66. Akimoto, J. *et al.* Facile cell sheet manipulation and transplantation by using in situ gelation method. *J. Biomed. Mater. Res. B. Appl. Biomater.* **102,** 1659–68 (2014).

67. Ke, Q. *et al.* Carrier-free epithelial cell sheets prepared by enzymatic degradation of collagen gel. *J. Tissue Eng. Regen. Med.* **5,** 138–45 (2011).

68. Okano, T., Yamada, N., Sakai, H. & Sakurai, Y. A novel recovery system for cultured cells using plasma-treated polystyrene dishes grafted with poly(N-isopropylacrylamide). *J. Biomed. Mater. Res.* **27,** 1243–51 (1993).

69. Wu, C. & Zhou, S. Laser Light Scattering Study of the Phase Transition of Poly(N-isopropylacrylamide) in Water. 1. Single Chain. *Macromolecules* **28,** 8381–8387 (1995).

70. Wang, X., Qiu, X. & Wu, C. Comparison of the Coil-to-Globule and the Globule-to-Coil Transitions of a Single Poly(N-isopropylacrylamide) Homopoylmer Chain in Water. *Macromolecules* **31,** 2972–2976 (1998).

71. Akiyama, Y., Kikuchi, A., Yamato, M. & Okano, T. Ultrathin poly(N-isopropylacrylamide) grafted layer on polystyrene surfaces for cell adhesion/detachment control. *Langmuir* **20,** 5506–11 (2004).

72. Tekin, H., Sanchez, J. & Tsinman, T. Thermoresponsive Platforms for Tissue Engineering and Regenerative Medicine. *AIChE J.* **57,** 3249–3258 (2011).

73. Patel, N. G. & Zhang, G. Responsive systems for cell sheet detachment. *Organogenesis* **9,** 93–100 (2013).

74. Da Silva, R. M. P., Mano, J. F., Reis, R. L., Mano, F. & Silva, R. M. P. Smart thermoresponsive coatings and surfaces for tissue engineering: switching cell-material boundaries. *Trends Biotechnol.* **25,** 577–83 (2007).

75. Brown, X. Q., Ookawa, K. & Wong, J. Y. Evaluation of polydimethylsiloxane scaffolds with physiologically-relevant elastic moduli: interplay of substrate mechanics and surface chemistry effects on vascular smooth muscle cell response. *Biomaterials* **26,** 3123–9 (2005).

76. Lee, E. L., Recum, H. A. Von & von Recum, H. a. Cell culture platform with mechanical conditioning and nondamaging cellular detachment. *J. Biomed. Mater. Res. Part A* **93,** 411–418 (2010).

77. Ebara, M., Hoffman, J. M., Stayton, P. S. & Hoffman, A. S. Surface modification of microfluidic channels by UV-mediated graft polymerization of non-fouling and ‘smart’ polymers. *Radiat. Phys. Chem.* **76,** 1409–1413 (2007).

78. Ma, D., Chen, H., Shi, D., Li, Z. & Wang, J. Preparation and characterization of thermo-responsive PDMS surfaces grafted with poly(N-isopropylacrylamide) by

benzophenone-initiated photopolymerization. *J. Colloid Interface Sci.* **332,** 85–90 (2009).

79. Rayatpisheh, S., Li, P. & Chan-park, M. B. Argon-plasma-induced ultrathin thermal grafting of thermoresponsive pNIPAm coating for contractile patterned human SMC sheet engineering. *Macromol. Biosci.* **12,** 937–45 (2012).

80. Akiyama, Y., Yamato, M. & Okano, T. Preparation of Poly (N-isopropylacrylamide) Grafted Polydimethylsiloxane by Using Electron Beam Irradiation. *J. Robot. Mechatronics* **25,** 631–636 (2013).

81. Choi, S., Choi, B.-C., Xue, C. & Leckband, D. Protein adsorption mechanisms determine the efficiency of thermally controlled cell adhesion on poly(N-isopropyl acrylamide) brushes. *Biomacromolecules* **14,** 92–100 (2013).

82. Lee, S. G. *et al.* Deswelling Mechanisms of Surface-Grafted Poly(NIPAAm) Brush: Molecular Dynamics Simulation Approach. *J. Phys. Chem.* **116,** 15974–15985 (2012).

83. Takahashi, H., Nakayama, M., Yamato, M. & Okano, T. Controlled chain length and graft density of thermoresponsive polymer brushes for optimizing cell sheet harvest. *Biomacromolecules* **11,** 1991–1999 (2010).

84. Li, Y. *et al.* Engineering cell alignment in vitro. *Biotechnol. Adv.* **32,** 347–365 (2014).

85. Weiss, P. & Hiscoe, H. B. Experiments on the mechanism of nerve growth. *J. Exp. Zool.* **107,** 315–95 (1948).

86. Brunette, D. M. Spreading and orientation of epithelial cells on grooved substrata. *Exp. Cell Res.* **167,** 203–217 (1986).

87. Clark, P., Connolly, P., Curtis, A. S., Dow, J. A. & Wilkinson, C. D. Cell guidance by ultrafine topography in vitro. *J. Cell Sci.* **99 (Pt 1),** 73–7 (1991).

88. Pilia, M., Guda, T., Shiels, S. M. & Appleford, M. R. Influence of substrate curvature on osteoblast orientation and extracellular matrix deposition. *J. Biol. Eng.* **7,** 23 (2013).

89. Chen, C. S., Mrksich, M., Huang, S., Whitesides, G. M. & Ingber, D. E. Micropatterned surfaces for control of cell shape, position, and function. *Biotechnol. Prog.* **14,** 356–363 (1998).

90. Sarkar, S., Dadhania, M., Rourke, P., Desai, T. a & Wong, J. Y. Vascular tissue engineering: microtextured scaffold templates to control organization of vascular smooth muscle cells and extracellular matrix. *Acta Biomater.* **1,** 93–100 (2005).

91. Zahor, D., Radko, a., Vago, R. & Gheber, L. a. Organization of mesenchymal stem cells is controlled by micropatterned silicon substrates. *Mater. Sci. Eng. C* **27,** 117–121 (2007).

92. Griffith, L. G. & Swartz, M. a. Capturing complex 3D tissue physiology in vitro. *Nat. Rev. Mol. Cell Biol.* **7,** 211–224 (2006).

93. Isenberg, B. C. *et al.* Micropatterned cell sheets with defined cell and extracellular matrix orientation exhibit anisotropic mechanical properties. *J. Biomech.* **45,** 756–61 (2012).

94. Williams, C. *et al.* Aligned Cell Sheets Grown on Thermo-Responsive Substrates with Microcontact Printed Protein Patterns. *Adv. Mater.* **21,** 2161–2164 (2009).

95. Williams, C., Xie, A. W., Yamato, M., Okano, T. & Wong, J. Y. Stacking of aligned cell sheets for layer-by-layer control of complex tissue structure. *Biomaterials* **32,** 5625–32 (2011).

96. Pang, Y., Wang, X., Lee, D. & Greisler, H. P. Dynamic quantitative visualization of single cell alignment and migration and matrix remodeling in 3-D collagen hydrogels under mechanical force. *Biomaterials* **32,** 3776–3783 (2011).

97. Liu, Y., Lu, J., Li, H., Wei, J. & Li, X. Engineering blood vessels through micropatterned coculture of vascular endothelial and smooth muscle cells on bilayered electrospun fibrous mats with pDNA inoculations. *Acta Biomater.* **11,** 114–125 (2015).

98. Wang, J. H. C., Goldschmidt-Clermont, P., Wille, J. & Yin, F. C. P. Specificity of endothelial cell reorientation in response to cyclic mechanical stretching. *J. Biomech.* **34,** 1563–1572 (2001).

99. Hsu, H.-J., Lee, C.-F., Locke, A., Vanderzyl, S. Q. & Kaunas, R. Stretch-induced stress fiber remodeling and the activations of JNK and ERK depend on mechanical strain rate, but not FAK. *PLoS One* **5,** e12470 (2010).

100. Kaunas, R., Nguyen, P., Usami, S. & Chien, S. Cooperative effects of Rho and mechanical stretch on stress fiber organization. *Proc. Natl. Acad. Sci. U. S. A.* **102,** 15895–15900 (2005).

101. Livne, A., Bouchbinder, E. & Geiger, B. Cell reorientation under cyclic stretching. *Nat. Commun.* **5,** 3938 (2014).

102. Crouchley, C. M., Barron, V., Punchard, M., O'Cearbhaill, E. & Smith, T. Development of a co-culture system for tissue engineered vascular grafts. *Biomed. Mater. Eng.* **18,** 291–4 (2008).

103. Kakisis, J. D., Liapis, C. D. & Sumpio, B. E. Effects of Cyclic Strain on Cells. *Endothelium* **11,** 17–28 (2004).

104. Humphrey, J. D. Review Paper: Continuum biomechanics of soft biological tissues. *Proc. R. Soc. A Math. Phys. Eng. Sci.* **459,** 3–46 (2003).

105. Ingber, D. E. *et al.* Tissue engineering and developmental biology: going biomimetic. *Tissue Eng.* **12,** 3265–83 (2006).

106. Niklason, L. E. *et al.* Enabling tools for engineering collagenous tissues integrating bioreactors, intravital imaging, and biomechanical modeling. *Proc. Natl. Acad. Sci. U. S. A.* **107,** 3335–9 (2010).

107. Fung, Y. C., Fronek, K. & Patitucci, P. Pseudoelasticity of arteries and the choice of its mathematical expression. *Am. J. Physiol.* **237,** H620–H631 (1979).

108. Zulliger, M. a, Fridez, P., Hayashi, K. & Stergiopulos, N. A strain energy function for arteries accounting for wall composition and structure. *J. Biomech.* **37,** 989–1000 (2004).

109. Lanir, Y. Constitutive equations for fibrous connective tissues. *J. Biomech.* **16,** 1–12 (1983).

110. Stella, J. a, D'Amore, A., Wagner, W. R. & Sacks, M. S. On the biomechanical function of scaffolds for engineering load-bearing soft tissues. *Acta Biomater.* **6,** 2365–81 (2010).

111. D'Amore, A., Stella, J. A., Wagner, W. R., Sacks, M. S. & Amore, A. D. Characterization of the complete fiber network topology of planar fibrous tissues and scaffolds. *Biomaterials* **31,** 5345–54 (2010).

112. Taylor, C. a & Humphrey, J. D. Open Problems in Computational Vascular Biomechanics: Hemodynamics and Arterial Wall Mechanics. *Comput. Methods Appl. Mech. Eng.* **198,** 3514–3523 (2009).

113. Dahl, S. L. M. *et al.* A microstructurally motivated model of the mechanical behavior of tissue engineered blood vessels. *Ann. Biomed. Eng.* **36,** 1782–92 (2008).

114. Matsuda, N., Shimizu, T., Yamato, M. & Okano, T. Tissue Engineering Based on Cell Sheet Technology. *Adv. Mater.* **19,** 3089–3099 (2007).

115. Takei, Y. G. *et al.* Dynamic Contact Angle Measurement of Temperature-Responsive Surface Properties for Poly(N-isopropylacrylamide) Grafted Surfaces. *Macromolecules* **27,** 6163–6166 (1994).

116. Isenberg, B. C. *et al.* A thermoresponsive, microtextured substrate for cell sheet engineering with defined structural organization. *Biomaterials* **29,** 2565–72 (2008).

117. Suki, B. Assessing the functional mechanical properties of bioengineered organs with emphasis on the lung. *J. Cell. Physiol.* **229,** 1134–40 (2014).

118. Kittel, C. *Introduction to Solid State Physics*. (John Wiley & Sons, 1968).

119. Purcell, E. M. *Electricity and Magnetism*. (McGraw-Hill, 1965).

120. Budynas, R. *Advanced Strength and Applied Stress Analysis*. (McGraw-Hill, 1998).

121. Kinahan, M. E. *et al.* Tunable silk: Using microfluidics to fabricate silk fibers with controllable properties. *Biomacromolecules* **12,** 1504–1511 (2011).

122. Isenberg, B. C., Williams, C. & Tranquillo, R. T. Small-diameter artificial arteries engineered in vitro. *Circ. Res.* **98,** 25–35 (2006).

123. Sarkar, S., Sales, K. M., Hamilton, G. & Seifalian, A. M. Addressing Thrombogenicity in Vascular Graft Construction. *J. Biomed. Mater. Res. B. Appl. Biomater.* **82,** 100–108 (2007).

124. Tekin, H., Ozaydin-Ince, G. & Tsinman, T. Responsive microgrooves for the formation of harvestable tissue constructs. *Langmuir* **59,** 863–883 (2011).

125. Sarkar, S., Lee, G. Y., Wong, J. Y. & Desai, T. a. Development and characterization of a porous micro-patterned scaffold for vascular tissue engineering applications. *Biomaterials* **27,** 4775–82 (2006).

126. Ayres, C. E. *et al.* Measuring fiber alignment in electrospun scaffolds: a user's guide to the 2D fast Fourier transform approach. *J. Biomater. Sci. Polym. Ed.* **19,** 603–21 (2008).

127. Choi, B.-C., Choi, S. & Leckband, D. E. Poly(N-isopropyl acrylamide) brush topography: dependence on grafting conditions and temperature. *Langmuir* **29,** 5841–50 (2013).

128. Schneider, M. H., Tran, Y. & Tabeling, P. Benzophenone absorption and diffusion in poly(dimethylsiloxane) and its role in graft photo-polymerization for surface modification. *Langmuir* **27,** 1232–40 (2011).

129. Lin, J. B. *et al.* Thermo-responsive poly(N-isopropylacrylamide) grafted onto microtextured poly(dimethylsiloxane) for aligned cell sheet engineering. *Colloids Surf. B. Biointerfaces* **99,** 108–15 (2012).

130. Kuddannaya, S. *et al.* Surface Chemical Modification of Poly (dimethylsiloxane) for the Enhanced Adhesion and Proliferation of Mesenchymal Stem Cells. *ACS Appl. Mater. Interfaces* **5,** 9777–9784 (2013).

131. Patel, N. G., Cavicchia, J. P., Zhang, G. & Zhang Newby, B. Rapid cell sheet detachment using spin-coated pNIPAAm films retained on surfaces by an aminopropyltriethoxysilane network. *Acta Biomater.* **8,** 2559–67 (2012).

132. Gauvin, R. *et al.* Dynamic mechanical stimulations induce anisotropy and improve the tensile properties of engineered tissues produced without exogenous scaffolding. *Acta Biomater.* **7,** 3294–301 (2011).

133. Holzapfel, G. A. *Nonlinear Solid Mechanics*. (John Wiley & Sons, 2000).

134. Weidenhamer, N. K. & Tranquillo, R. T. Influence of cyclic mechanical stretch and tissue constraints on cellular and collagen alignment in fibroblast-derived cell sheets. *Tissue Eng. Part C. Methods* **19,** 386–95 (2013).

135. Takahashi, H., Nakayama, M., Shimizu, T., Yamato, M. & Okano, T. Anisotropic cell sheets for constructing three-dimensional tissue with well-organized cell orientation. *Biomaterials* **32,** 8830–8 (2011).

136. Williams, C. *et al.* The use of micropatterning to control smooth muscle myosin heavy chain expression and limit the response to transforming growth factor β1 in vascular smooth muscle cells. *Biomaterials* **32,** 410–418 (2011).

137. Shen, J. Y. *et al.* Three-dimensional microchannels in biodegradable polymeric films for control orientation and phenotype of vascular smooth muscle cells. *Tissue Eng.* **12,** 2229–2240 (2006).

138. Xing, Q. *et al.* Decellularization of Fibroblast Cell Sheets for Natural Extracellular Matrix Scaffold Preparation. *Tissue Eng. Part C* **21,** 77–87 (2015).

139. Gorschewsky, O., Klakow, A., Riechert, K., Pitzl, M. & Becker, R. Clinical comparison of the Tutoplast allograft and autologous patellar tendon (bone-patellar tendon-bone) for the reconstruction of the anterior cruciate ligament: 2- and 6-year results. *Am. J. Sports Med.* **33,** 1202–1209 (2005).

140. Suki, B. *et al.* Biomechanics of the lung parenchyma: critical roles of collagen and mechanical forces. *J. Appl. Physiol.* **98,** 1892–9 (2005).

141. Dobrin, P. Mechanical properties of arteries. *Physiol. Rev.* **58,** 397–460 (1978).

142. Ritter, M. C. *et al.* A zipper network model of the failure mechanics of extracellular matrices. *Proc. Natl. Acad. Sci. U. S. A.* **106,** 1081–6 (2009).

143. Kothapalli, C. R., Taylor, P. M., Smolenski, R. T., Yacoub, M. H. & Ramamurthi, A. Transforming growth factor beta 1 and hyaluronan oligomers synergistically enhance elastin matrix regeneration by vascular smooth muscle cells. *Tissue Eng. Part A* **15,** 501–511 (2009).

144. Kim, W. & Chaikof, E. L. Recombinant elastin-mimetic biomaterials: Emerging applications in medicine. *Adv. Drug Deliv. Rev.* **62,** 1468–1478 (2010).

145. Gasser, T. C., Ogden, R. W. & Holzapfel, G. a. Hyperelastic modelling of arterial layers with distributed collagen fibre orientations. *J. R. Soc. Interface* **3,** 15–35 (2006).

Curriculum Vitae

Daniel Edwin Backman

Boston University College of Engineering

Department of Biomedical Engineering

44 Cummington Mall, Room 520 Boston, MA 02215

Year of Birth: 1983

Education

PhD in Biomedical Engineering **2008–2015**
Boston University, Boston, MA
Dissertation: "*Biomechanics of Aligned Cell Sheets for Arterial Tissue Engineering*"

Bachelors of Science in Mechanical Engineering **2001–2005**
Tufts University, Medford, MA
Double Major in Mechanical Engineering and Mathematics

Research Experience

Research Assistant, Biomimetic Materials Engineering Lab **2009–2015**
PhD candidate under Professor Joyce Wong, Department of Biomedical Engineering, Boston University, Boston, MA

Staff Scientist **2007–2008**
Ocean Acoustical Services and Instrumentation Systems, Lexington, MA

Intern **2005**
Los Alamos Dynamics Summer School, Los Alamos National Laboratory, NM.

Undergraduate Research Assistant **2004–2005**
Worked for Prof. Douglas Matson, Department of Mechanical Engineering, Tufts University, Medford, MA

Research Intern **2003**
Working for Luca M. Bigatello, M.D., Department of Anesthesiology Massachusetts General Hospital, Boston, MA

Publications

Isenberg, B.C., **Backman, D.E**., Kinahan M.E., Jesudason R., Suki, B., Stone, P.J., Davis, E.C. and Wong, J.Y., Micropatterned cell sheets with defined cell and extracellular matrix orientation exhibit anisotropic mechanical properties. *Journal of Biomechanics*

Flynn, E.B., Swartz, R.A., **Backman, D.E.,** Park, G., Farrar, C. R. (2009), "Active-Sensing Lamb Wave Propagations for Damage Identification in Honeycomb Aluminum Panels," Journal of the Korean Society for Nondestructive Testing, Vol. 29, No.4, pp. 269–282.

Roberts, E. G., Lee, E. L., **Backman, D.E**, Buczek-Thomas, J. A., Emani, S., & Wong, J. Y. (2014). Engineering Myocardial Tissue Patches with Hierarchical Structure–Function. *Annals of Biomedical Engineering*

Conference Participation

Presentations

Flynn, E.B. Swartz, R.A., **Backman, D.E**., "Active Piezoelectric Sensing for Damage Identification in Honeycomb Composite Panels", 24th annual International Modal Analysis Conference (2006)

Proceedings

Backman, D.E., Flynn, E.B., Swartz, R.A., Hundhausen, R.J., Park, G., "Active Piezoelectric Sensing for Damage Identification in Honeycomb Composite Panels," *Proceedings of 24th International Modal Analysis Conference*, Jan 30–Feb 2 2006, St. Louis, MO

V. Premus, **D. Backman,** "A Matched Subspace Approach to Depth Discrimination in a Shallow Water Waveguide", *Proc. of the 41st Asilomar Conference on Signals, Systems, and Computers*, Nov 2007.

Posters

Backman, D.E., Isenberg, B.C., Wong, J.Y. *"Mechanical Properties of Aligned Cell Sheets for Arterial Tissue Engineering", Gordon Research Conference - Tissue Engineering and Biomaterials, August 2011, Holderness, NH*

Backman, D.E., J.Y. Wong, "Biomechanics of Cell Sheets Based Arterial Tissue using a Novel Force Sensor", *Society For Biomaterials 2013 Annual Meeting and Exposition: Biomaterials Revolution*, April 2013, Boston, MA.